RWTH AACHEN UNIVERSITY

# Track Selection for the Alignment of the CMS Tracker

von
Matthias H. Edelhoff

Diplomarbeit in Physik
vorgelegt der

Fakultät für Mathematik, Informatik und Naturwissenschaften
der RWTH Aachen University

im November 2008

angefertigt im
I. Physikalischen Institut B

Professor Dr. Lutz Feld

# Contents

# 1. Introduction

Near Geneva at the french-swiss border the Large Hadron Collider (LHC) has been built. This proton-proton collider is designed to reach a centre-of-mass energy up to 14 TeV and is one of the biggest scientific endeavours in the history of high energy physics. For proton-proton collisions, the centre-of-mass energy is one order of magnitude higher than the centre-of-mass energy reached by any comparable high energy physics experiment before. Fig. 1.1 shows the rise in cross-sections compared to the Tevatron, which was the most powerful collider before the LHC. In combination with the high luminosity this will allow to search for new physics like the nature of electroweak symmetry breaking and physics beyond the Standard Model. On the other hand properties of already known particles like the top quark will be examined in greater detail. For instance the rate of top-antitop events is expected to be more than 1 Hz even at a low luminosity of $10^{33}$ cm$^{-2}$s$^{-1}$ which is planned for the first year of data-taking [1] at the Compact Muon Solenoid (CMS), one of the LHC experiments. This high rate will make it possible to study properties of the Standard Model such as the top mass in great detail.

In order to reach these and further goals precise detectors are needed. This thesis concentrates on one of the most versatile detectors: The Compact Muon Solenoid (CMS) experiment. It is set up to provide measurements on the full variety of LHC physics from higgs search, over top- and b-physics to the analysis of heavy ion collisions. To meet the requirements of these different fields a powerful and reliable inner tracking system has been built. It measures the trajectories of charged particles emerging from the interaction region. However, to reach its full potential in particle momentum measurement, vertex position reconstruction, and b-tagging, the position and orientation of more than 16 000 measuring components of the tracking system hahave to be determined and monitored. This procedure is called tracker alignment. The gained precision of these alignment measurements is significantly better than the mechanical mounting precision of the detector components. One possibility to measure these positions and orientations uses tracks reconstructed in the tracking system itself (track based alignment, see section 2.2). Since it uses the tracker's own measurements, track based alignment can be applied after the tracker is installed in the experiment.

This thesis deals with the selection of tracks for track based alignment. Methods and criteria leading to robust high statistics track selections are described. Likewise, the selections of smaller, pure track samples of the physics processes $Z \to \mu^+\mu^-$, $J/\psi \to \mu^+\mu^-$ and $\Upsilon \to \mu^+\mu^-$ are covered. Using these selections, the known invariant mass of the mother particles and the common vertex of the two tracks introduce additional information to solve the alignment

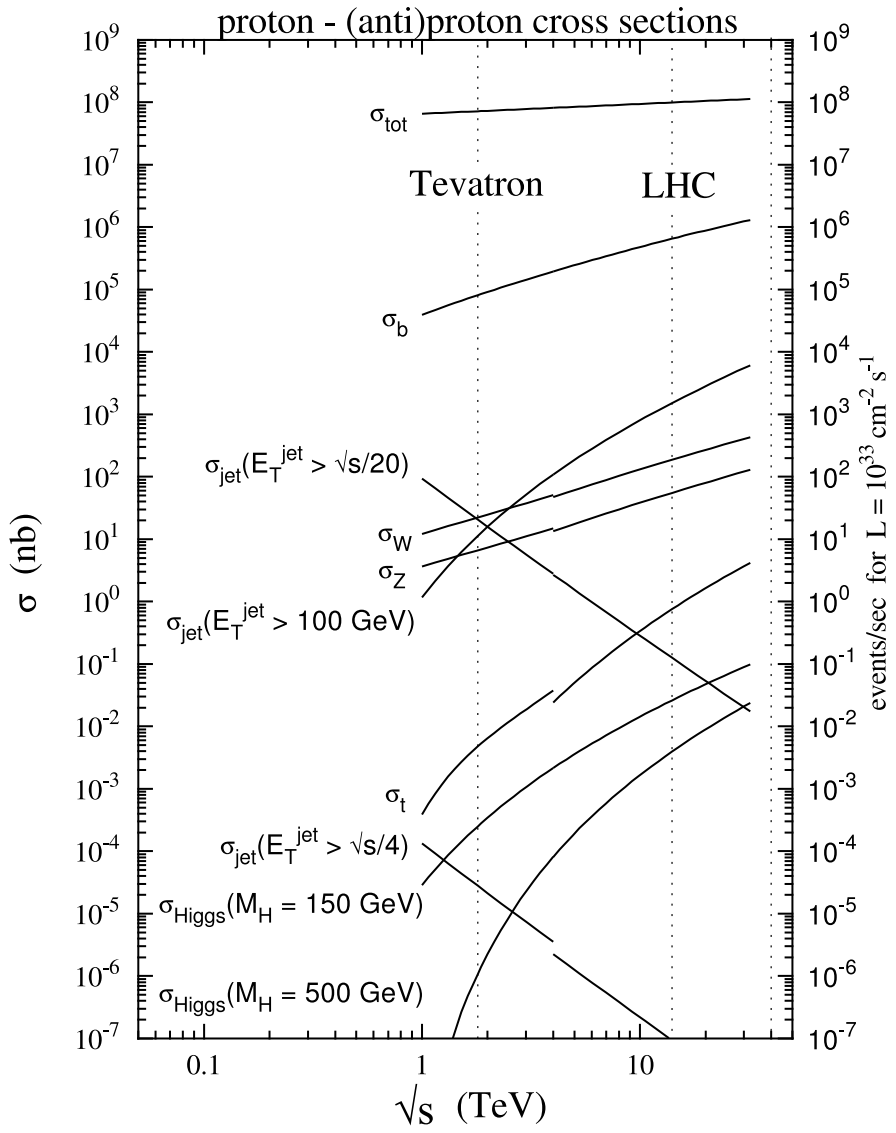


**Figure 1.1:** Expected cross-sections of various physics channels at the LHC in comparison to the Tevatron

problem. In addition to these selections, further track sources which do not stem from collisions in the center of CMS are available.
All selections are bench-marked using full tracker module-level alignment on the basis of simulations of the first $\mathcal{L} = 10$ pb$^{-1}$ to be collected by CMS. In the course of these studies the necessary software was developed, tested and put into place in the overall CMS computing scheme. Chapter 3 documents the resulting selection mechanisms as well as measures to monitor track selection performance.
Chapter 4 introduces the selection of tracks from resonance decays. Especially the $Z \to \mu^+\mu^-$ decay has been studied in the past and shown to provide excellent tracks for alignment [2]. Therefore the selection of these tracks from a realistic mixture of events was studied and tuned to select pure track samples. Tracks from the decays $J/\psi \to \mu^+\mu^-$ and $\Upsilon \to \mu^+\mu^-$ are selected, which are expected to be similarly beneficial for alignment. For all three selections, the knowledge of the invariant mass and the common vertex is exploited to gain additional information.
During the early stages of the CMS experiment none of the above selections will gain enough statistical power to determine the positions and rotations of the large number of measuring components. Therefore as discussed in chapter 5, selections were developed that do not choose events based on their physics content, but on general track quality. These samples are available with high statistics, where – due to smaller cross-sections – resonance samples are too small to constrain all $6 \times 16000$ degrees of freedom.
In chapter 6, the combination of those high statistics samples and samples that are too small for a stand alone alignment is shown. First, the effect of adding tracks from the $Z \to \mu^+\mu^-$ and $\Upsilon \to \mu^+\mu^-$ was studied. Secondly, the use of tracks that do not originate from the interaction point is investigated. As part of this study, the first successful alignment using beam halo tracks is shown. Those tracks originate from known interaction with residual gas or material close to the beam line, e.g. collimators. Additionally, the gain in alignment precision using muons produced in air showers is discussed.

## 1.1 The Large Hadron Collider

In the old tunnel of the Large Electron Proton Collider (LEP) [3] about 100 metres below the surface, the Large Hadron Collider (LHC) [4] has been built at the European Organisation for Nuclear Research (CERN) near Geneva, Switzerland. It is a proton-proton collider which has been designed to reach centre of mass energies up to 14 TeV and a luminosity of $10^{34}$ cm$^{-2}$s$^{-1}$ at the multi-purpose detectors ATLAS [5] and CMS [6]. To reach these properties - and thus a high discovery potential - LHC is designed for a high bunch crossing rate of 40 MHz. At each of these crossings an average of about 20 proton-proton interactions will be superimposed in the detectors. Thus, they have to be build with high granularity and low latency. The collider itself is a 27 km circumference synchrotron containing two anti-parallel proton beams (Fig. 1.2). Those beams will be kept on track by 8 T super conducting Nb-Ti dipole magnets cooled to a temperature below 2 K by super fluid Helium. In addition quadrupole, sextupole, oktupole, and higher order magnets are in place to focus and control the beams. Apart from the proton-proton collision programme the same machine is built to collide Pb ions, which will allow dedicated heavy ion studies at luminosities up to $10^{27}$ cm$^{-2}$s$^{-1}$ [4].
During the start up phase in the year 2009 it is proposed to initially take data at a lower center of mass energy of 10 TeV and reduced luminosity between $2 \cdot 10^{30}$ cm$^{-2}$s$^{-1}$ and $2 \cdot 10^{31}$ cm$^{-2}$s$^{-1}$ at the multi-purpose detectors.

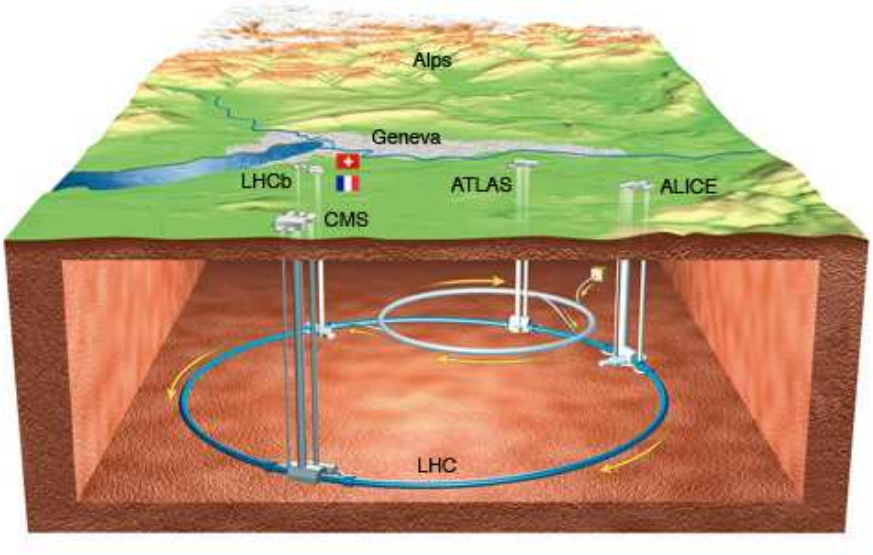


**Figure 1.2:** The Large Hadron Collider site and experiments.

### 1.1.1 Detectors at the LHC

The proton beams of the LHC will collide at four positions along its circumference. At each site one experiment will take data and study different aspects of high energy physics. Of those experiments ATLAS and CMS are multi-purpose detectors built to probe an as wide range of topics as possible. To this end they aim to hermetically cover the $4\pi$ solid angle around the interaction region with precise tracking and calorimetry detectors. Powerful muon systems for muon momentum measurement, triggering, and particle identification complete the design. Although the ATLAS and CMS scientific programmes largely overlap, different design choices in both tracking and calorimetry systems lead to two distinct experiments.
The other two detectors are specialised for specific topics of high energy physics: LHCb [7] will study physics concerning the b-quark and its mesons which are expected to be produced in abundance at LHC. Therefore LHCb does not need to cover the whole angular space around the interaction point, but concentrates its sophisticated spectrometer arm in one forward region. Finally Alice [8] is designed to investigate heavy ion collisions and specialises to be able to accommodate the large amount of particles that will be produced in those collisions.

## 1.2 The Compact Muon Solenoid

The Compact Muon Solenoid (CMS) [6] resides about 100 m underground near the village of Cessy at the french-swiss border. It is 21.6 m long and has a diameter of 14.6 m. In order to measure the momentum of highly energetic charged particles a homogeneous magnetic field in a cylindrical volume with a length of 12.5 m and a diameter of 6 m is at the center of the detector. It is generated by a 3.8 T super-conducting solenoid. In this volume there is enough room for the full silicon tracking system, the electromagnetic calorimeter, and most of the hadronic calorimeter. An additional tracking system is placed in the iron return yoke outside of the solenoid to identify and measure muon tracks (muon system).
In this thesis positions and directions are given in a cylindrical coordinate system. The origin of this system is the center of the detector and the $z$-axis points - along the beam line - towards the Jura mountains. The azimuthal coordinate $\varphi$ is measured from a radial vector

pointing towards the center of the LHC. Polar directions are given in as pseudo-rapidity $\eta = -\ln\tan(\theta/2)$, where the polar angle $\theta$ is measured from the $z$-axis.
Since the direction of the solenoid field is parallel to the beam line, the precision of the momentum measurement is dominated by the precision of measurements in this bending plane. Thus, the precision of the $r\varphi$ coordinate needs to be maximised for all tracking systems.

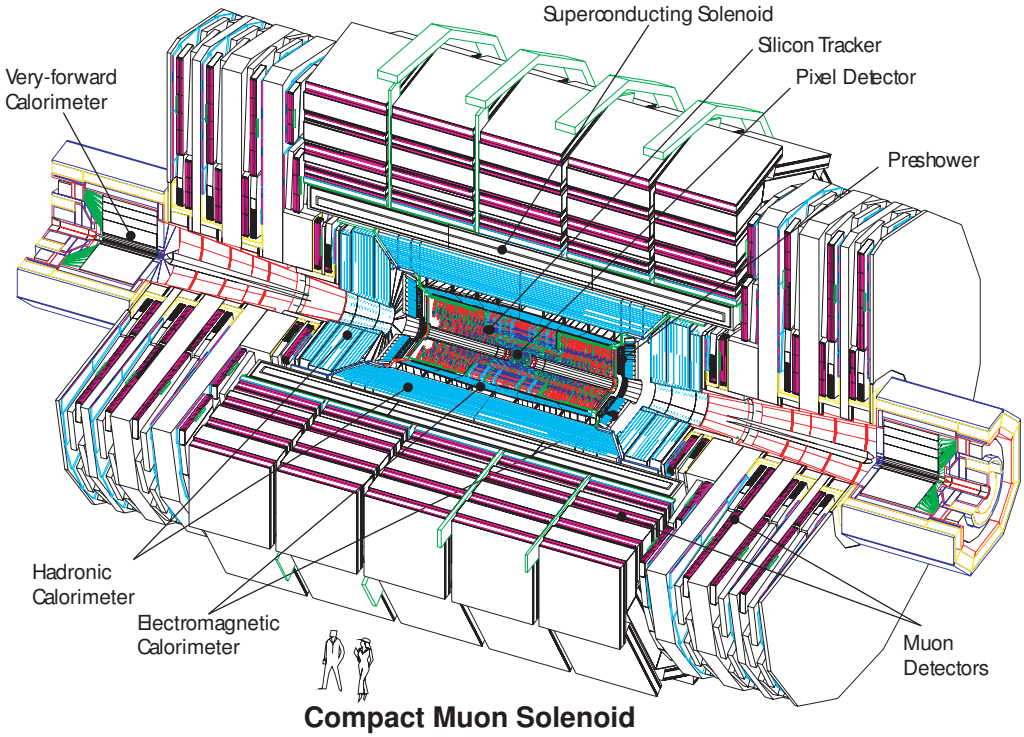


**Figure 1.3:** The CMS Detector.

### 1.2.1 The Muon System

Electrons, Photons and Hadrons are absorbed in the calorimeters (section 1.2.2). Only muons can penetrate to the muon system of CMS. It consists of three different types of detectors: The drift tube (DT) chambers, the cathode strip chambers (CSC) and the resistive plate chambers (RPC). The three systems share a modular design where the big superstructures (stations) are build out of smaller independent building blocks.
The fast response time below 25 ns of the RPCs is achieved by double gap chambers operated in avalanche mode, which are placed in the region $|\eta| < 1.6$. In the barrel region six RPC stations are attached to the DT stations. In the end caps they are mounted in three stations near the CSCs. This ensures independent and reliable muon triggering even at the high interaction rate, pileup and backgrounds at nominal LHC operation.
In the barrel region covering $|\eta| < 1.2$ the DT chambers are segmented into four stations arranged in cylinders with increasing radius around the beam line (see Fig. 1.3). Three stations contain eight chambers measuring the $r\varphi$ direction and four chambers measuring in $z$ direction along the beam line. The outermost fourth station - at the outer radius of CMS - measures in $r\varphi$ direction only. They are built out of rectangular drift cells containing one anode wire and are filled by a mixture of $Ar$ and $CO_2$.
Due to higher expected occupancy, higher background rates, and the inhomogeneity of the magnetic field in the end cap region of the muon system another detector design has been chosen. In the region $0.9 < |\eta| < 2.4$ the CSCs detect muons in four concentric rings orthogonal

to the beam line. These rings are segmented into trapezoidal multi-wire proportional chambers filled by a gaseous mixture of $Ar$, $CO_2$, and $CF_4$.
When combined, the DTs and CSCs yield an offline stand-alone $p_T$ measurement resolution up to 9%. Fig. 1.4 shows that the combination of this measurement with that of the inner tracking system notably improves the transverse momentum measurement. Particle tracks reconstructed in this way are referred to as "global muon" and play a significant role throughout this thesis.

**(a)** central region **(b)** forward/backward region

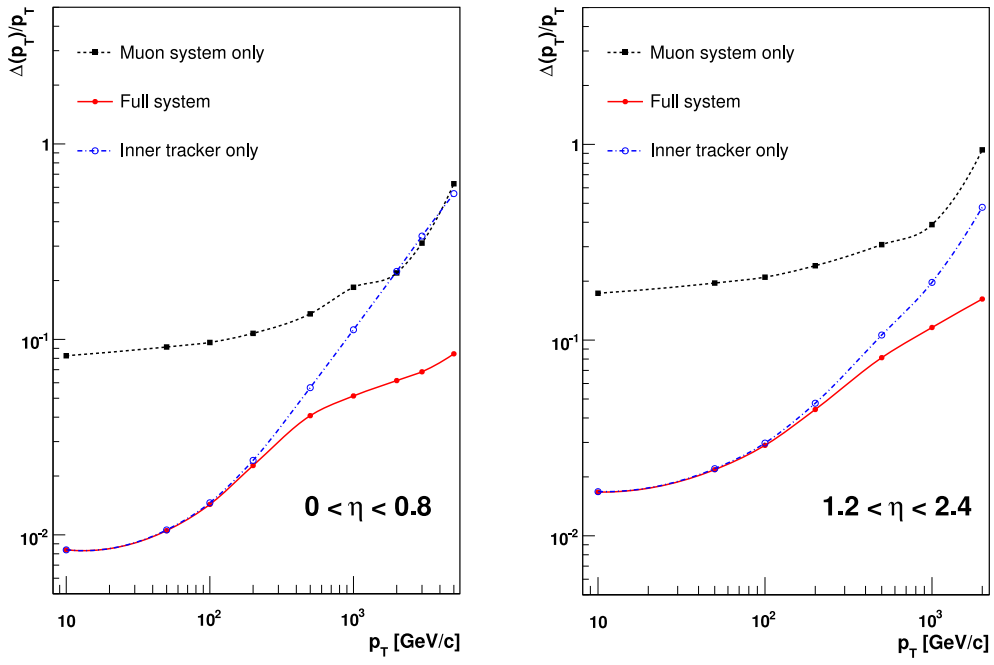


**Figure 1.4:** Transverse momentum measurement resolution for muon system, inner tracking system, and the combination of both [6].

For all systems the chambers are interleaved, so that blind spots in $\eta$ or $\varphi$ coverage are omitted. In this way the offline reconstruction efficiency for single muons typically is 95% to 99% dropping to the lower value only in the regions around $|\eta| \approx 0.25$, 0.8, and 1.2 due to the transition between DT wheels and between the DT and the CSC system.

### 1.2.2 The Calorimeters

For many physics channels the measurement of missing transverse energy or the reconstruction of neutral particles is essential. This is achieved in the calorimeters. Measuring missing energy requires hermetical calorimetry, whereas measuring the direction of neutral particles needs high segmentation of the same. Both is accomplished in the CMS calorimeters described in the following sections.

#### The Hadronic Calorimeter

The hadronic calorimetry is divided into four systems: barrel hadronic calorimeter (HB) inside the magnetic coil at $|\eta| < 1.3$ complemented by the tail catcher (HO) outside of the coil, the

end cap (HE) at $1.3 < |\eta| < 3$, and the forward calorimeter (HF) extending this range up to $|\eta| = 5.2$. Due to different radiation and magnetic field properties in this big region different combinations of absorbing and active materials are used for these sampling calorimeters. The HB uses brass and steel plates as absorber where the steel plates are used as supporting structures as well. This amounts to a hadronic interaction length of between 5.82 $\lambda_I$ and 10.6 $\lambda_I$ depending on the angle. On the inner radius the electromagnetic calorimeter adds 1.1 $\lambda_I$. On the outer radius the magnet coil and the first layer of the iron return yoke is used as an absorber in front og HO, resulting in a minimal interaction length of 11.8 $\lambda_I$ in the barrel region. The HE uses brass to avoid distortion of the magnetic field, reduce cost, and stabilise the detector. In this way it reaches a total interaction length of about 10 $\lambda_I$. All hadronic calorimeters use plastic scintillators in combination with wavelength shifting fibres. The HB, HE, and HO are using photodiodes for read out, while only the HF uses Cherenkov radiation emitted in quartz fibres. Those are inserted into steel absorber plates leading to an interaction length of 10 $\lambda_I$. This choice was dictated by the extreme radiation near the beam line ( 12.5 cm $< r <$ 130 cm ).

**The Electromagnetic Calorimeter**

The electromagnetic calorimeter is built out of 75 848 lead tungstate ($PbWO_4$) crystals. Like nearly every other detection system in CMS it is divided into a barrel region $|\eta| < 1.479$ and two end caps $1.479 < |\eta| < 3.0$. Together both systems build a hermetic and homogeneous calorimeter which, due to its high granularity and fast response time, is well suited for the LHC environment.
The shape of the crystals in the barrel region is a truncated pyramid with a 22 mm $\times$ 22 mm front face and a 26 mm $\times$ 26 mm back face. Grouped into sub- and supermodules they form a cylinder defined by an inner radius of 1.29 m. Their length of 23 cm yields a radiation length of 25.8 $X_0$ providing negligible leakage from its back side up to energies of 500 GeV. The blue-green light emitted by the lead tungstate is received by avalanche photo diodes at the back end of the crystals which allow a good measurement of the 4.5 photoelectrons per MeV in the presence of the high longitudinal magnetic field.
Behind a preshower detector the crystals in the end cap region have a front face of 28.62 mm $\times$ 28.62 mm, a back face of 30 mm $\times$ 30 mm, and a length of 22 cm (24.7 $X_0$) providing properties similar to the barrel region. Due to the different layout of the magnetic field and higher level of radiation the end cap crystals are read out by vacuum phototriodes.
The energy resolution of the calorimeter given by

$$\left(\frac{\sigma}{E}\right)^2 = \left(\frac{S}{\sqrt{E}}\right)^2 + \left(\frac{N}{E}\right)^2 + C^2$$

is determined by the stochastic term S, the noise term N and a constant C. During a beam test in 2004 values of $S = 2.8\%\ \sqrt{\text{GeV}}$, $N = 12\%$ GeV, and $C = 0.30\%$ have been established.

**The Very Forward Calorimetry**

Complementing the described calorimetry two additional detectors have been installed in the CMS cavern and hte LHC tunnel. First, the CASTOR detector placed 14.38 m from the interaction point covering $5.3 < \eta < 6.6$ and then, the Zero Degree Calorimeter (ZDC) with a distance of about 140 m from the interaction region covering $|\eta| > 8.3$. Due to the high radiation levels both are quartz tungsten sampling calorimeters. Varying the absorber and active material geometry both calorimeters optimise energy resolution for electromagnetic and hadronic showers.

### 1.2.3 The Tracker

The inner tracking system of CMS consists of about 200 $m^2$ of active silicon surface segmented into more than 16 thousand modules, featuring 512 to 4160 channels. This high granularity is necessary since at design luminosity each LHC bunch crossing will result in about one thousand particles emerging from the interaction point. Due to the large inner radius of the CMS solenoid, all of the instrumented volume - a cylinder of 5.8 m in length and 2.5 m in diameter - features a homogeneous magnetic field. Fig. 1.5 shows a schematic view of the structure of the tracker described in the following sections. It measures particle tracks up to $|\eta| = 2.5$ and in the full $\varphi$ range. The tracker is divided into pixel detector and strip tracker. The first is subdivided into forward pixel detector and barrel pixel detector. The second is subdivided into tracker inner and outer barrel as well as tracker inner disks and tracker end cap.

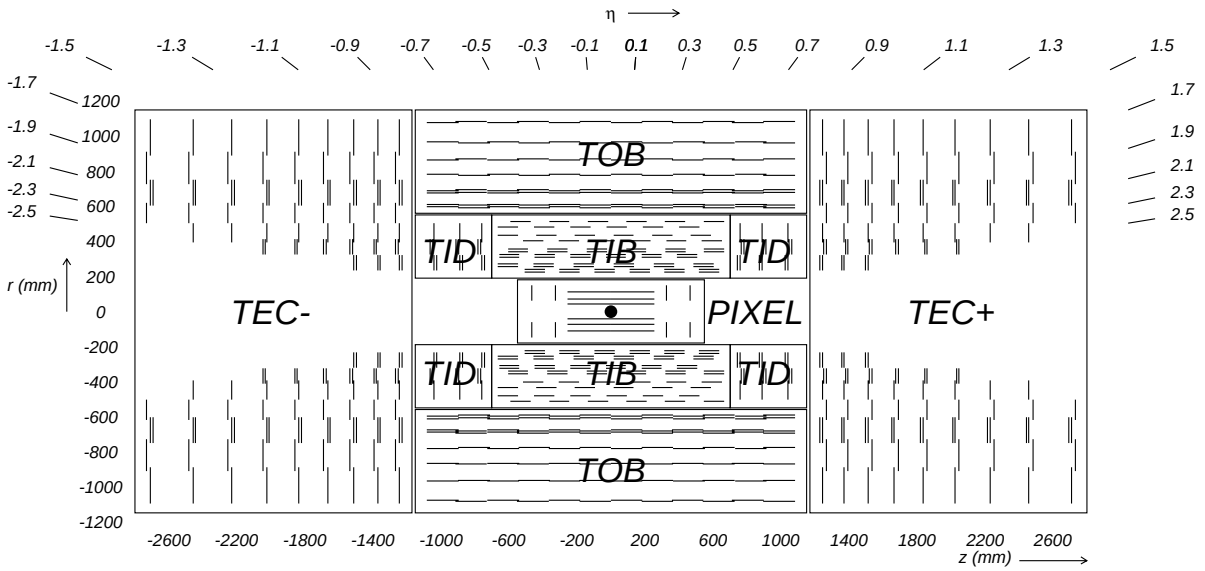


**Figure 1.5:** Sketch of the CMS inner tracking system.

#### The Pixel Detector

In order to precisely measure secondary vertices, modules in the innermost part of the tracking system are structured in $100 \times 150$ $\mu m^2$ pixels leading to two dimensional high resolution hit measurements (see Table 1.1). This subsystem is divided into a barrel region (PXB) and two endcaps (PXF). Spanning a length of 53 cm the PXB consists of three layers at $r = 4.4$ cm, 7.3 cm, and 10.2 cm. The cylindrical geometry around the beam line yields most sensitive measurements along $r\varphi$ and $z$. As shown in Fig. 1.5 two groups of two disks forming the forward pixel detectors are placed on each side of this volume at $z = \pm 34.5$cm and $z = \pm 46.5$cm, producing precise measurements along $r\varphi$ and $r$. In total, the 1440 sensitive modules contain 66 million two-dimensional measurement points. In order to withstand the extreme radiation close to the interaction point the pixel detectors are built implanting high dose n-implants into a n-type substrate. Nevertheless the expected lifetime for the innermost pixel layers of two years at full design luminosity is short compared to the ten year lifetime for the less irradiated strip tracker.

#### The Strip Tracker

Beyond the pixel detector the tracking volume is covered by a silicon strip tracker. The strip pitch of its 15148 modules ranges between 80 μm in the inner regions and 205 μm in its outer

**Table 1.1:** Resolution of the tracker subsystems. Resolutions in the pixel detectors is enhaced by the template hit reconstruction method described in [9]. The layout of the silicon strip sensors is given in [6] and [10]. Resolutions for the strip tracker are calculated as $\frac{1}{\sqrt{12}}\times$ pitch, assuming a uniform distribution of hits in the measuring direction.

| Name | Shorthand | Direction | Resolution |
|---|---|---|---|
| Barrel Pixel | PXB | $r\varphi \times z$ | $9 \times 21$ µm$^2$ |
| Forward Pixel | PXF± | $r\varphi \times r$ | $15 \times 25$ µm$^2$ |
| Tracker Inner Barrel | TIB | $r\varphi$ | $23 - 35$ µm |
| Tracker Outer Barrel | TOB | $r\varphi$ | $35 - 53$ µm |
| Tracker Inner Disks | TID± | $\varphi$ | $91 - 100$ µrad |
| Tracker Endcaps | TEC± | $\varphi$ | $45 - 100$ µrad |

regions leading to measurement resolutions shown in Table 1.1. The barrel part of the strip tracker is subdivided into the tracker inner barrel (TIB) and the tracker outer barrel (TOB) covering the range of 20 cm $< r <$ 116 cm extending up to $z = \pm 118$ cm. In this volume two groups of three tracker inner disks (TID±) are inserted covering a radial range up to 55 cm. Finally the two groups of nine disks of the tracker end caps (TEC±) provide measurements in the region 124 cm $< |z| <$ 282 cm and up to a radius of 113.5 cm.
While the strips in the barrel region (TIB and TOB) are placed parallel to the beam line, the strips in the end caps (TID and TEC) are radial and orthogonal to the beam line. Therefore, the modules in the barrel region are rectangular whereas end cap modules are trapezoidal. This layout ensures that $r\varphi$ is the most sensitive measurement throughout the strip tracker, leading to precise transverse momentum measurements. Additional modules have been added back to back to the first two layers and rings of all strip tracker subsystems and the fifth ring of TEC± (stereo modules). Tilted by 100 mrad, stereo modules provide an additional measurement near that of the untilted module. The combined information obtained from both modules allows to measure the $r$ coordinate in the end caps and the $z$ coordinate in the barrel region. This is used for pattern recognition during reconstruction and to constrain module positions for the alignment of the detector. For the track fit the measurement of the second back-to-back module is used as separate one dimensional measurement instead of a combined two dimensional one.

### 1.2.4 The Structure of Computational Services for CMS

The high bunch crossing rate of 40 MHz and the described formidable granularity of the CMS detector leads to high data rates of about 60 TB s$^{-1}$. To cope with this, the collaboration had to build both a powerful computing structure and an efficient triggering system. The latter reduces the data rate by selecting events of possible interest to physics analyses for reconstruction and storage. Fig. 1.1 shows the difference between the total cross-section and the cross-section of interesting physics channels which makes this reduction necessary.

#### The Trigger System

The first step in event selection is called Level One (L1) trigger. It comprises mostly programmable dedicated integrated circuits built directly into the detector read out systems. Due to time constraints the L1 decision is reached analysing coarsely segmented information

from the calorimetry and muon systems, reducing the data rate to 30 kHz. Two thirds of the technically possible rate of 100 kHz are kept as a backup. The full measurement of the event is kept in front-end buffers and read out in case of a positive decision. The tracker can not be used to select events on this level.
The High Level Trigger (HLT) can make use of the full information acquired during the event in order to reduce this rate to about 100 Hz to 300 Hz. Contrary to the L1 trigger the data is processed by software components very similar to the ones used in offline analysis. This implies the use of a flexible computing farm built out of commercial hardware. The result of this first analysis of the recorded data is stored with the event in the form of HLT-bits. Each of which indicate if the event in question did pass the requirements corresponding to that bit. By logical combination the HLT-bits allow fast pre-selection for any subsequent analysis. The complete sets of those definitions can be found in [11] and [12].

**The Reconstruction Procedure**

Even after the event rate reduction described in the previous section about 1.6 TB $h^{-1}$ have to be reconstructed, stored and eventually analysed. All three tasks are not going to be tackled in a single monolithic computing center, but in several centers distributed around the world. In this model - known as the "GRID" - centers are subdivided into a hierarchical structure of "tiers". The first tier (Tier0), is located at CERN receiving data directly from the experimental site. After a first reconstruction data that can be used to obtain alignment and calibration constants is selected and reduced to a light weight data format (ALCARECO) (Fig. 1.6). Due to strict computational limits, this "express stream" can accomodate only about 20% of the data transferred to the Tier0. The neccesarry selection is based on high level trigger bits. Thereafter, the resulting datasets are transferred to the CERN Analysis Facility (CAF). Here experts have direct and fast access to these data enabling them to produce alignment and calibration constants in a timely manner. The derived constants are then used to reconstruct all the events read out from the detector. The next tiers (Tier1) are hosted by several states collaborating in the experiment. They receive the raw data and the outcome of the first reconstruction to build a redundant storage and to distribute the information to lower tiers which are located directly at member institutes around the globe. When sufficient data is recorded, in-depth studies of the alignment and calibration are performed and more accurate corrections are calculated (long term constants). Those corrections are used to re-reconstruct the data stored at the Tier1 centers in order to increase the precision as far as possible.

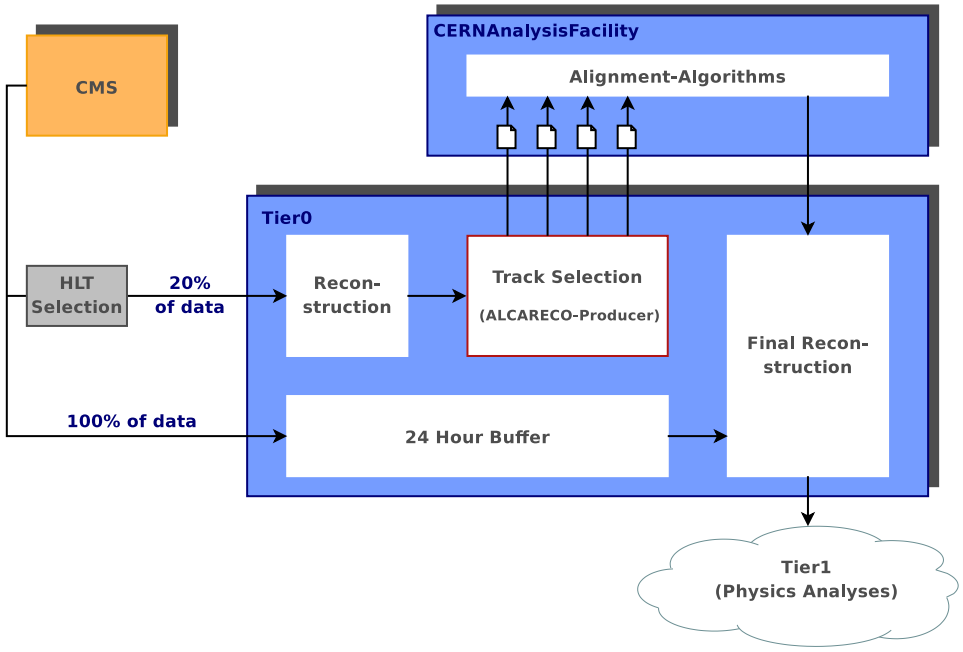


**Figure 1.6:** Path of the data from the experiment to the Tier1 centers

# 2. The Alignment Problem

The CMS inner tracking system as described in section 1.2.3 is built out of 1440 pixel and 15148 strip modules. Although great care has been taken to mount the modules precisely at the right position and tilt, the measurement precision of the modules (Tab 1.1) is better than the possible mounting precision. Therefore, the position and tilt of each silicon module has to be determined as precisely as possible in order to correct for slight deviations from the designed layout of the detector. Since no survey is possible once all modules are in place, the position has to be obtained via the module's own measurements. This procedure is called alignment. It improves both the pattern recognition and the track fit, which determines physical quantities like the transverse momentum and the direction of charged particle tracks, during reconstruction. Fig. 2.1 shows how the transverse momentum measurement is affected by misalignment using estimated alignment precision scenarios as described the next section 2.1 and [13].

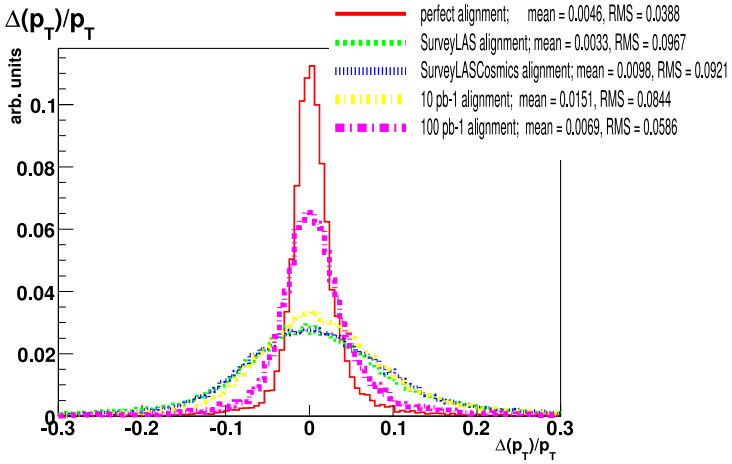


**Figure 2.1:** Expected impact of residual misalignment on tracking performance for muon tracks simulated at $p_{\mathrm{T,sim}} = 100$ GeV.

Depicted is the normalised difference in simulated $p_{\mathrm{T,sim}}$ and reconstructed transverse momentum $p_{\mathrm{T,reco}}$: $\frac{\Delta(p_T)}{p_T} = \frac{p_{\mathrm{T,sim}} - p_{\mathrm{T,reco}}}{p_{\mathrm{T,sim}}}$ for a sample of muons simulated at $p_{\mathrm{T,sim}} = 100$ GeV. This figure of merit is plotted for five scenarios: First, the geometry that was used to simulate the

trajectories (perfect alignment). Second and third, the two scenarios representing start-up using the hardware alignment system and survey measurements taken before the installation of the tracking system. The difference between the two is the use of cosmic muon tracks for alignment. The final two scenarios include the use of track based alignemnt employing $\mathcal{L} = 10$ pb$^{-1}$ and $\mathcal{L} = 100$ pb$^{-1}$ of collision tracks, respectivly. Note that even in the long term scenario utilising $\mathcal{L} = 100$ pb$^{-1}$ of data the residual misalignment is expected to have a significant effect on the transverse momentum measurement. For the CMS tracker there are three sources for corrections of the detector positions and orientations: After the assembly of the tracker subsystems the positions of some modules and larger support structures have been measured using photogrammetry (survey). Secondly, a laser alignment system (LAS) has been installed in the tracker. Using intense infra-red laser beams the position of bigger structures like the TEC disks can be monitored fast and independent of the measured tracks. This is done by measuring the positions where the laser beams traverse a subset of the strip tracker modules. Finally, the track based alignment is an algorithmic solution of the alignment problem using track measurements to determine the positions and tilts of all silicon modules (module level alignment). It is possible to use the outcome of the survey and photogrammetry measurements and laser alignment as a starting point reducing systematic errors and improving the number of measured input tracks, or even combine all methods in a single alignment procedure. However, in this thesis track based alignment is discussed only.

## 2.1 The Misalignment Scenarios

In order to estimate the systematic effects of misalignment on physics studies, the misalignment has to be taken into account during the reconstruction: The simulated positions of the hits are shifted before they are passed to the reconstruction procedure. The magnitude of sensor and support structure displacement was estimated for different degrees of knowledge. According to these estimates random gaussian distortions were applied to the tracking geometry [13]. In this procedure the positions are misaligned in all three Cartesian coordinates and tilted in three angles. For this thesis the scenario `surveyLASCosmics` for start-up conditions and the scenario corresponding to the result of alignment using information gathered taking $\mathcal{L} = 10$ pb$^{-1}$ of data are of interest.
The first scenario takes into account, that – in advance of collision data – tracks will be measured improving the precision of the laser alignment system and survey measurements. These tracks stem from muons generated in the upper atmosphere (cosmics) and charged particles generated in beam-gas or beam-collimator collisions during LHC machine tests (beam halo). The combination of the estimated misalignment of the support structures and the modules themselves lead to overall displacements $\Delta\boldsymbol{p}_{residual}$ (see Eqn. 2.5). Table 2.1 shows the RMS of $\Delta\boldsymbol{p}_{residual}$ along $r\Delta\varphi$ resulting from the combined misalignment.

| Subdetector | | PXB | PXF | TIB | TID | TOB | TEC |
|---|---|---|---|---|---|---|---|
| RMS of the overall module displacement | [µm] | 105 | 120 | 482 | 445 | 106 | 92 |

**Table 2.1:** Resulting RMS if module displacements $\Delta\boldsymbol{p}_{residual}$ (see Eqn. 2.5) estimated for the start-up scenario along $r\Delta\varphi$.

The second misalignment scenario of interest to this thesis emulates the alignment obtained using minimum bias and low mass resonances gathered in $\mathcal{L} = 10$ pb$^{-1}$ in addition to the

surveyLASCosmics scenario. Table 2.2 summarises the RMS of the module displacements $\Delta \boldsymbol{p}_{residual}$ along $r\Delta\varphi$ as defined in Eqn. 2.5. In this scenario the alignment of the pixel detectors as well as the tracker inner barrel and disk is improved significantly. On the other hand, it is estimated that the alignment precision of only the largest support structures of the tracker outer barrel is increased. For the tracker end cap no improvement at all was estimated. Both leads to a similar displacement of the modules when compared to the surveyLASCosmics scenario. For the two scenarios the misalignment was diced separately, which explains the numerical differences.

| Subdetector | | PXB | PXF | TIB | TID | TOB | TEC |
|---|---|---|---|---|---|---|---|
| RMS of the overall module displacement | [μm] | 61 | 17 | 225 | 295 | 102 | 104 |

**Table 2.2:** Resulting RMS for module displacements $\Delta \boldsymbol{p}_{residual}$ (see Eqn. 2.5) estimated for the $\mathcal{L} = 10$ pb$^{-1}$ scenario along $r\Delta\varphi$.

Both scenarios are embedded into general misalignment and miscalibration scenarios, taking into account tracker and muon system misalignment as well as the miscalibration of all tracking and calorimetry systems of the CMS experiment. The combined misalignment and miscalibration scenario designed for early data taking will be referred to as "start-up scenario" and the combination estimating the conditions after the analysis of $\mathcal{L} = 10$ pb$^{-1}$ of collision data will be called "$\mathcal{L} = 10$ pb$^{-1}$ scenario". Note that a third combined scenario is available, simulating the conditions after analysing $\mathcal{L} = 1$ pb$^{-1}$ of collision data (1PB_V2_RECO). While the calibration and alignment of the muon system and the calorimetry is changed with respect to the start-up scenario, for the tracker the same misalignment scenario (surveyLASCosmics) is used.

## 2.2 Track Based Alignment

Since track based alignment essentially is an optimisation problem one has to define an objective function. It is determined by global parameters $\boldsymbol{p}$ which denote the alignment corrections and local parameters $\boldsymbol{q}_j$ which denote the parameters of the fit for track $j$. Furthermore $f_{ij}(\boldsymbol{p}, \boldsymbol{q}_j)$ determines the position of the hit $i$ as predicted by the fit of track $j$. For given measured hits $y_{ij}$ with an uncertainty $\sigma_{ij}$, corresponding to the fit result $f_{ij}$, the objective function $\chi^2$ is defined by:

$$\chi^2(\boldsymbol{p}, \boldsymbol{q}_1 ... \boldsymbol{q}_N) = \sum_j \sum_i \frac{\left(y_{ij} - f_{ij}(\boldsymbol{p}, \boldsymbol{q}_j)\right)^2}{\sigma_{ij}^2} \tag{2.1}$$

Here N denotes the number of tracks and the sums cover all possible values. This, implies that the correlations between the single measurements are negligible.
The principle of track based alignment is based on the assumption that the $\chi^2$ of the track fit in a misaligned detector can be reduced by moving the measuring detector components (alignables) and thus the measurement point (hit) on them to a more appropriate position. Reversely the position of a hit and therefore the position and orientation of alignables is more appropriate if the $\chi^2$ of many independent track fits is minimal. In order to pinpoint the right combination of all possible shifts and rotations of more than 16000 alignables in the CMS tracker a large number of tracks is needed.

## 2.3 The MillePede II Algorithm

One of the algorithms suitable to solve this problem is MillePede II as described in [14] and [15] which is used throughout this thesis. It qualifies itself by the fast turnaround time and relatively low computational requirements for an alignment on module level. This is indispensable for a detailed study of alignment performance for different input samples. To reach these beneficial features the MillePede algorithm has been adopted to the high number of alignables.
It uses the Gauß-Newton method [16] to approximate the minimum of the general $\chi^2$ function 2.1 with respect to the used trackparameters $\boldsymbol{q}_j \in \mathbb{R}^\nu$ and the geometry $\boldsymbol{p} \in \mathbb{R}^{N_{alignables}}$. The residuals $z_{ij} = y_{ij} - f_{ij}(\boldsymbol{p}, \boldsymbol{q}_j)$ in the general $\chi^2$ function are linearised with respect to both the changes in the geometry and the track parameters:

$$\chi^2 \approx \sum_j \sum_i \frac{1}{\sigma_{ij}^2} \left( y_{ij} - f_{ij}|_{\boldsymbol{p},\boldsymbol{q}_j} + \frac{\partial f_{ij}}{\partial \boldsymbol{p}} \delta\boldsymbol{p} + \frac{\partial f_{ij}}{\partial \boldsymbol{q}_j} \delta\boldsymbol{q}_j \right)^2 \tag{2.2}$$

The minimum of this linearised problem is reached within one iteration of the Gauß-Newton method. According to this method the necessary corrections $\delta\boldsymbol{q}_j$ and $\delta\boldsymbol{p}$ to reach the minimum are the solution of $N_{alignables} + \nu \cdot N_{measurement}$ linear equations (normal equations). Here $\nu$ denotes the number of free parameters of the track fit. For example the standard helix track model yields $\nu = 5$, but methods such as the one described in 2.5 can lead to larger $\nu$. The number of aligned degrees of freedom is given by $N_{alignables}$ and the total number of hits on all tracks is given by $N_{measurement}$.
The fact that the local track measurements $j$ are all independent yields a specific form of the product of the Jacobian matrix $J$ of the vector of residuals $\sum_i \frac{y_{ij} - f_{ij}(\boldsymbol{p},\boldsymbol{q}_j)}{\sigma_{ij}}$ with respect to the free parameters $\boldsymbol{q}_j$ and $\boldsymbol{p}$:

$$J^T J \cdot \begin{pmatrix} \delta\boldsymbol{p} \\ \hline \vdots \\ \delta\boldsymbol{q}_j \\ \vdots \end{pmatrix} = \left(\begin{array}{c|ccc} \sum_j C_j^* & \dots & G_j & \dots \\ \hline \vdots & \ddots & 0 & 0 \\ G_j^T & 0 & \Gamma_j & 0 \\ \vdots & 0 & 0 & \ddots \end{array}\right) \cdot \begin{pmatrix} \delta\boldsymbol{p} \\ \hline \vdots \\ \delta\boldsymbol{q}_j \\ \vdots \end{pmatrix} = - \begin{pmatrix} \sum_j \boldsymbol{g}_j^* \\ \hline \vdots \\ \boldsymbol{\beta}_j \\ \vdots \end{pmatrix}$$

As set up in [15] the submatrix $\sum_j C_j^*$ and right hand side $\sum_j \boldsymbol{g}_j^*$ combine the derivatives of the global variables, the $\Gamma_j$ and $\boldsymbol{\beta}_j$ the derivatives and right hand side for the local parameters $\boldsymbol{q}_j$ and the cross terms are concentrated in $G_j$:

$$\begin{aligned} (C_j^*)_{kl} &= \sum_i \frac{\partial z_{ij}}{\partial p_k} \frac{\partial z_{ij}}{\partial p_l} \quad , \quad (\boldsymbol{g}_j^*)_k = \sum_i \frac{\partial z_{ij}}{\partial p_k} z_{ij}, \\ (\Gamma_j)_{kl} &= \sum_i \frac{\partial z_{ij}}{\partial q_{jk}} \frac{\partial z_{ij}}{\partial q_{jl}} \quad , \quad (\boldsymbol{\beta}_j)_k = \sum_i \frac{\partial z_{ij}}{\partial q_{jk}} z_{ij}, \\ (G_j)_{kl} &= \sum_i \frac{\partial z_{ij}}{\partial p_k} \frac{\partial z_{ij}}{\partial q_{jl}} \end{aligned}$$

Because the number of used tracks $N$ is of the order of millions and because of the numerous alignables the above matrix can not be inverted efficiently. Instead, exploiting the sparse block diagonal submatrix in the lower right, the global geometric corrections $\delta\boldsymbol{p}$ can be obtained solving a reduced set of linear equations

$$C \cdot \delta\boldsymbol{p} = -\boldsymbol{g} \tag{2.3}$$

$$\Gamma_j \cdot \delta\boldsymbol{q}_j = -\boldsymbol{\beta}_j \tag{2.4}$$

Where the matrix $C$ and the vector $\boldsymbol{g}$ are defined as the Schur-Complement [17]:

$$\begin{aligned} C &:= \sum_j C_j^* - G_j \cdot \Gamma_j^{-1} \cdot G_j^T \\ g &:= \sum_j \boldsymbol{g}_j^* - G_j \cdot \delta \boldsymbol{q}_j \end{aligned}$$

While MillePede II offers several methods to solve these equations, in this thesis only the Generalised Minimal RESidual (GMRES) [18] method is used.
Additional to this basic functionality MillePede II allows to use prior knowledge by adding for example survey information or another prior alignment as a starting point for the algorithm. This is done by iterating the Gauß-Newton method more than once, adding additional residuals to the $\chi^2$ function:

$$\chi^2_{pre} = \frac{\left(\boldsymbol{q}_{k-1} - \boldsymbol{q}_k\right)^2}{\sigma^2_{pre}}$$

Here the index $k$ denotes the $k$th iteration of solving equation 2.3, starting from the prior solution $\boldsymbol{q}_{k-1}$. $\boldsymbol{q}_0$ is set to the chosen prior knowledge. Thus, every degree of freedom is constrained ensuring the existence of a numerical solution to the alignment problem in the face of weakly constrained modes (see section 2.4). In iterations $k > 1$ the presence of the $\chi^2_{pre}$ limits the change of $\boldsymbol{q}_k$ for a single iteration to $\mathcal{O}(k_{max}\sigma_{pre})$. For studies in this thesis iterations are stopped at $k_{max} = 7$ and the presigmas $\sigma_{pre}$ developed for the start-up misalignment are used.
Finally, the impact of very large residuals that could otherwise distort the result can be reduced by multiplying the summand in equation 2.2 by a weight, transforming the least squares method into a method of M-estimates [19]. Similarly, tracks can be discarded if their $\chi^2_j$ does suggest that the initial track fit does not hold for the alignment reached during former iterations. Here $\chi^2_j$ is the contribution of the $j$th track to equation 2.2. For studies in this thesis the algorithm defaults were used: a track is dropped as outlier if its $\chi^2_j$ yields a probability of less than $p_{\min}(1) = 5.4\%$ in the first iteration. For subsequent iterations this cut-off is $p_{\min}(2) = 1.21\%$ and $p_{\min}(k)|_{k>2} = 0.27\%$ $\frac{4.5}{\sqrt{k}}$.
Non-linear components of the $\chi^2$ function can be taken into account by iterating the whole alignment, re-evaluating the derivatives in the linearized residuals.

## 2.4 $\chi^2$-Invariant Deformations

One central problem of track based alignment are possible large deformations of the detector that only slightly change the $\chi^2$ function 2.2. Thus, such deformations can not be corrected by an algorithm that minimises this function. A trivial example for this effect is a module that does not contribute any measurement to the alignment at all. The position and orientation of such a module will not be defined and in the best case it will remain at its initial position. The situation would be even worse if such a module contributes just a few wrongly measured hits as they are produced by electrical noise. Minimising the $\chi^2$, the algorithm will place the hypothetical module at a wrong position, since no further information regarding its position is available. Now the effect of the presigmas introduced in the previous section becomes obvious: Every shift and rotation of every module is constrained by at least one measurement and movements due to measurements with big uncertainties are suppressed to the order of the uncertainty of the prior knowledge. In this simple example the way to prevent such deformations is to make sure that several tracks of another track selection provide measurements on

the module.
In reality important $\chi^2$ invariant deformations are not shifts of single modules but correlated deformations of many modules. However, the considerations of the above example can be applied by choosing a base in the vector space of possible deformations that includes not the shift of a single module but the correlated deformation in question. If in this base the topology of the used track sample does not constrain the deformation, again the alignment algorithm might apply an unreasonable deformation that will minimise the $\chi^2$ function but not the module misplacement. The risk of such correlated deformations is that they directly bias measured quantities like the transverse momentum of all tracks or their distribution in $\varphi$. It has been shown in [2] that adding tracks with a different topology does in fact constrain such a deformation. Sources of these tracks are cosmic muon tracks traversing the detector vertically and tracks of beam halo muons that mostly are parallel to the beam line. The advantage of both is that they do not originate at the central collision vertex.
Fig. 2.2a shows an example for a large $\chi^2$-invariant mode of an alignment obtained from collision tracks only. Here a simplified version of the barrel region is depicted. By changing the direction of all tracks the layers of the detector can be shifted like a telescope along the $z$-axis. This effect is constrained by long straight tracks connecting the upper and lower half of the detector as shown in Fig. 2.2b. These tracks would show a kink if the telescope like shift was applied. This is not consistent with the assumed straight track model and leads to large additions to the overall $\chi^2$. Thus, the correlated shift is constraint.

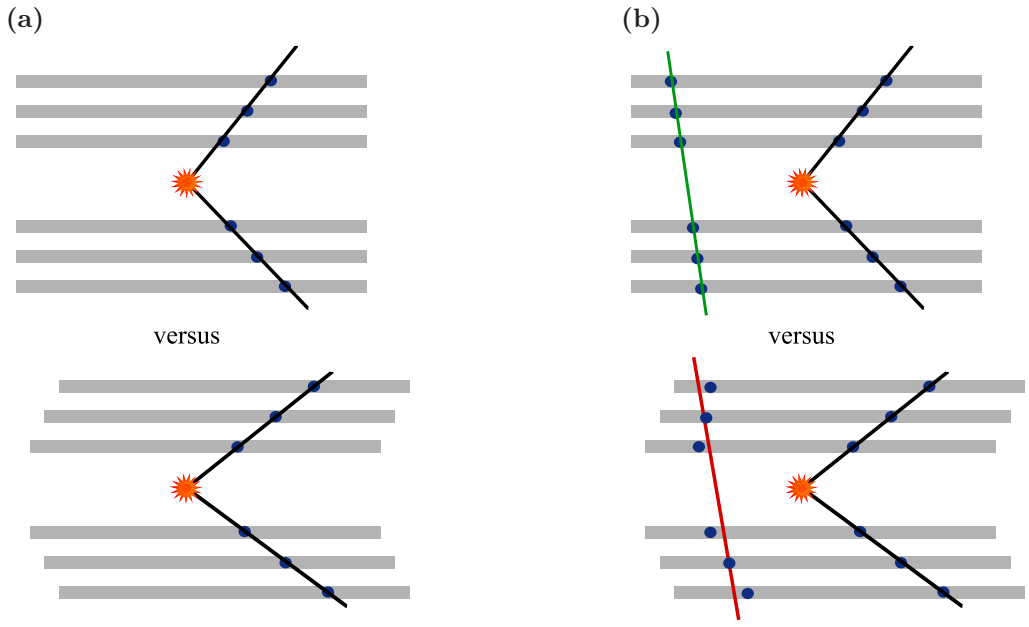


**Figure 2.2:** Example for large correlated deformations of a simplified detector. Tracks from collision events do not constrain telescope like deformations along the $z$-axis.

## 2.5 The Vertex and Mass Constraint

Another way to constrain weakly defined modes is to add more information. If e.g. the decay topology of a resonance like $Z \to \mu^+\mu^-$ is considered, the tracks come from a common vertex position and have a defined invariant mass. In the CMS Software Framework (CMSSW) [20] this information is used by a nine parameter fit for the whole decay [21], instead of the five parameter helix fit for each single track. This fit parametrises two tracks by the vertex

position, the momentum of the primary particle, the angle between the daughter particles in the mothers rest frame, and the mass of the mother particle. The resulting parameters and derivatives of the hit positions are passed to the $\chi^2$ function 2.2 as before. That way, changes to the geometry that contradict the assumed decay topology are suppressed. One consequence is that deformations which prevent the two tracks from intersecting are suppressed by the vertex term, while those deformations can be applied freely if two separate helix tracks are considered. In [2] this method was used on $Z \to \mu^+\mu^-$ events constraining $\chi^2$-invariant modes sheering and bending the detector in long term alignment.

## 2.6 Alignment Quality Estimation

In this section figures of merit (metrics) are defined, in order to compare sets of alignment constants quantitatively. As will be described in chapters 5 and 6 constants are derived using different track selections and the metrics are used to estimate the value of the track sample to alignment.
Generally, there are three possible sources for such metrics: First, information using track measurements such as the collection of track residuals in the tracker or its substructures can be monitored as well as the overall $\chi^2$ of the track fit.
Second, for simulated data the exact positions $\boldsymbol{p}_{design}$ and tilts of the detector components are known. Thus, the residual misplacement $\Delta\boldsymbol{p}_{residual}$ of modules - relative to the center of the tracker or a sub-detector - can be monitored:

$$\Delta\boldsymbol{p}_{residual} = \boldsymbol{p}_{design} - \boldsymbol{p}_{aligned} - \Delta\boldsymbol{c}_{sub-detector} \tag{2.5}$$

Here $\boldsymbol{p}_{aligned}$ denotes the module positions obtained from alignment. The relative misplacement of the center of the sub-detector $\Delta\boldsymbol{c}_{sub-detector} = \boldsymbol{c}_{design}^{sub-detector} - \boldsymbol{c}_{aligned}^{sub-detector}$ vanishes if the residual misalignment for the whole tracker is considered.
Lastly, the outcome of the track fit for independent track samples reconstructed using the alignment constants in question can be compared to the simulated track parameters. This provides insight into the systematic impact of misalignment on the quality of physics measurements.
While the first method is widely used for real data, the second and third are powerful tools analysing alignment performance using simulated data. As the last two methods compare to simulated values – known only for Monte Carlo samples – they are not affected by ambiguities like $\chi^2$ invariant modes.

### 2.6.1 Absolute Residual Misalignment

Exploiting the knowledge of the true geometry used during the simulation of events the difference to the aligned geometry (residual misalignment) can be computed. Since in this thesis alignment is done on module level, the residual misalignment of modules is of paramount interest. The residual misalignment $\Delta\boldsymbol{p}_{residual}$ is given in terms of differences between ideal and obtained module positions in cylindrical coordinates ($r\Delta\varphi$, $\Delta r$ and $\Delta z$). Due to the layout of the tracker, the $r\Delta\varphi$ coordinate has the biggest impact on tracking performance and thus is the most sensitive coordinate. Consequently it is of special interest in estimating alignment performance.
For example Fig. 2.3a shows the distribution of the simulated and aligned module positions along $r\Delta\varphi$ for the start-up scenario introduced in section 2.1. For an unbiased alignment, the mean of this distribution should be compatible with zero within its error, else a correlated distortion of the (sub)detector was introduced. Secondly, the RMS of the distribution measures

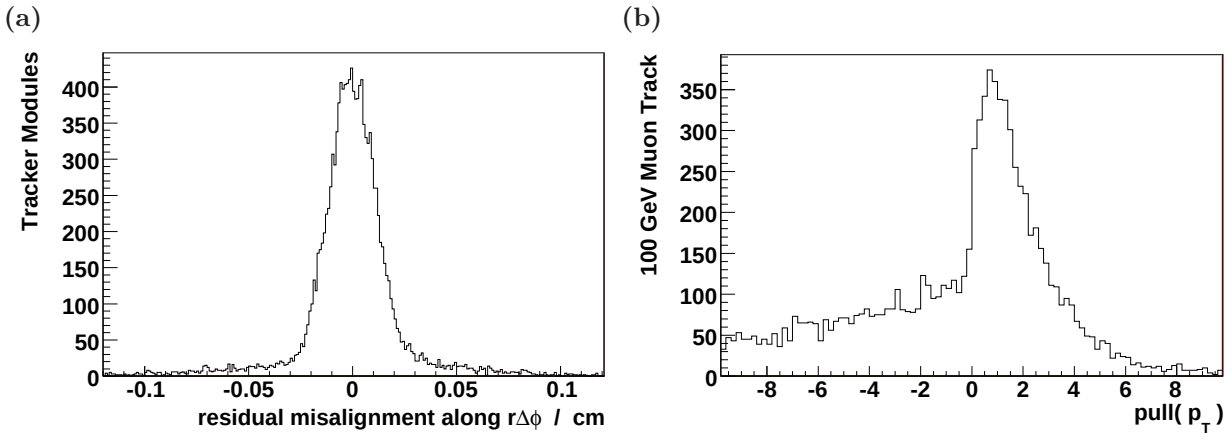


**Figure 2.3:** Distribution of the residual misalignment along $r\Delta\varphi$ for all modules of the tracker (a) and the pull of the transverse momentum measurement (see text) (b). Both featured in the start-up misalignment scenario.

the quality of alignment since it denotes the spread of module positions around their ideal locations.
As described in section 1.2.3, the individual sub-detectors of the tracker have different geometries, measurement resolutions, and positions relative to the interaction point. This leads to differences in alignment performance. Thus the residual misalignment of modules for each sub-detectors separately is of interest. For this comparison the overall misplacement of the sub-detector is neglected (see Equation 2.5). The mean of the residual misalignment distribution corresponds to the correlated distortion and the RMS of the same distribution corresponds to the alignment precision. In this way the bias and precision for any sub-detector and for different directions can be defined. For example the two metrics for the whole tracker and along $r\Delta\varphi$ are:

**Bias of the tracker module alignment along $r\Delta\varphi$:**

$$\langle r\Delta\varphi_{residual}\rangle = \sum_{\text{tracker modules}} \frac{r\Delta\varphi_{residual}}{n}$$

**Precision of the tracker module alignment along $r\Delta\varphi$:**

$$\text{RMS } r\Delta\varphi_{residual} = \sqrt{\sum_{\text{tracker modules}} \frac{(r\Delta\varphi_{residual} - \langle r\Delta\varphi_{residual}\rangle)^2}{n-1}}$$

Here, $r\Delta\varphi_{residual}$ denotes the component of $\Delta\boldsymbol{p}_{residual}$ along $r\varphi$. Further, $n$ represents the number of modules in the detector, in this case of the tracker.

### 2.6.2 Tracking Performance

Benchmark samples can be used to estimate the impact of the residual misalignment on tracking performance for any given set of alignment constants: a sample of similar tracks is reconstructed using the alignment constants in question. Since the ultimate goal of alignment is

to allow more precise reconstruction of tracks, increased precision in the reconstruction of the bench mark sample shows increased alignment quality. In contrast to the absolute residual misalignment this procedure takes the relevance of the deformation into account: deformations with large impact on tracking algorithms lead to large changes in this metric. Furthermore, the impact of residual misalignment on the reconstruction of distinct types of tracks can be studied, by comparing the results for different bench mark samples.
In this thesis a sample of 10 000 events, each containing two muons simulated with a transverse momentum of 100 GeV is used repeatedly. After reconstructing the tracks in the aligned geometry derived measurements like the transverse momentum $p_{T,\mathrm{reco}}$ can be compared to the simulated value $p_{T,\mathrm{sim}}$. Normalising to the error $\sigma_{p_T}$ obtained from the track fit the final metric, the $p_T$-pull in equation 2.6 is obtained. In the determination of $\sigma_{p_T}$ the simulated geometry is used.

$$\mathrm{pull}(p_T) = \frac{p_{T,\mathrm{reco}} - p_{T,\mathrm{sim}}}{\sigma_{p_T}} \tag{2.6}$$

Fig. 2.3b depicts the distribution of pull($p_T$) using the start-up scenario for reconstruction. The mean of this distribution quantifies a systematical bias, e.g. introduced by correlated deformations. Because of the normalisation in equation 2.6 the root mean square of the pull($p_T$)-distribution equals one if no additional systematic error is introduced by the residual misalignment. If it is greater than one a decrease of the $p_T$-resolution measurement is found. Furthermore, if the distribution is Gaussian, this implies that the RMS of this distribution is the factor by which the systematic error has to be increased to take the residual misalignment into account. This way two additional metrics are defined:

**$p_T$ Bias:**

$$\langle \mathrm{pull}(p_T) \rangle = \sum_{\text{reference tracks}} \frac{\mathrm{pull}(p_T)}{n}$$

**$p_T$ Resolution:**

$$\mathrm{RMS\ pull}(p_T) = \sqrt{\sum_{\text{reference tracks}} \frac{(\mathrm{pull}(p_T) - \langle \mathrm{pull}(p_T) \rangle)^2}{n-1}}$$

Here, $n$ denotes the number of tracks in the reference sample.
One should note that due to the large misalignment of the start-up scenario tails are observed in Fig. 2.3b.

# 3. The Computational Model for Alignment Track Selection

As introduced in section 1.2.4 a special data format named ALCARECO is defined as input to alignment. It contains only tracks, their hits and some additional information. In this way the 250 kB required for a fully reconstructed event is reduced to about 8 kB to 80 kB per event depending on the average number of tracks. Additionally only events that contain valuable information to solve the alignment problem are stored, reducing the number of events being read during alignment. Since the number of events used in alignment is of the order of ten million, this reduced data size evidently streamlines the process.
Another requirement for the ALCARECO production is to be able to run automatically on the Tier0 just after the first reconstruction of the events selected for alignment and calibration tasks. Here three types of selections are generated: high statistics, non collision, and resonance samples. Table 3.1 shows the different kinds of samples that are produced for alignment: First the high statistics samples used to determine the general positions of the modules. Secondly the non collision sample with their topology being drastically different of collision tracks should constrain weak modes significantly. Lastly, through the usage of the mass and vertex constraint the resonance samples will on the one hand help to suppress distortions along weak modes and provide very clean samples for long term alignment.

**Table 3.1:** Samples used for alignment, their HLT preselection, and cuts applied by the trackselector. For detailed a description of the HLT bits see [12] and [11]. See text for definition of the cuts applied by the trackselector.

| Process | Name | HLT preselection (logical OR) | Cuts by Trackselector | (average) contents |
|---|---|---|---|---|
| soft QCD | `TkAlMinBias` | `HLTMinBiasEcal HLTMinBiasHcal HLTMinBiasPixel` | $n_{Hits} > 8 \ \wedge \ p_T > 1.5$ GeV | $\approx 1.64$ tracks |
| mostly soft QCD | `TkAlMuonIsolated` | `HLT1MuonPrescalePt3 HLT1MuonPrescalePt5 HLT1MuonIso HLT1MuonNonIso` | $\Delta R(\text{jet}\|_{E_T>40 \text{ GeV}}, \text{track}) > 0.1 \ \wedge p_T >$ 2 GeV $\wedge$ global muon track | $\approx 1.31$ global muons |
| Air Showers | `TkAlCosmics` | – | $n_{Hits} > 18 \ \wedge \ p_T > 15$ GeV | $\approx 1.50$ muons |
| Beam Halo | `TkAlBeamHalo` | – | – | $\approx 3.6$ tracks |
| $Z \to \mu^+\mu^-$ | `TkAlZMuMu` | `HLT2MuonJPsi HLTBJPsiMuMu` | $p_T > 0.8\,\text{GeV} \wedge m_{\mu\mu} \in [70, 110]$ GeV $\wedge$ $\sum$ charge $= 0 \wedge$ global muon tracks | exactly 2 muons |
| $J/\psi \to \mu^+\mu^-$ | `TkAlJpsiMuMu` | `HLT2MuonUpsilon` | $p_T > 0.8\,\text{GeV} \wedge m_{\mu\mu} \in [3.0, 3.2]$ GeV $\wedge$ $\sum$ charge $= 0 \wedge$ global muon tracks | exactly 2 muons |
| $\Upsilon \to \mu^+\mu^-$ | `TkAlUpsilonMuMu` | `HLT2MuonZ` | $p_T > 0.8\,\text{GeV} \wedge m_{\mu\mu} \in [3.0, 3.2]$ GeV $\wedge$ $\sum$ charge $= 0 \wedge$ global muon tracks | exactly 2 muons |

## 3.1 Track Selection

The ALCARECO producers for track based alignment described in this thesis have entered the CMS software framework (CMSSW) in version CMSSW_2_0_0. Because the ALCARECO production is an automated and time-critical workflow, the developed software needed to be both robust and easy to maintain. To that end, all of the above selections are generated by one single module. This track selector module can be set up by configuration files; this way changes to the selection criteria or additional ALCARECO selections require no further software development.
Fig. 3.1 shows the conceptual outline of the track selector module. It instantiates three classes which consecutively apply different criteria to the selection of tracks. First, the `AlignmentTrackSelector` selects tracks checking basic properties. Second, the `AlignmentGlobalTrackSelector` applies cuts based on the whole event content incorporating measurements of the muon system and the calorimetry. Last, the `AlignmentTwoBodyDecayTrackSelector` selects combinations of tracks that with high probability stem from resonance decays. At the end only the information of the tracks that were selected by all subselectors is saved and the event is discarded if this set is empty.
Due to the large number of events recorded by the CMS detector it is deemed not feasible to run every selector on every reconstructed event. Instead, for each selector a set of HLT bits is defined that mark events of interest to the selector (see table 3.1). In this way the rate of events analysed by the track selectors is reduced.

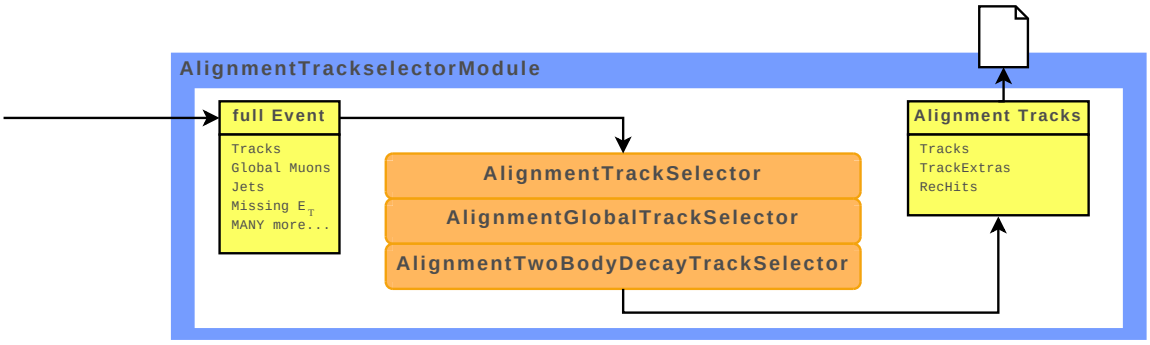


**Figure 3.1:** Structure of the ALCARECO producer as implemented in CMSSW_2_0_0.

### 3.1.1 The Basic Track Selection Criteria

There are two use-cases for this sub-selector: On the one hand, it applies thresholds for each track during the creation of the ALCARECO selections. On the other hand, it is used by alignment experts to impose even stricter selection criteria to tune the used track sample for the tackled alignment task and algorithm. This is possible, because only information of single tracks is required for the applied criteria.
Possible selection criteria are:

- transverse track momentum in range $p_{T,min} < p_T < p_{T,max}$
- track pseudorapidity in range $\eta_{min} < \eta < \eta_{max}$
- track azimuthal angle in range $\varphi_{min} < \varphi < \varphi_{max}$

- minimum number of associated Hits, minimum number of associated Hits on stereo modules, and minimum number of associated hits in sub-detectors (PXF, PXB, TIB, TOB, TID and TEC)
- only the $n$ tracks with the highest transverse momentum
- events containing $n_{min} < n < n_{max}$ tracks
- minimal absolute distance between hits associated to the track and hits not associated to the track.
- minimum charge deposited during measurement for each associated hit

### 3.1.2 The Global Selection Criteria

This sub-selector uses information from the whole event. Thus, it can not be used on ALCARECO selections. Its main feature is the usage of information from the muon system and the calorimetry. For the first, only tracks in the tracker that are associated to a track in the muon system are selected (global muons). Additionally a minimal number of such tracks can be required. The calorimeter information is exploited using jets reconstructed by the kt jet clustering algorithm with the cut-off parameter set to 0.6 rad [22]. A maximum number of jets above a configurable transverse energy threshold can be set. Another criterion is used for instance in the `TkAlMuonIsolated` selection: The isolation of a given track to the core of nearest jet is required. This limits the track's angular distance $\Delta R(\text{jet}, \text{track}) = \sqrt{\Delta\eta^2 + \Delta\varphi^2}$ to the direction of all jets above a transverse energy threshold $E_T > 40$ GeV. To avoid inter-dependencies of the alignment and calibration workflows the uncalibrated transverse energy is used for all criteria using jet information.

### 3.1.3 The Two Body Decay Selection Criteria

This last selector combines information of different tracks. The invariant mass of two selected tracks can be constrained to be $m_{min} < \sqrt{(E_1 + E_2)^2 - (\boldsymbol{p}_1 + \boldsymbol{p}_2)^2} < m_{max}$. This is most important for any resonance selection. Here the previous selection must yield exactly two tracks, otherwise the event will be dropped. Additionally, the charge of all selected tracks $\sum charge$ or its absolute value $|\sum charge|$ can be restricted to a certain value. The missing energy in the event can be taken into account using it instead of a second track in the mass range filter. Furthermore, the purity of the selected resonance sample can be improved by an acoplanar distance cut $||\varphi_1 - \varphi_2| - \pi| < \varphi_{max}$. This assumes that the boost of the mother particle is small in the transverse direction thus leading to $|\varphi_1 - \varphi_2| \approx \pi$.

## 3.2 Computing Challenges

In the years 2007 and 2008 there have been two large-scale computing exercises for the CMS experiment: the CMS Computing, Software, and Analysis challenges CSA07 and CSA08. While the goals of both differ and complement each other, in both challenges high statistics of data has been simulated. These simulations allowed to test the end-to-end work flow from triggering, over first reconstruction, the alignment and calibration tasks, up to physics analysis. However, since most of the events occurring during LHC bunch crossings will not be stored, it is not practical to first produce all these uninteresting events and then discard them right away. Due to their different emphasis this problem was tackled differently in both challenges.

The CSA07 challenge concentrated on physics analysis possible using the first $\mathcal{L} = 100$ pb$^{-1}$ of data recorded by CMS at LHC design conditions. To this end, trigger paths and data flow were modeled as accurately as technically possible, solving the above problem by introducing weights. These weights allowed to simulate minor amounts of data not likely to be used in physics studies while still reaching the goal of a highly accurate representation of the event selection process. Three collections of data sets – the so called "soups" – were produced to resemble the mixture expected to occur during real data taking. The split into three was neccesarry due to technical restrictions during the generation of the collecrtions. Together, they represent the Standard Model expectation for the first $\mathcal{L} = 100$ pb$^{-1}$ recorded at CMS.
The goal of CSA08 was centered around alignment and calibration tasks as well as early physics studies due in the very first weeks of data taking. Here LHC collisions are expected to reach center-of-mass energies up to 10 TeV for which two scenarios have been considered: The S43 scenario aims to simulate data gathered in runs with $43 \times 43$ bunches at a luminosity of $2 \cdot 10^{30}$ cm$^{-2}$s$^{-1}$ forming a sample of 1 pb$^{-1}$ integrated luminosity. The second scenario, which is studied more deeply in this thesis, is called S156. Data samples representing an integrated luminosity of 10 pb$^{-1}$ are simulated, obtained by collisions of $156 \times 156$ bunches in LHC at a luminosity of $2 \cdot 10^{31}$ cm$^{-2}$s$^{-1}$. The accumulated data represents about one month of LHC running with a 20% duty cycle. Further details are given in [23]. Contrary to the philosophy of CSA07, cuts at generator level were applied to minimize the number of simulated events that would be rejected by the triggering system. Furthermore no elaborate soups were created and the overlap between different samples was not studied in detail. These restrictions enabled the generation of high statistic samples needed for alignment and calibration studies like the one presented in this thesis.

## 3.3 Data Quality Monitoring

As for any automated production of data samples it is important to monitor the contents of ALCARECO samples in a fast and efficient way. In CMSSW this is possible using the Data Quality Monitoring (DQM) framework which allows the creation and management of monitoring histograms (ME) during the creation of the ALCARECO samples. These MEs are stored within the data samples and histograms are extracted and made available as soon as the data samples themselves arrive. This way, alignment experts will have a host of information available in order to decide on the mixture of track samples to be used for alignment. Also problems during data taking and erroneous software can be identified and dealt with in a timely manner.
The track based alignment ALCARECO workflow was the first offline ALCARECO workflow to implement the gathering of DQM histograms and thus was able to test it during CSA08. Since at that time the harvesting of DQM information was not implemented for the offline steps the histograms were extracted manually. Nevertheless the rest of the workflow, as well as the usage of this information, could be tested and several trivial problems were spotted and solved.
In an effort to share developed software and to reduce the necessary maintenance the `TrackingMonitor` developed by the tracking group as introduced in [24] is used for basic track information such as the transverse momentum or geometrical distribution of hits shown in Fig. 3.2. Afterwards, additional MEs have been created to monitor more specialised information such as the minimal distance of tracks and jets, the invariant mass of selected tracks and the distribution of hits shown in Fig. 3.3.

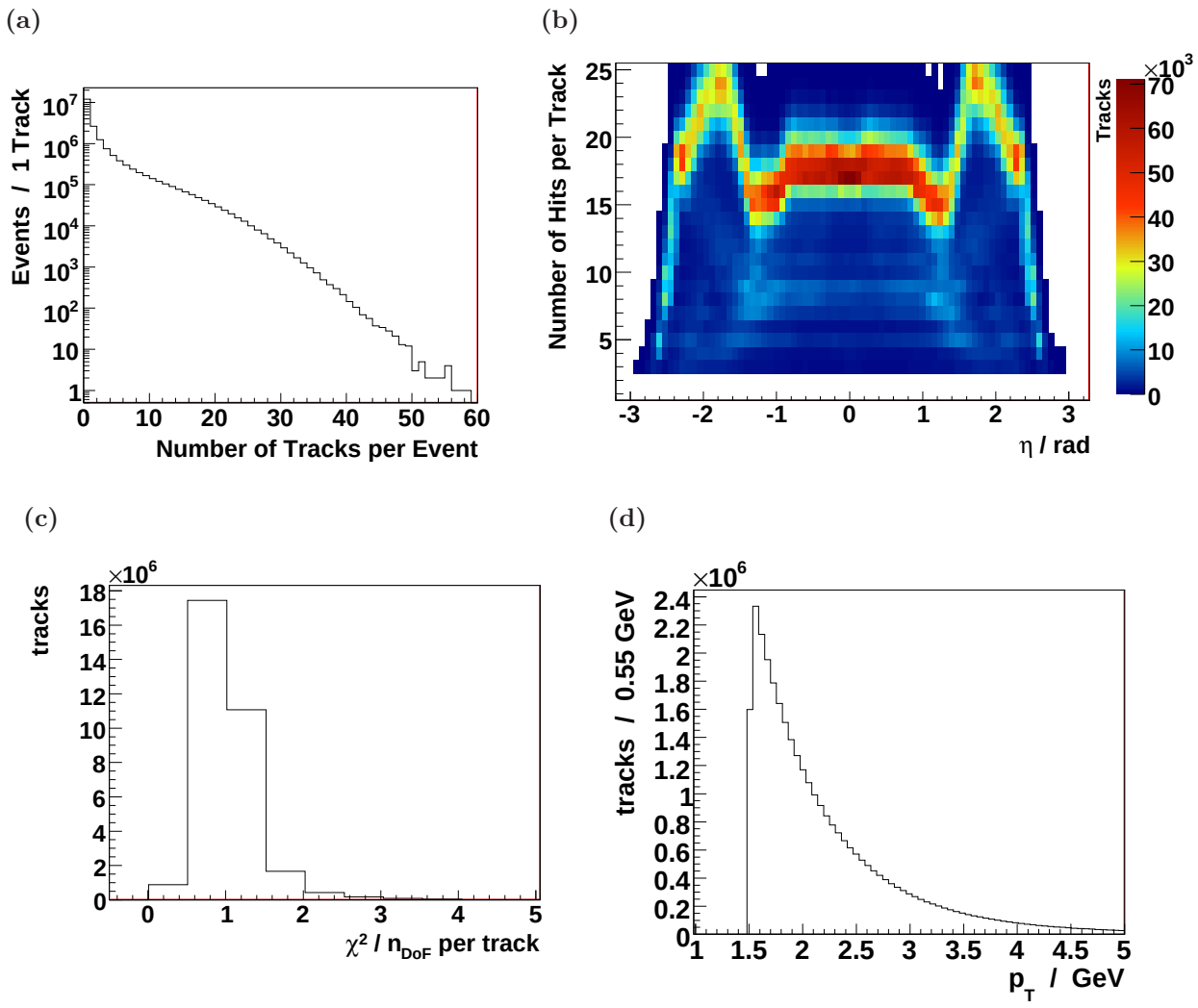


**Figure 3.2:** Examples of monitor elements available in `TrackingMonitor` analysing the CSA08 S156 `TkAlMinBias` selection.

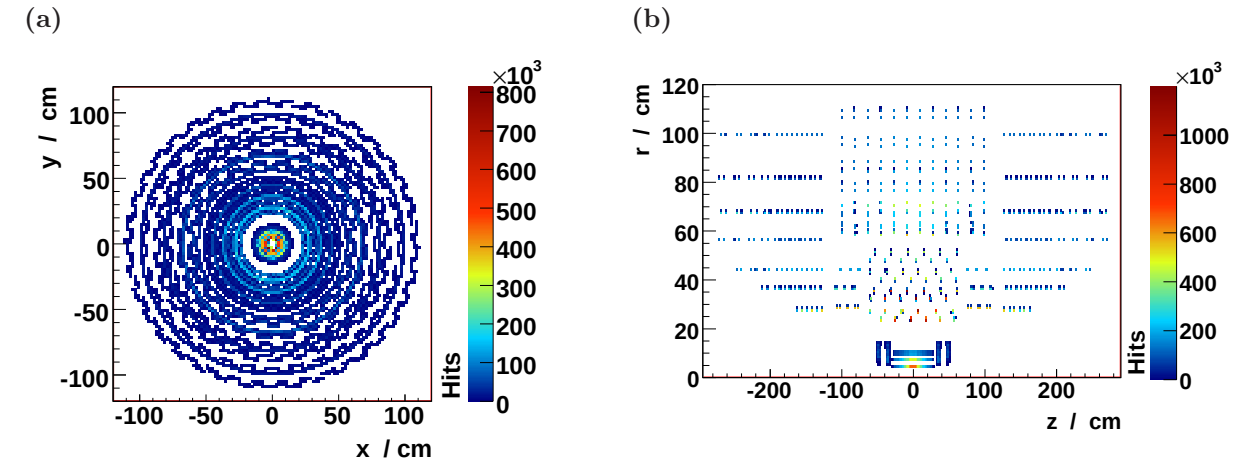


**Figure 3.3:** Examples of monitor elements available in `TkAlCaRecoMonitor` analysing the CSA08 S156 `TkAlMinBias` selection.

# 4. The Development of Realistic Track Selectors

For the long term alignment of the CMS inner tracking system large selections are needed, because it is made up out of more than 16 000 individual detectors. All of those have to be aligned with respect to their position and orientation (see chapter 2). Those selections should contain well measured tracks, since mismeasurements can lead to systematic distortions along $\chi^2$-invariant modes as introduced in section 2.4. Also the track model applied during reconstruction should be in good agreement with the selected tracks. This leads to a preference for minimally ionising particles such as high momentum muons. This has been shown in previous studies, using a combination of high momentum tracks from $Z \rightarrow \mu^+\mu^-$ and long tracks from muons produced in air showers (cosmics) [2]. The application of mass and vertex constraints as introduced in section 2.5 has proven to be a valuable asset reducing correlated distortions of the tracker. Because of the expected initial misalignment noise hits lead to distortions of the measured tracks. Errors during pattern recognition introduce tracks where no particle did traverse the detector (fake tracks). The known decay topology of physical decay processes makes it improbable that those tracks pass the selections below. Hence, the first step towards studying the track selection for alignment was to implement and test track selectors using the tools introduced in section 3.1. Those selectors are capable of separating the wanted signal from the background expected to be recorded during CMS operation.
The following sections describe the configuration of these tools to select the "golden" $Z \rightarrow \mu^+\mu^-$ and two similar event types, namely the decays $J/\psi \rightarrow \mu^+\mu^-$ and $\Upsilon \rightarrow \mu^+\mu^-$. The goal is to retain high purity without loosing too many tracks due to low efficiency. In contrast to similar selections for the luminosity measurement or electro-weak physics analyses no geometrical cuts must be applied because these would exclude whole regions of the tracker from alignment. Muons in the final state were chosen because of the reliable particle identification and the reduced interaction with detector material [25].

## 4.1 The CSA07 Monte Carlo Samples

In order to benchmark the track selectors, weighted samples from the CSA07 exercise were used, because only there background was available. These mixed samples, often referred to as "soups", are subdivided into:

**Chowder:** Electroweak decays of Z and W bosons as well as $t\bar{t}$-decays. For a better description of the jet spectrum, ALPGEN [26] was used to generate this sample.

**Stew:** Generated by PYTHIA [27], this sample contains lepton-enriched QCD as well as decays of bottom and charm mesons.

**Gumbo:** This event sample was generated by PYTHIA as well. It is not enriched and therefore contains minimum bias and QCD events containing photons and jets.

All samples were reconstructed using the misalignment expected after analysing the data gathered at $\mathcal{L} = 10\ \mathrm{pb}^{-1}$ (see section 2.1). The CSA07 HLT menu [11] was applied. For all studies shown in this chapter events were preselected by requiring the event to pass at least one muon HLT trigger. From the "Chowder" and "Stew" event sample only one million events were used to speed up the analysis. Since only about 150 thousand events of the Gumbo sample passed any muon HLT trigger criteria, all events were considered. The samples were reweighted according to their cross-sections and combined into a single benchmark sample. The weights were chosen in a way that the combined sample corresponds to $\mathcal{L} = 100\ \mathrm{pb}^{-1}$. Any efficiencies stated below are relative to this pre-selection, thus do not take muons into account that are not identified by the muon system. Since the efficiency of muon identification is more than 98% for most of the detector's $\eta$-range [6] and this pre-selection has no impact on comparison of selection criteria below.

## 4.2 The $Z \rightarrow \mu^+\mu^-$ Selection

The selection of events containing Drell-Yan produced Z bosons decaying into oppositely charged muons is especially beneficial for track-based alignment. The high invariant mass of the Z boson not only leads to large transverse momenta of the produced muons (Fig. 4.3a), but also ensures that the Z boson center-of-mass-system retains only a small boost. Thus, the angular distance of the emitted muons (Fig. 4.1) is high. Therfore, the two tracks of the selected events connect distant parts of the tracking system. Like with any resonance selection, mass and vertex constraints can be used to enhance alignment quality.

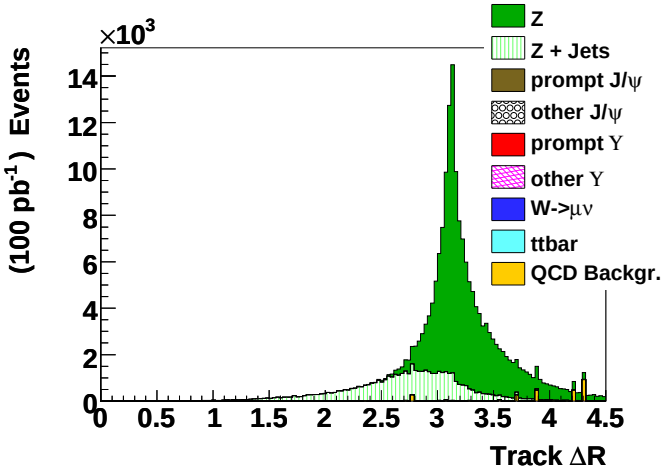


**Figure 4.1:** Distance $\Delta R = \sqrt{\Delta\varphi^2 + \Delta\eta^2}$ of muons in the $Z \rightarrow \mu^+\mu^-$ decay.

### 4.2.1 The Track Selection

The selection of tracks proceeds in two steps. First, the high level trigger is checked. In addition to the general muon trigger, the `HLT2MuonZ` bit has to be active (see Tab. 4.1). Note that since this bit is a muon trigger bit, no events were omitted due to the general muon trigger pre-selection. A comparison with other possible trigger selections is shown in the next section.

**Table 4.1:** High level trigger bits used for resonance selection, which were developed for the first year of LHC data-taking featuring a luminosity of $\mathcal{L} = 10^{32}\ \mathrm{cm}^{-2}\mathrm{s}^{-1}$. Rates are estimated to a precision of 10% of their value. The invariant mass of two muon tracks is denoted by $m_{\mu\mu}$. A cut on $m_{\mu\mu}$ requires at least two muons to be reconstructed by the HLT algorithm.

| Name | Rate [Hz] | Thresholds [GeV] |
|---|---|---|
| `HTL2MuonZ` | 0.1 | $p_T > 7 \ \wedge \ m_{\mu\mu} \in [80, 100]$ |
| `HLT2MuonJPsi` | 2.0 | $p_T > 3 \ \wedge \ m_{\mu\mu} \in [2.9, 3.3]$ |
| `HLTBJPsiMuMu` | 0.7 | $p_T > 4 \ \wedge \ m_{\mu\mu} \in [2.95, 3.25] \ \wedge$ sec. vertex (see text) |
| `HLT2MuonUpsilon` | 1.8 | $p_T > 3 \ \wedge \ m_{\mu\mu} \in [8, 12]$ |
| `HLT2MuonNonIso` | 12.3 | $p_T > 3$ for two muons |
| any Muon Bit | 61.3 | various |

The second step is a selection based on event properties. Two requirements remove most of the background: Firstly, the selected event has to contain exactly two tracks associated to a global muon. Fig. 4.2a shows that most of the signal events satisfy this requirement. For this figure only the high level trigger cuts are in place.
Secondly, a cut on the invariant mass $m_{\mu\mu}$ of the muon tracks is performed ($m_{\mu\mu} \in [70, 110]$ GeV). Fig. 4.2b shows the invariant mass of two tracks with all other cuts in place. It can be observed that a wide mass range still produces a pure sample. Note that during the high level trigger selection only a streamlined version of the pattern recognition and reconstruction algorithms is used. As a result, the invariant mass $m_{\mu\mu}$ calculated after the full reconstruction can be outside of the HLT-level cut.

To further increase the purity, in Fig. 4.3b it can be observed that the sum of the reconstructed charges can be constrained to zero without reducing the efficiency at all. Finally, the available statistical power for the soft QCD sample does not suffices to describe the transverse momentum spectrum of the QCD background to deduce a $p_T$ threshold. The `HLT2MuonZ` bit requires a transverse momentum of more than 7 GeV for muon candidates. This cut is applied after the streamlined high level trigger reconstruction. Using the full reconstruction different track might be found and selected. Tracks are considered to be of bad quality if they feature a transverse momentum below 1 GeV , because the tracking algorithms are not optimised low $p_T$ tracks [28]. As a precaution a minimal transverse momentum cut of $p_T > 0.8$ GeV is applied for all resonance selections.

From this analysis the final selection was deduced:

- the event has to be selected by the `HLT2MuonZ` HLT trigger
- exactly two tracks need to be associated to global muons

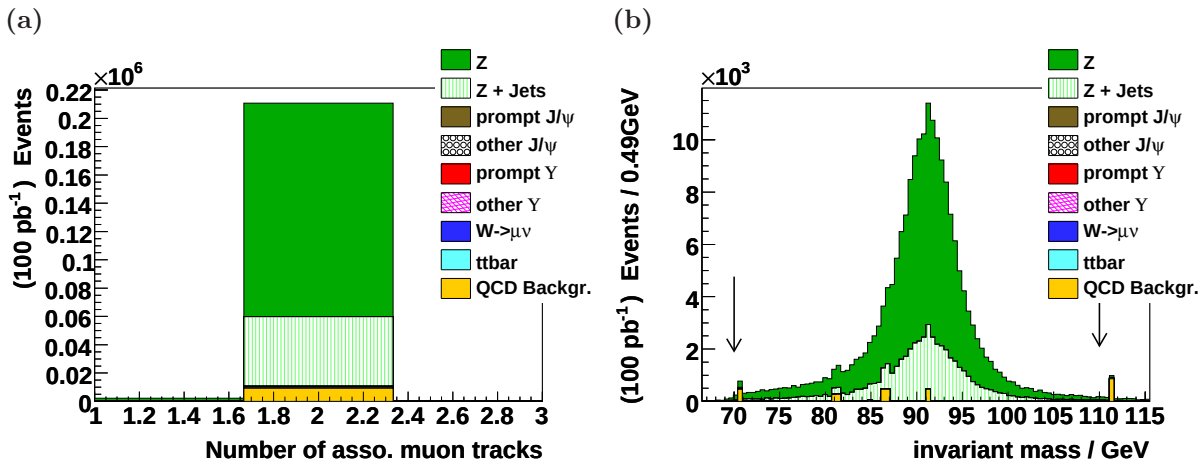


**Figure 4.2:** Number of global muons before any cuts (a) and invariant mass of two tracks after all but the invariant mass cut (b).

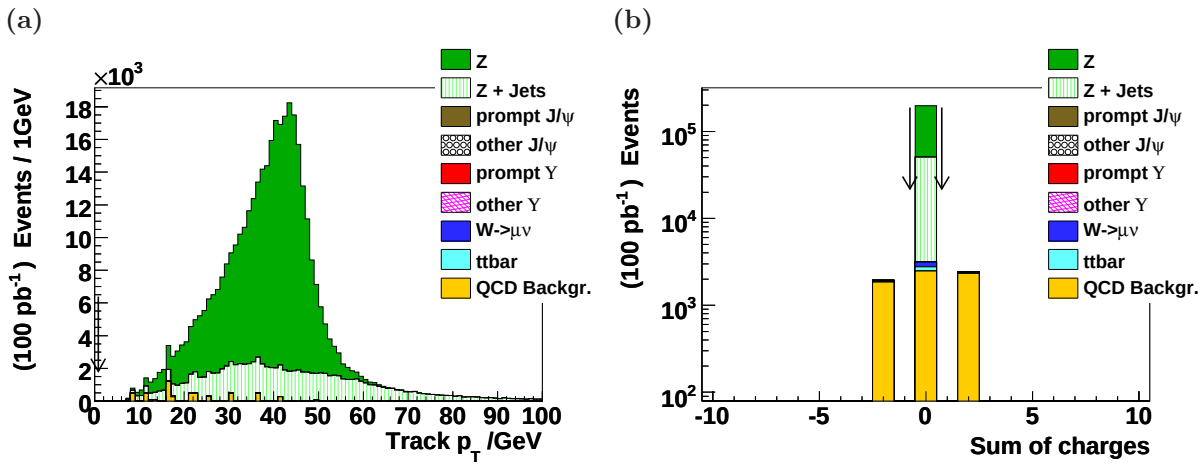


**Figure 4.3:** Transverse momentum of the tracks after all but the $p_T$-cut (a) and sum of the charges of the two tracks after all but the charge cut (b).

- the invariant mass of the two tracks has to be in the range of 70 to 110 GeV
- the sum of the charges of the two tracks has to be neutral
- each track has to be reconstructed with a transverse momentum of at least 0.8 GeV

By modifying these criteria the purity $\pi$ and the efficiency $\epsilon$ can be adjusted. Those are given by:

$$\epsilon = \frac{n_{\text{signal,selected}}}{n_{\text{signal}}} \qquad \pi = \frac{n_{\text{signal,selected}}}{n_{\text{selected}}}$$

Here $n_{\text{signal,selected}}$ denotes the number of selected signal events, $n_{\text{signal}}$ the number of signal events, and $n_{\text{selected}}$ the number of the selected events.
With the criteria listed above a purity of $\pi = 98.4\%$ at an efficiency of $\epsilon = 40.2\%$ is achieved.

### 4.2.2 Optimisation of High Level Trigger Selection

In this section the question is addressed whether adding further HLT bits might increase the selection efficiency without increasing the selected background significantly.
However, the gain in efficiency is compensated by higher computing needs: By adding HLT bits with high rate the number of processed events increases significantly. A strict limit of the express stream and subsequent analysis in the Tier0 (see section 3.1) forbids to choose events with a too high rate. To optimise the HLT selection, two HLT criteria are of special interest: First the `HLT2MuonZ` which requires two muons reconstructed with a transverse momentum of more than 7 GeV at HLT level. In addition, their invariant mass has to be in the region of 80 to 100 GeV. Secondly, the `HLT2MuonNonIso` flag which is set if two muons - each satisfying $p_T > 3$ GeV - are found in the event. The estimated rate at $\mathcal{L} = 10^{32}$ cm$^{-2}$s$^{-1}$ the first is 0.1 Hz and of the second 12.3 Hz [11]. This luminosity is expected during the first year of LHC data-taking. Note that during HLT reconstruction a stream lined version of track reconstruction is used which is not as precise as the full reconstruction. This leads to slight differences between cuts applied at HLT level and cuts applied in the studied track selection. Three trigger selections were studied:

**any:** analyse any event with a HLT muon flag. This is a bench mark selection which represents the maximum efficiency that is realistically possible

**loose:** analyse events that satisfy either the `HLT2MuonZ` or the `HLT2MuonNonIso` criteria

**tight:** analyse events that satisfy the `HLT2MuonZ` criterion

Fig. 4.4a shows that the difference in efficiency between the "loose" scenario of 41.6% and the "tight" scenario of 40.2% is negligible compared to the large difference in the trigger rates. To reach the "any" scenario, even higher rates of about 60 Hz would be needed. It was decided that the increase to an efficiency of 47.9% does not justify the additional computational effort. Fig. 4.4b shows the impurity $1 - \pi$, defined as the relative contribution of the backgrounds to the selection, for the three scenarios. A reduction of the QCD backgrounds for the "tight" scenario is observed.

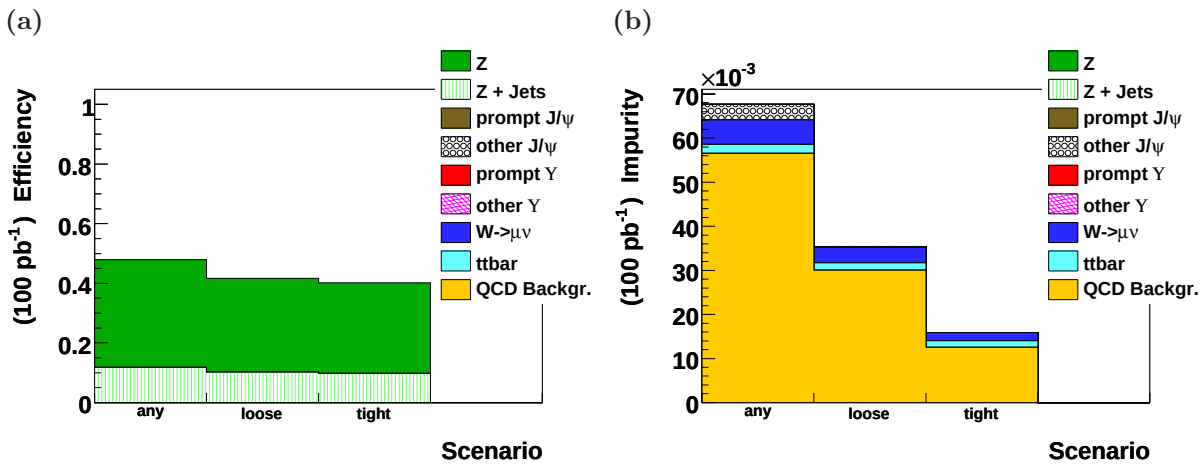


**Figure 4.4:** Impact of HLT selection on efficiency and impurity using the "any", "loose", and "tight" scenarios (see text).

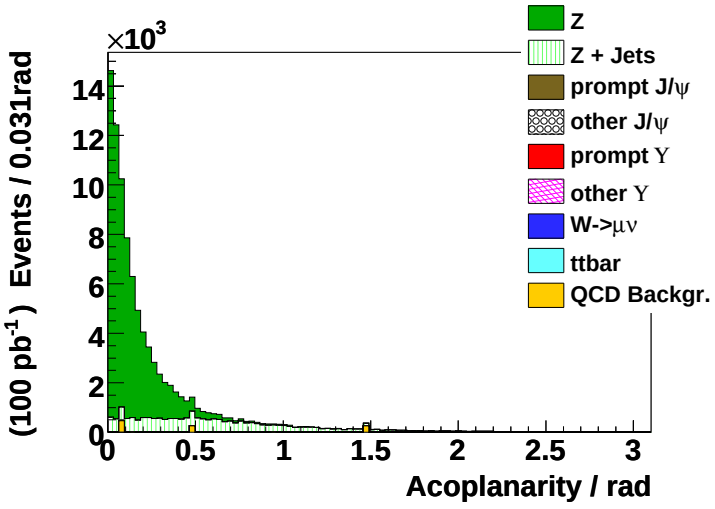


**Figure 4.5:** acoplanarity of the two tracks in the $Z \to \mu^+\mu^-$ selection.

### 4.2.3 An Additional Quality Criterion

While not applied in the final selection, the acoplanarity of the two selected tracks can be used to monitor the selection quality from data. Should differences between Monte Carlo simulation and reality lead to a higher background rate, the acoplanarity of tracks originating from background will be flatly distributed and easily distinguishable from the peak of the signal shown in Fig. 4.5.

## 4.3 The $J/\psi \to \mu^+\mu^-$ Selection

$J/\psi$ mesons can be produced promptly through gluon fusion - in leading order through a box diagram - or during hadronisation of final state quarks and gluons. Both are of potential interest for alignment, however in the plots a difference between prompt production and hadronisation is made. For alignment purposes the way of the production is irrelevant as long as the fit of the decay as described in section 2.5 is justified.
The first step is to select events based on a logical "or" of the `HLT2MuonJPsi` and `HLTBJPsiMuMu` HLT trigger bits, as described below. In the second step track information is used: All selected tracks are required to be associated to a track in the muon system. Because of the lower transverse momentum threshold of the imposed HLT selection, this does not remove as much of the background as the corresponding filter in the $Z \to \mu^+\mu^-$ study. Subsequently, both the rejected and the remaining background are larger (Fig. 4.6a). The range of the invariant mass of the two muon tracks is constrained to be in the range of 3.0 to 3.2 GeV. Fig. 4.6b shows the computed invariant mass after all other cuts are applied. It is observed that the detector resolution dominates the width of this distribution, leading to a more Gaussian shape that is broader than the natural width of the $J/\psi$ meson of 93 keV [25]. Nevertheless, a large fraction of the background can be rejected by this cut.

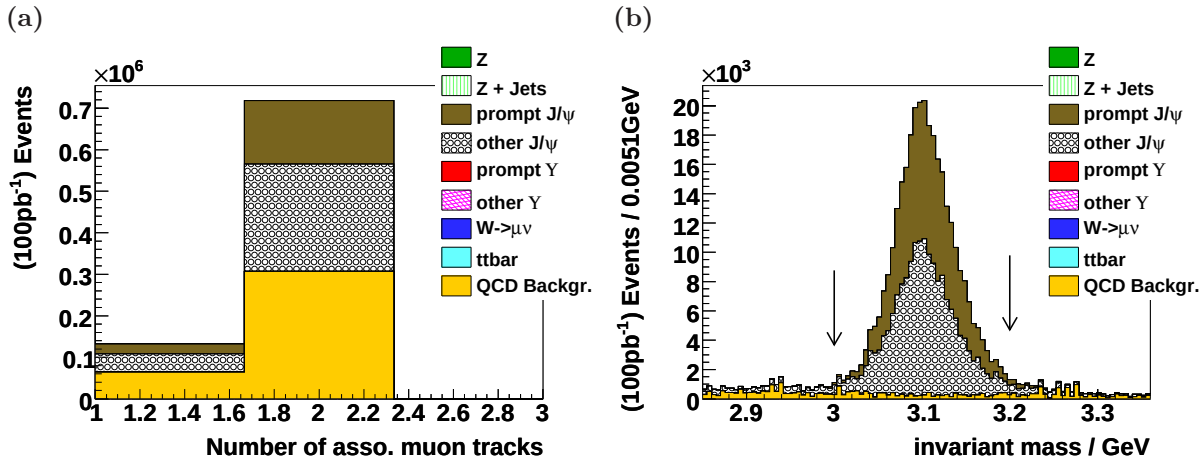


**Figure 4.6:** Number of global muons before any cuts (a) and invariant mass of two tracks after all but the invariant mass cut (b).

The chosen HLT preselection already applies a transverse momentum cut of 3 GeV. As can be seen in Fig. 4.7a, this cut removes part of the signal. Therefore, no higher threshold is imposed. For the high level trigger decision streamlined pattern recognition and track reconstruction algorithms are applied. Thus, differences to the final reconstruction are possible. As a precaution a minimal transverse momentum of $p_T > 0.8$ GeV is required for any selected track, to reduce the risk of using badly reconstructed tracks for alignment. As shown in

Fig. 4.7b a cut on the charge of the reconstructed meson has been found to have little effect. Nevertheless, a neutral reconstructed meson is required for sanity reasons.

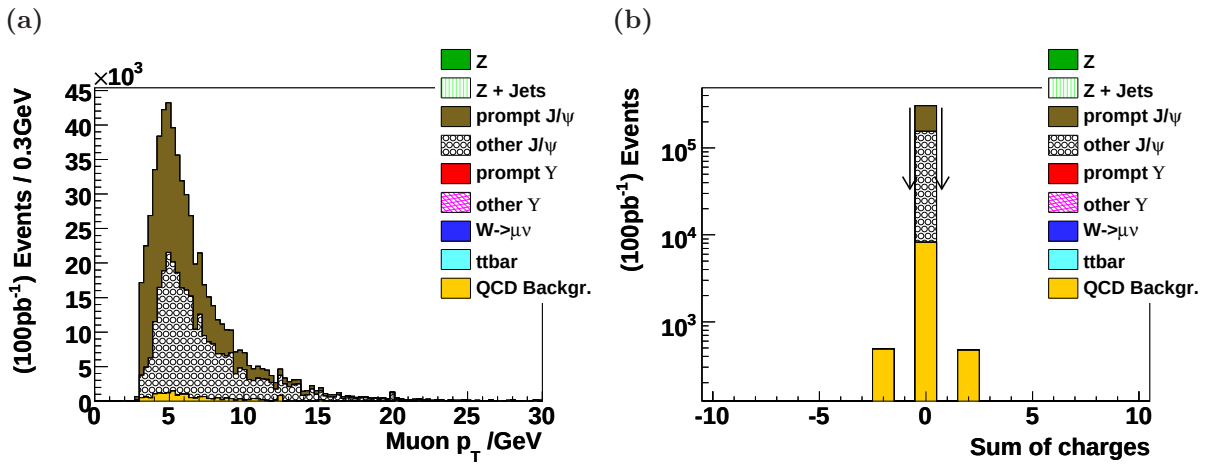


**Figure 4.7:** Transverse momentum of the tracks after HLT preselection (a) and sum of the charges of the two selected tracks after all cuts but the sum of charge cut (b).

From these considerations the following criteria for the `TkAlJPsiMuMu` selection were found:

- the Event has to pass either the `HLT2MuonJPsi` or the `HLTBJPsiMuMu` HLT filter
- exactly two tracks need to be associated to global muons
- the invariant mass of the two tracks has to be in the range of 3.0 to 3.2 GeV
- each track has to be reconstructed with a transverse momentum of at least 0.8 GeV
- the sum of the charges of the two selected tracks has to be neutral

Applying these selection criteria an efficiency of $\epsilon = 45.1\%$ and a purity of $\pi = 96.7\%$ have been found. Fig. 4.8b shows that the remaining background is dominated by hard QCD interactions.

### 4.3.1 Optimisation of High Level Trigger Selection

Again the effect of adding additional HLT selections was studied. Three high-level-trigger-based preselection scenarios were defined, similar to the ones introduced before:

**any:** analyse any event with a HLT muon flag

**loose:** analyse events that satisfy the `HLT2MuonJPsi`, the `HLTBJPsiMuMu` or the `HLT2MuonNonIso` criteria

**tight:** analyse events that satisfy either the `HLT2MuonJPsi` or `HLTBJPsiMuMu` critera

Two dedicated HLT selections for $J/\psi$ decays (`HLT2MuonJPsi` and `HLTBJPsiMuMu`) are available, where the second specialises on $J/\psi$-mesons produced in $b$-jets. Their estimated rates at a luminosity of $\mathcal{L} = 10^{32}$ cm$^{-2}$s$^{-1}$ are 2.0 Hz and 0.7 Hz, respectively [11]. For the "loose" and "tight" scenario a logical "or" of both trigger paths was used. The prompt $J/\psi$ path (`HLT2MuonJPsi`) requires a lower transverse momentum of 3 GeV and an invariant mass range of $m_{\mu\mu} \in [2.9, 3.3]$ GeV. The `HLTBJPsiMuMu` bit is set only if a point of intersection of the two muon tracks is found to be different from the primary vertex reconstructed using the pixel detectors. In addition to this vertex criterion a minimal transverse momentum of 4 GeV and an invariant mass in the range of 2.95 to 3.25 GeV is required.

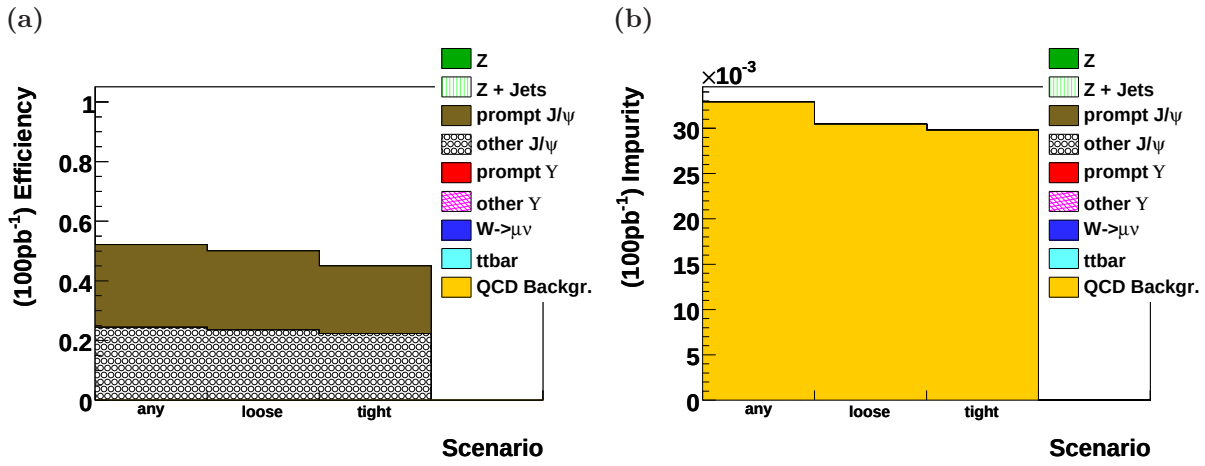


**Figure 4.8:** Impact of HLT preselection on efficiency and impurity using the "any", "loose", and "tight" scenarios (see text).

Figure 4.8a shows that the difference between the efficiency of 52.2% for the "any" case and 45% of the "tight" case are found to be small. On this bases it was decided that the difference does not justify the computational effort to analyse events with an expected rate of more than one order of magnitude higher than the "tight" scenario. In this case the slight differences in purity do not impact that decision.

## 4.4 The $\Upsilon \to \mu^+\mu^-$ Selection

Compared to the $J/\psi$ production, the rate of $\Upsilon \to \mu^+\mu^-$ is relatively low. This poses a challenge in the selection since the QCD background rate remains unchanged due to the similar signature. In Fig. 4.9a this effect can be seen in the signal to background ratio for the initial filtering for global muons. The natural width of 54.02 keV of the $\Upsilon$-meson is broadened by the detector resolution (Fig. 4.9b), as already seen in section 4.3 for the $J/\psi$-meson. Again the higher relative background is observed.

Even though the invariant mass of the $\Upsilon$-meson is higher than the $J/\psi$-meson, the transverse momentum distribution, given in Fig. 4.10a, suggests that only a precautionary low $p_T$ threshold should be in place to ensure reliable track reconstruction. Finally, some of the background can be cancelled by enforcing different charge of the two muons (Fig. 4.10b). This analysis leads to the following thresholds for the `TkAlUpsilon` selection:

- the event has to be selected by the `HLT2MuonUpsilon` HLT trigger bit
- exactly two tracks need to be associated to global muons

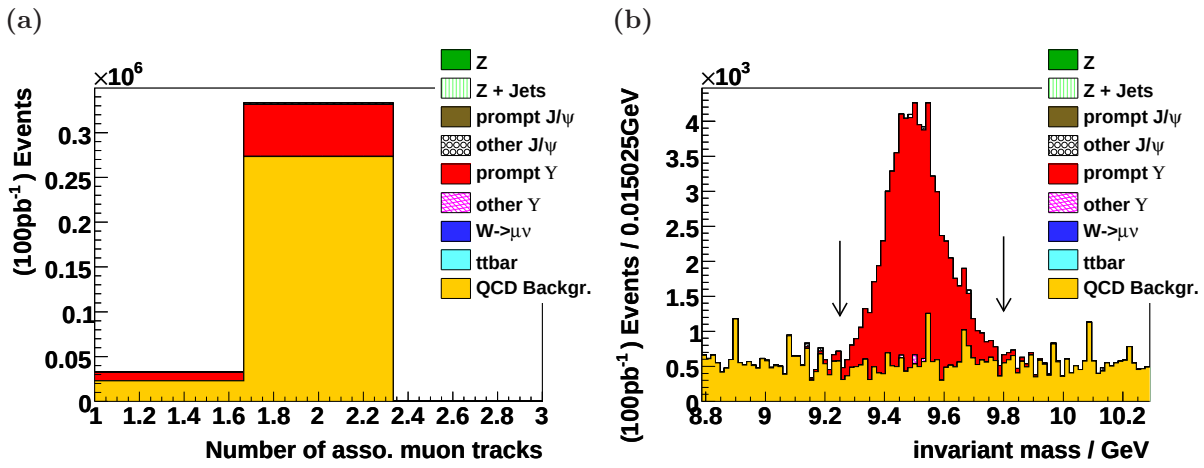


**Figure 4.9:** Number of global muons before any cuts (a) and invariant mass of two tracks after all but the invariant mass cut (b).

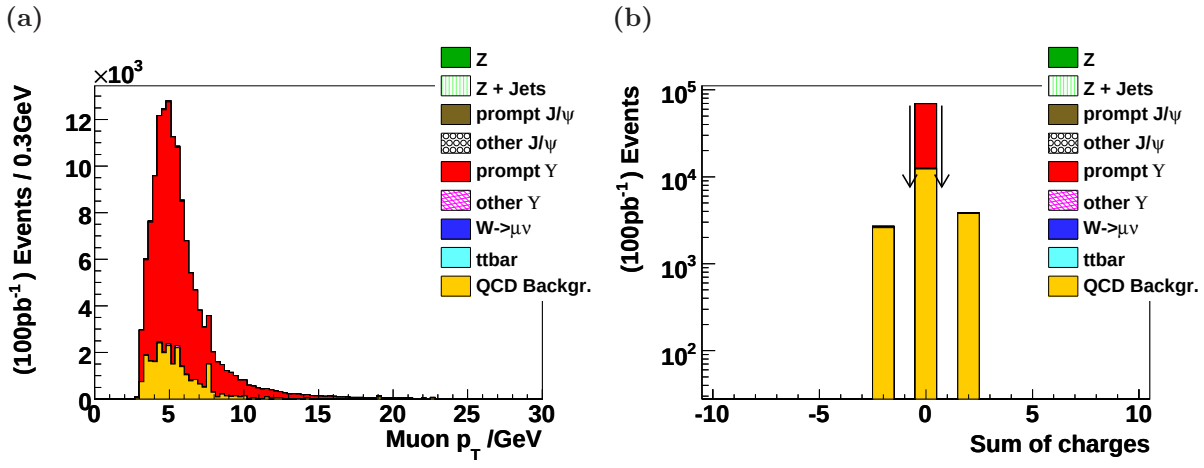


**Figure 4.10:** Transverse momentum of the tracks after HLT preselection (a) and the sum of charges of the the two tracks after all cuts but the sum of charges cut(b).

- the invariant mass of the two tracks has to be in the range of 9.25 to 9.8 GeV
- each track has to be reconstructed with a transverse momentum of at least 0.8 GeV
- the charge of the reconstructed $\Upsilon$-meson has to be neutral

Fig. 4.11a illustrates that with these criteria an efficiency of $\epsilon = 68.1\%$ is reached. The remaining background is again dominated by hard QCD events as shown in Fig. 4.11b. These lead to a final purity of $\pi = 82.1\%$.

### 4.4.1 Optimisation of High Level Trigger Selection

Finally, the three scenarios "any", "loose", and "tight" were studied to optimise the HLT preselection.

**any:** analyse any event with a HLT muon flag

**loose:** analyse events that satisfy either the `HLT2MuonUpsilon` or the `HLT2MuonNonIso` criteria

**tight:** only analyse events that satisfy the `HLT2MuonUpsilon` criterion

This time `HLT2MuonUpsilon` was used as dedicated HLT path in the "loose" and "tight" scenario. A transverse momentum exceeding 3 GeV for both muons and an invariant mass in the range of 8 and 12 GeV are required. The estimated rate of 1.8 Hz again is much lower than the about 60 Hz of the "any" case.
As Fig. 4.11a illustrates the improvement in efficiency using looser HLT criteria is small. As before the "tight" scenario was chosen because of its 30 times lower rate.

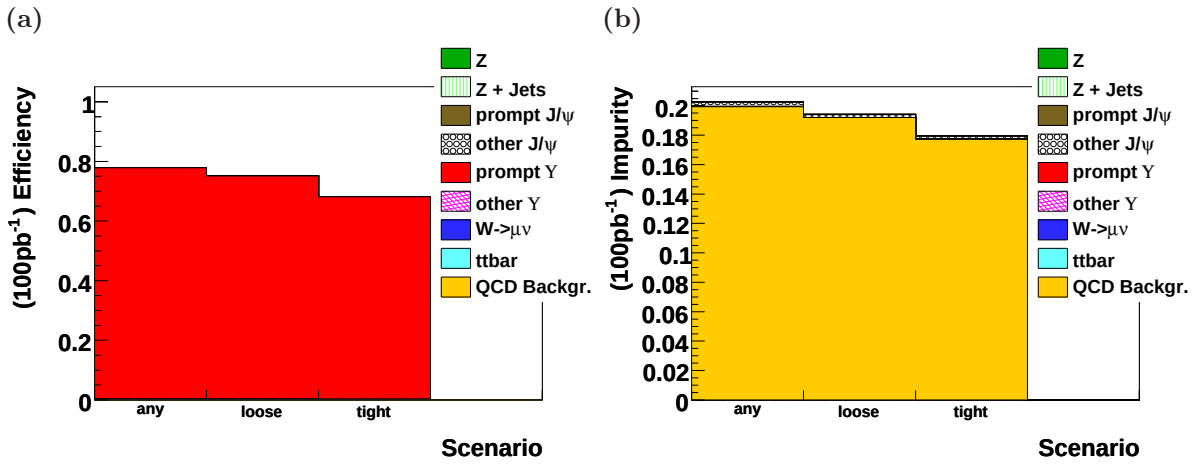


**Figure 4.11:** Impact of HLT preselection on efficiency and impurity using the "any", "loose", and "tight" scenarios (see text).

## 4.5 Test of the Selectors

The above selectors have been successfully applied during the CSA08 exercise (see section 3.2). This test showed that the developed software is stable and able to be operated in full scale selection on Tier0. Also it has been shown that the chosen HLT selections keep the rate of analysed events within the limits of the available computing power. The applied misalignment and calibration scenarios, the simulated luminosity, and the center of mass energy differ in the CSA07 and CSA08 exercises. Additionally during the CSA08 exercise not all backgrounds were simulated. As a result the efficiencies and purities can not be directly compared. Nevertheless, the high purity of the selection was confirmed. The simulated backgrounds were: a muon enriched soft QCD sample with $\hat{p}_T > 30$ GeV, a $W \to \mu\nu$ sample, QCD samples with $\hat{p}_T > 20$, 30, 50, 80, 110 and 150 GeV. Out of those no more than 0.0016% of the events were selected.

## 4.6 Conclusion

- pure selections were developed as shown in table 4.2
- for all selections dedicated HLT bits are used to decrease the necessary computational effort.
- during the CSA08 exercise it has been shown that the introduced selectors can be operated in the Tier0 centers and at event rates expected at LHC start-up

**Table 4.2:** Efficiencies and purities of available resonance selections

| Process | Efficiency [%] | Purity [%] |
|---|---|---|
| $Z \to \mu^+\mu^-$ | 40.2 | 98.4 |
| $J/\psi \to \mu^+\mu^-$ | 45.1 | 96.7 |
| $\Upsilon \to \mu^+\mu^-$ | 68.1 | 82.1 |

# 5. Data Samples Offering High Statistics

Usually, well measured and identified muon tracks like from the $Z \rightarrow \mu^+\mu^-$ decay are used for track-based alignment. But at the beginning of the CMS data taking where alignment is expected to apply the largest geometry corrections, the number of those "golden channel" muons will be very limited. Therefore, as described in section 3.1, track selections were devised that provide high statistics for initial alignment during LHC start-up. In the following sections, a first study of the statistical impact and the dependency of the alignment on possible cuts during the selection process are shown. For these studies, data from the CSA08 S156 scenario have been chosen and used statistics are limited by what can be collected in $\mathcal{L} = 10$ pb$^{-1}$. Furthermore, this scenario utilises the joint S43 and S156 HLT trigger menu used during the computing challenge for the necessary preselection of events [12]. Note that differences to the menu used during actual LHC start-up can not be studied here. Finally, following the goal of a study for the track selection at $\mathcal{L} = 10$ pb$^{-1}$, the global misalignment and miscalibration scenario representing the knowledge after analysing $\mathcal{L} = 1$ pb$^{-1}$ worth of data (`1PB_V2_RECO`) has been applied. The misalignment in this scenario is identical to the misalignment in the S43 scenario. Thus, taking the reduced statistics at $\mathcal{L} = 1$ pb$^{-1}$ into account, results obtained in this study are applicable to the S43 scenario as well. Especially the results for the minimum bias selection apply for both the S156 and the S43 scenario, since the number of available tracks is dominated by the rate data can be taken by CMS. The prescaling in the S156 scenario is higher and the resulting selection for both scenarios are nearly identical.
All alignments presented in the following sections are at module level and span the whole tracker. They have been performed in two spatial coordinates u, w and the most sensitive rotation $\gamma$ along the normal of the module plane (Fig. 5.1). For stereo modules and modules in the pixel detector the third spatial coordinate v has been aligned as well.
To study the optimisation of track selection, the successful selection criteria of the ALCARECO producers as they have been used during CSA08 were applied as a starting point. The full set of those producers is given in Tab. 3.1 in section 3.

## 5.1 Statistical Impact of Datasamples

Given the unprecedented size of the alignment problem of the CMS inner tracking system, the size of the track sample used in track-based alignment plays an important role for the

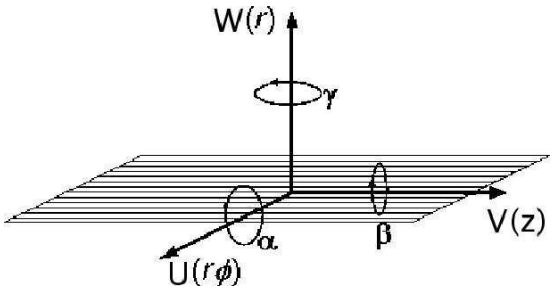


**Figure 5.1:** Definition of the coordiantes in which alignment corections are applied [13]. The horizontal lines indicate the direction of strips and the longer dimension of pixels for the strip tracker and the pixel detector, respectively.

alignment precision. The following section describes alignments with varying size of the track sample used as input to the algorithm.
The error on the module position measured during the alignment process is expected to decrease proportional to $\frac{1}{\sqrt{n}}$ with respect to the size $n$ of the track sample. Accordingly, alignment metrics $\mathcal{M}$ such as the RMS of the geometrical displacement have been found to follow a similar empirical distribution:

$$\mathcal{M}(n) = \mathcal{M}_0 + \frac{q}{\sqrt{n - n_0}} \tag{5.1}$$

Here, $\mathcal{M}_0$ denotes the best value of the metric achievable using this sample and set of aligned degrees of freedom. This is on the one hand affected by correlated $\chi^2$ invariant distortions that can not be determined by tracks from the given track sample. On the other hand, misalignment along degrees of freedom that are not included in the alignment can not be fully compensated by shifts along the aligned degrees of freedom. Note that a quadratic sum of $\mathcal{M}_0$ and $\frac{q}{\sqrt{n-n_0}}$ does not model the alignment metrics shown later in this chapter. The initial alignment is represented by the negative starting point $n_0$. Finally, the quality of a given sample for this metric is the slope $q$, which is antiproportional to the benefit of the sample to the alignment. Systematic effects, such as errors due to linearisation and parametrisation of the tracking model lead to the asymptotic approach of the alignment to $\mathcal{M}_0$. At this point, additional measures like reprocessing the dataset with the alignment gained so far to improve pattern recognition and to avoid linearisation effects of the $\chi^2$ function have to be taken, which are not part of this thesis.

### 5.1.1 The `TkAlMinBias` Sample

The `TkAlMinBias` selection aims to choose any track that could be beneficial to alignment. To reject empty events from the analysis at least one of three high level trigger conditions has to be satisfied:

`HLTMinBiasPixel` requests at least two tracks in the pixel detector, separated by a cone of $\Delta R >= 1$

`HLTMinBiasEcal` requests either a single cluster of 2 GeV or at least two clusters of at least 1 GeV in the electromagnetic calorimeter (These energies are measured by the level 1 trigger and are uncalibrated)

`HLTMinBiasHcal` requests any level 1 trigger bit with thresholds above 20 GeV in the hadronic calorimeter

From this high level trigger selection any reconstructed track that features a transverse momentum above 1.5 GeV and at least 8 hits is chosen for the `TkAlMinBias` selection (see Tab. 3.1). The impact of these cuts on alignment quality is studied in a later this chapter. That way, about 32 million out of about 350 million tracks in the unfiltered sample are selected. It is the sample with the highest number of available tracks.
The speciality of the minimum bias sample is that its size is not limited by the event rate, but by the possibility to record data. Therefore it is heavily dependent on the trigger setup and prescaling applied during data taking. Possibilities to optimise HLT-level selection are given below.

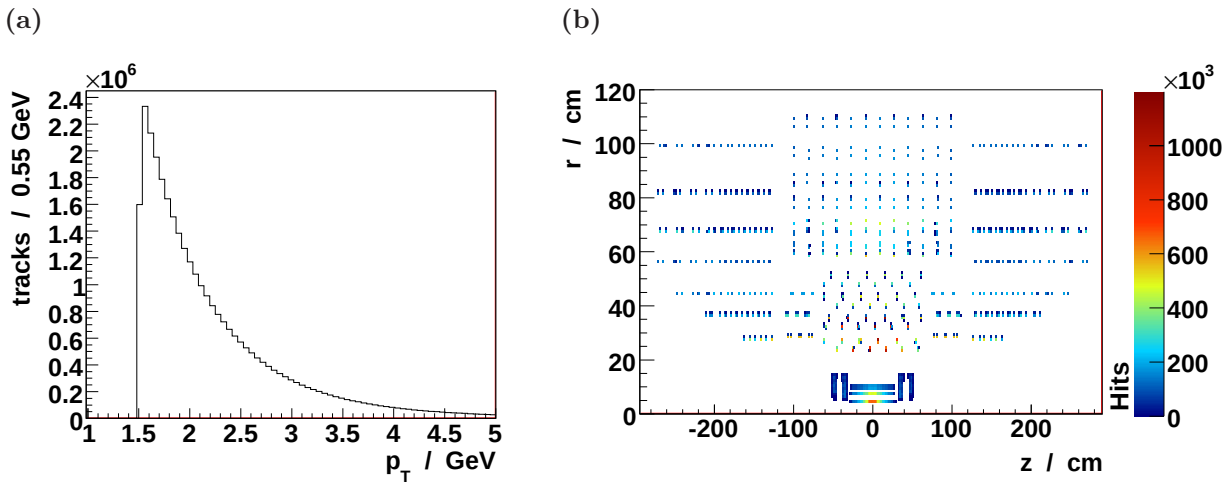


**Figure 5.2:** (a) The transverse momentum spectrum of the `TkAlMinBias` selection. The spectrum ends at $p_T = 1.5$ GeV because of the applied quality cut. (b) The position of hits on tracks in the `TkAlMinBias` selection.

Fig. 5.2a shows the transverse momentum spectrum of the sample. About 90% of the tracks are measured to have a $p_T$ below 3.2 GeV leading to a high correlation between the chosen minimal transverse momentum and the number of tracks available to alignment. In Fig. 5.2b, a map of hit positions used in the track fit is depicted. Positions are given in the $r$-$z$ plane of the cylindrical coordinate system and the distribution is integrated over the azimuthal coordinate $\varphi$. Since in the minimum bias sample the tracks are uniformly distributed in the pseudo-rapidity $\eta$, a steep gradient of hits from the interaction point outwards is observed. Because of the high granularity of the pixel detector, this gradient is more visible than in the strip tracker. Nevertheless, more hits are observed in the tracker inner barrel ($r \in [25.5, 49.8]$cm and $z \in [-70, 70]$cm) than in any other sub-detector. Note that according to this distribution modules in the forward pixels are rarely traversed by a measured track.

### The Position Resolution in $r\Delta\varphi$

Because the coordinate along the bending plane of the magnetic field $r\Delta\varphi$ can be measured with the highest precision, residual misalignment along this coordinate has the largest impact on tracking performance. Thus, the prime figure of merit to evaluate the performance of the alignment is the residual misplacement of modules along $r\Delta\varphi$.

Fig. 5.3 shows the evolution of the average displacement (a) and the width of the displacement distribution (b). The error bars in these and all other figures in the following studies denote

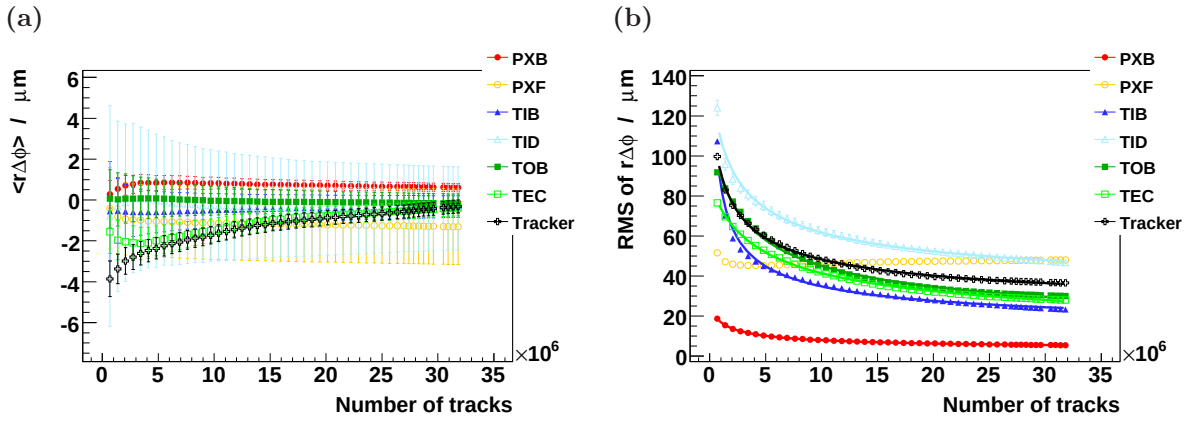


**Figure 5.3:** Evolution of the residual misalignment along the most sensitive coordinate $r\Delta\varphi$ for different selection sizes. Samples are enlarged by adding events. (a) Bias of the module alignment along $r\Delta\varphi$ (average misplacement of modules in the detector). (b) Precision of the alignment along $r\Delta\varphi$ (RMS of the module displacement). The result of a fit to Eqn. 5.1 is given for all sub-detectors but the forward pixels. Error bars denote statistical errors (see Eqn. 5.2).

the statistical error $\delta$ as expected from the distribution of the studied metric. For a mean $\langle\mathcal{M}\rangle$ and a RMS $\sigma_{\mathcal{M}}$ these are defined as:

$$\delta_{\langle\mathcal{M}\rangle} = \frac{\langle\mathcal{M}\rangle}{\sqrt{n}} \quad \text{and} \quad \delta_{\sigma_{\mathcal{M}}} = \frac{\sigma_{\mathcal{M}}}{\sqrt{2n}} \tag{5.2}$$

Here $n$ denotes the number of modules in the detector. This way, since common tracks are used for all alignments, the correlation between two data points is not taken into account. Note that there is no estimate for systematic errors. Fig. 5.3a shows that within their errors the residual misalignment is well centered along $r\Delta\varphi$. Also the evolution for all tracker modules converges towards very small mean displacements and improves steadily even after adding more than 10 million tracks to the alignment.
As expected, the resolution (Fig. 5.3b) of the alignment along $r\Delta\varphi$ improves following equation 5.1 for most subdetectors and the tracker as a whole. Solely the forward pixel detectors show a large RMS that does not improve with additional tracks. Comparing to Fig. 5.2b this can well be attributed to modules that are rarely hit in this subdetector.
Tab. 5.1 summarises the outcome of the fit using equation 5.1 and the alignment precision achieved using the full sample. Comparing the first two columns suggests that an even higher precision could be reached with more than the about 32 million tracks provided by the $\mathcal{L} = 10$ pb$^{-1}$ scenario. Here the chosen metric $\mathcal{M}$ is the RMS of the residual module displacements along $r\Delta\varphi$. $\mathcal{M}_0$ denotes the limit for an infinite track sample (see Eqn. 5.1) and $\mathcal{M}_{\text{last}}$ denotes the resolution actually achieved using the full track sample. Also the comparison of the detector subsystems shows that the spread of the forward pixel modules leads to the lowest precision in the whole tracker. Further investigation confirms that the effect spans the bulk of the PXF modules and not only a few of them at very high $\eta$ regions.

### 5.1.2 The Drawbacks of TkAlMinBias

Since the `TkAlMinBias` selection contains any track that has been reconstructed with a $p_T > 1.5$ GeV and more than 8 hits, alignment quality is expected to suffer from low track quality. Not

**Table 5.1:** Results of the statistical evolution of the module alignment precision along the most sensitive coordinate $r\Delta\varphi$ (RMS of $r\Delta\varphi$). Tracks from the selection were used for alignment. $\mathcal{M}_{\text{last}}$ denotes the best module alignment precision.

| Subdetector | $\mathcal{M}_0$ [µm] | $\mathcal{M}_{\text{last}}$ [µm] | $n_0$ | $q$ |
|---|---|---|---|---|
| PXB | $2.0 \pm 0.13$ | $5.4 \pm 0.14$ | $(-6.6 \pm 1.15) \cdot 10^5$ | $(1.9 \pm 0.06) \cdot 10^4$ |
| PXF | - | $45.0 \pm 1.23$ | - | - |
| TIB | $10.0 \pm 0.31$ | $23.0 \pm 0.37$ | $(-9.2 \pm 4.74) \cdot 10^4$ | $(7.9 \pm 0.14) \cdot 10^4$ |
| TID | $28.0 \pm 1.4$ | $47.0 \pm 1.44$ | $(-9.6 \pm 2.48) \cdot 10^5$ | $(1.1 \pm 0.07) \cdot 10^5$ |
| TOB | $6.2 \pm 0.36$ | $30.0 \pm 0.33$ | $(-1.5 \pm 0.07) \cdot 10^6$ | $(1.3 \pm 0.02) \cdot 10^5$ |
| TEC | $6.4 \pm 0.36$ | $28.0 \pm 0.27$ | $(-2.3 \pm 0.1) \cdot 10^6$ | $(1.2 \pm 0.02) \cdot 10^5$ |
| Tracker | $19.0 \pm 0.19$ | $37.0 \pm 0.22$ | $(-7.3 \pm 0.33) \cdot 10^5$ | $(9.5 \pm 0.09) \cdot 10^4$ |

only falsely assigned hits and fake tracks lead to this reduced quality (see section 5.1.3). Also multiple scattering and the nuclear interaction and decay of stable mesons like pions or Bremsstrahlung and effects due to ionisation for electrons reduce the track quality. All these effects are not accounted for in the track model, which assumes a minimally ionising particle.

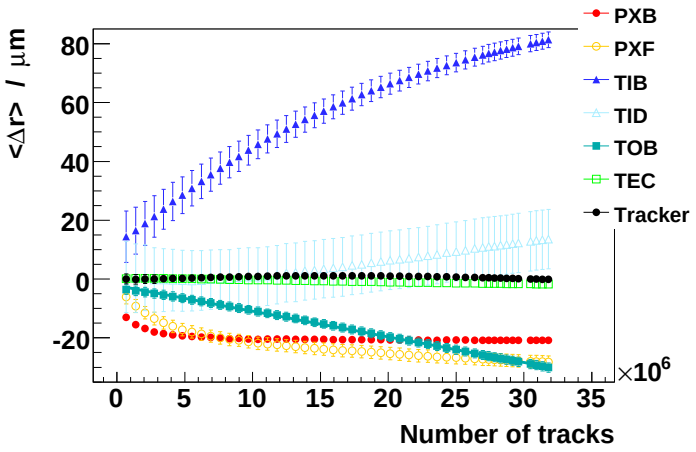


**Figure 5.4:** Bias of the module alignment along $\Delta r$ ( average of $\Delta r = r_{design} - r_{aligned} - \Delta r_{sub-detector}$) using the `TkAlMinBias` selection. Error bars denote statistical errors (see Eqn. 5.2).

In Fig. 5.4 an example for distortions produced through low track quality is depicted. Here, the average module displacement along the radial coordinate of the tracking subsystems and the full tracker (black curve) is shown. In an alignment unbiased by track quality, the residual misalignment should be centered around 0 µm in all coordinates. Especially for the tracker inner and outer barrel as well as the pixel detector this is not the case. The bias increases continuously when more tracks are added to the alignment. Interestingly, the effects compensate each other so that the overall average for the tracker is well centered. Tab. 5.2 lists the maximal bias resulting from high input statistics and compares to the bias using a sample containing the isolated muon tracks expected to be collected in the chosen S156 scenario (see section 5.1.3). The muon sample has a twofold advantage: First, the transverse momentum

spectrum of this sample is harder, as shown in Fig. 5.9a. Second, muons will traverse the tracker with less material interaction than pions and electrons found in the `TkAlMinBias` selection.

**Table 5.2:** Systematical distortions observed in the module alignment bias along $\Delta$r (average of $\Delta$r). Comparison of alignments using $\mathcal{L} = 10$ pb$^{-1}$ of the `TkAlMinBias` and `TkAlMuonIsolated` selection.

| (Sub)Detector | Minimum Bias $\lvert\langle\Delta r_{max}\rangle\rvert$ [µm] | Muon Sample $\lvert\langle\Delta r_{max}\rangle\rvert$ [µm] |
|---|---|---|
| PXB | $-21.0 \pm 0.41$ | $-8.5 \pm 0.35$ |
| PXF | $-28.0 \pm 2.12$ | $-13.0 \pm 2.21$ |
| TIB | $81.0 \pm 2.69$ | $7.0 \pm 8.94$ |
| TID | $14.0 \pm 10.1$ | $1.9 \pm 10.2$ |
| TOB | $-30.0 \pm 1.58$ | $-4.7 \pm 1.47$ |
| TEC | $-1.7 \pm 1.24$ | $0.42 \pm 1.27$ |
| Tracker | $1.1 \pm 1.09$ | $-2.4 \pm 1.12$ |

The deformation that can be seen in the minimum bias case is reduced when only muon tracks are used. As Fig. 5.5 illustrates most of the strip tracker is well centered in $\Delta r$ and additional tracks even decrease the residual misplacement of the strip tracker. In the forward pixel, the reduction of the bias is the smallest. This is explained by the general poor alignment for the pixel endcap.

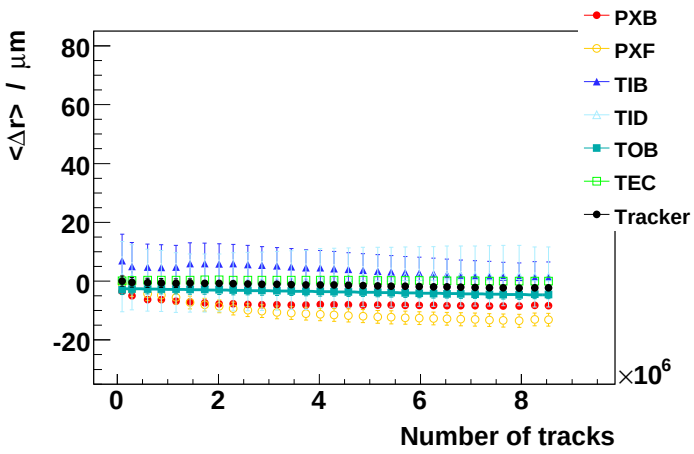


**Figure 5.5:** Bias of the module alignment along $\Delta r$ ( average of $\Delta r = r_{design} - r_{aligned} - \Delta r_{sub-detector}$) using the `TkAlMuonIsolated` selection. Error bars denote statistical errors (see Eqn. 5.2).

### The Impact on Track Parameters

In order to estimate the impact on physics measurements of the remaining misalignment, and more importantly the correlated distortion of the detector, the accuracy of the transverse momentum measurement of independent samples has been studied. As described in section 2.6 the bias and normalised resolution of this measurement are the subject of investigation.

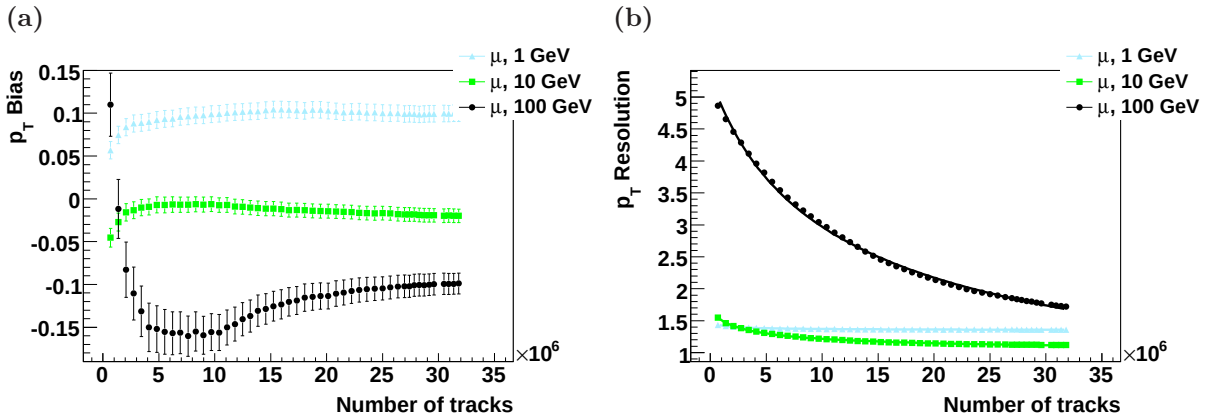


**Figure 5.6:** Evolution of (a) the bias (average of pull($p_T$)) and (b) the resolution (RMS of pull($p_T$)) for different alignments (see Eqn. 2.6). The Number of tracks used in the alignments is increased by adding more and more events of the `TkAlMinBias` selection. A fit to equation 5.1 has been made for the $p_T$ resolution. Error bars denote statistical errors (see Eqn. 5.2).

These are defined as the average and the RMS of the pull distribution pull($p_T$) = $\frac{p_{T,\mathrm{reco}} - p_{T,\mathrm{sim}}}{\sigma_{p_T}}$, respectively. Fig. 5.6 shows the evolution of bias and resolution for samples containing muon tracks simulated with $p_T$ = 1, 10, and 100 GeV. For each sample 10 000 events were simulated containing exactly two moun tracks.

For the two benchmark samples simulated at $p_T$ = 1 GeV and $p_T$ = 10 GeV, the bias introduced by the alignment is stable with respect to the addition of tracks to the sample used for alignment. This means that distortions increasing with the number of tracks used in alignment, such as the one shown in section 5.1.2, do not have a significant impact. Whereas 10 GeV muons are reconstructed with negligible bias, the 1 GeV muons are biased by about 10% of their error. The gained alignment precision along $r\Delta\varphi$ shown in section 5.7 does not improve the bias of the track fit either. Tracking algorithms are optimised for tracks with a transverse momentum above 1 GeV [28]. The observed alignment independent bias is attributed to this fact. This is different for muons simulated at $p_T$ = 100 GeV. A bias to lower transverse momenta up to a minimum of $-0.16 \pm 0.02\ \sigma_{\mathrm{stat}}$ after utilising 5 to 10 million tracks (Fig. 5.6) is observed. A part of this initial bias is compensated using more than 10 million tracks for alignment. The different behavior for the benchmark samples is to be expected, since high momentum tracks have lower radius of curvature induced by the solenoid's magnetic field. Subsequently, the relative effect of small correlated deviations of the module positions along $r\Delta\varphi$ do have a stronger impact on the $p_T$ measurement. [htp]

**Table 5.3:** Bias of the $p_T$ measurement (Average of pull($p_T$) see Eqn. 2.6) for different benchmark samples after alignment using all tracks in the `TkAlMinBias` selection. Each benchmark sample consists of 10 000 events containing two simulated muon tracks.

| Benchmark Sample | $p_T$-Bias |
|---|---|
| 1 GeV Muons | $0.1 \pm 0.01$ |
| 10 GeV Muons | $-0.02 \pm 0.01$ |
| 100 GeV Muons | $-0.099 \pm 0.01$ |

In contrast to the bias, the $p_T$-resolution does consistently improve with higher statistical power of the track selection. Again, the effect is more obvious for high momentum tracks and

**Table 5.4:** Resolution of the $p_T$ measurement (RMS of pull($p_T$) see Eqn. 2.6) for different benchmark samples after alignment using $\mathcal{L} = 10$ pb$^{-1}$ of the `TkAlMinBias` selection. Each benchmark sample consists of 10 000 events containing two simulated muon tracks. Also results of fit of equation 5.1 is shown.

| Benchmark Sample | $p_T$-Resolution | $\mathcal{M}_0$ | $n_0$ | $q$ |
|---|---|---|---|---|
| 1 GeV Muons | $1.4 \pm 0.01$ | $1.3 \pm 0.0$ | $(-3.6 \pm 3.12) \cdot 10^5$ | $96.0 \pm 13.7$ |
| 10 GeV Muons | $1.1 \pm 0.01$ | $0.96 \pm 0.0$ | $(-1.5 \pm 0.11) \cdot 10^6$ | $860.0 \pm 22.0$ |
| 100 GeV Muons | $1.7 \pm 0.01$ | $-0.71 \pm 0.02$ | $(-5.9 \pm 0.11) \cdot 10^6$ | $(1.5 \pm 0.01) \cdot 10^4$ |

as before muons simulated with $p_T = 10$ GeV can be reconstructed with the highest precision. Equation 5.1 can be fitted to all three distributions. Thus, a strong correlation between the accuracy of the transverse momentum measurement and the number of minimum bias tracks used for alignment can be concluded. This is explained by the steady improvement of the alignment along the most sensitive coordinate $r\Delta\varphi$. Tables 5.3 and 5.4 state the final values of the bias and resolution as well as the result of this fit. Note that the negative end point $\mathcal{M}_0$ of the fit shows that the resolution improves even faster than the statistical model would suggest. Therefore, even more tracks than the utilised 32 million will lead to further improvements. This could be accomplished by either looser cuts or preferably lower prescaling at HLT level.

### Investigation Towards an HLT-Level Selection

In contrast to all other selections, the number of tracks available in the `TkAlMinBias` selection is limited by the rate with which data can be recorded. From the technical maximum of 300 Hz, the rates of the physics triggers have to be subtracted which is expected to vary during the first months of LHC operation. For the CSA08 exercise, an available rate of 50 Hz for minimum bias events has been assumed and used for this study, too. The necessary rate reduction is foreseen to be done by random prescaling. This section investigates if a reduction based on physical properties measured during high level triggering, leads to a significantly better alignment precision. The advantage of a selection at HLT level is that track quality can be increased without reducing the number of tracks available to the alignment algorithm. Two samples have been used in this study:

**The Minimum Bias Sample** from the above studies represents $\mathcal{L} = 3.65 \cdot 10^{-4}$ pb$^{-1}$ of data and includes any events where tracks could be reconstructed. Given the hadronic nature of LHC interactions, these are mostly soft QCD interactions leading to a soft $p_T$ spectrum with its mean at 2.2 GeV, with about 90% below 3.2 GeV. The trigger and transverse momentum cuts lead to an overall efficiency of about 34% with respect to the unprescaled data. Multiplied by the prescale factor only one event in about $3 \cdot 10^4$ events is kept.

**The Soft Jet Sample** is a sample of soft QCD with a $\hat{p}_T > 20$ GeV [1] representing $\mathcal{L} = 0.0385$ pb$^{-1}$ of data, which is statistically prescaled to about 4% of its rate. The `TkAlMinBias` selector chooses 99.54% of the unprescaled data. The selection features a harder transverse momentum spectrum with a mean of 3.3 GeV and 90% of the tracks below 5.4 GeV.

[1] The generator level transverse momentum cut $\hat{p}_T$ applies to the transverse momentum of one of the two partons in the simulation of hard $2 \to 2$ QCD processes [27]

Comparing the alignments obtained using these samples, the effects of the two different prescaling strategies can be studied. On the one hand, the minimum bias sample represents the reduction of data rate by removing random events from the dataset. The soft jet sample on the other hand, stands for data rate reduction based on physical quantities. In this case, this is done using the generator level information and selecting jet events only.

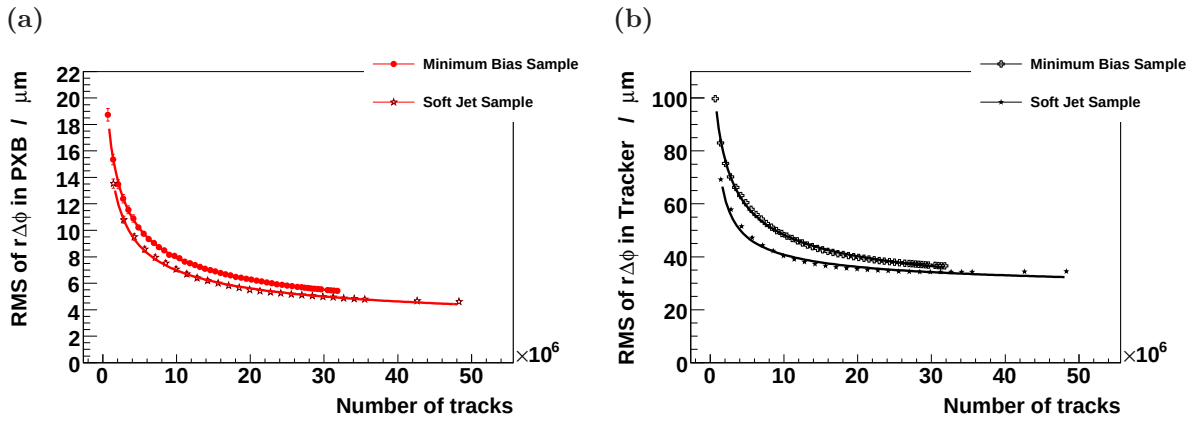


**Figure 5.7:** Evolution of the misplacement of PXB Modules (a) and all modules of the tracker (b) along the most sensitive coordinate $r\Delta\varphi$ with respect to the number of used Minimum Bias tracks (dots) and tracks from the soft jet sample (stars). Error bars denote statistical errors (see Eqn. 5.2).

To investigate the evolution of the alignment precision (see section 2.6) for the two data-sets two figures of merit are depicted. First, the RMS of the geometrical displacement for pixel barrel modules and second, the RMS of the overall displacement for all tracker modules is studied. As seen in section 5.1.1, the positions of pixel barrel modules reach the highest precision. Especially the RMS of the residual misalignment along the most sensitive coordinate $r\Delta\varphi$ is small and unbiased by systematic effects due to material interactions (Fig. 5.7a). Fig. 5.7b shows the alignment of the detector as a whole along $r\Delta\varphi$. Here one notices a slight saturation diverting from a purely statistical regression for the jet sample. A real HLT filter designed to increase alignment performance should apply quality criteria such as minimal transverse momentum (see section 5.2.1) or isolation. However this is beyond the scope of this thesis.
The alignment of the pixel barrel is summarised in Tab. 5.5. It contains the outcome of the fit to equation 5.1 and the best alignment obtained using the full data set. In this direct comparison the significantly steeper slope – a smaller quality factor $q$ – of the soft jet sample and the better result after analysing $\mathcal{L} = 10$ pb$^{-1}$ of data $\mathcal{M}_{\text{min}}$ is seen. The fit also suggests that it would take about $52.7 \cdot 10^6$ minium bias tracks, roughly the equivalent of $\mathcal{L} = 16.6$ pb$^{-1}$, to reach the jet sample precision at $\mathcal{L} = 10$ pb$^{-1}$.

Similarly Table 5.6 shows the results for the combination of all tracking modules along $r\Delta\varphi$. Here, about 2.4 pb$^{-1}$ worth of additional minimum bias tracks would be needed to reach the jet sample precision at $\mathcal{L} = 10$ pb$^{-1}$. While the slope $q$ is steeper for the alignment precision of all tracker modules than for the pixel barrel modules, the saturation mentioned above leads to a smaller difference in the precision at $\mathcal{L} = 10$ pb$^{-1}$.
In conclusion, using the soft jet sample a steeper slope and a higher precision of the module

**Table 5.5:** Parameters of the fit of equation 5.1 for the module alignment precision along $r\Delta\varphi$ for pixel barrel modules (RMS of the geometrical misplacement) compared to best precision $\mathcal{M}_{\text{min}}$. Alignments were done using tracks from the `TkAlMinBias` selection applied to a minimum bias and a soft jet sample (see text).

| Name | | Minimum Bias Sample | Soft Jet Sample |
|---|---|---|---|
| $\mathcal{M}_0$ | [µm] | $2.0 \pm 0.13$ | $2.2 \pm 0.13$ |
| $\mathcal{M}_{\text{min}}$ | [µm] | $5.4 \pm 0.14$ | $4.6 \pm 0.12$ |
| $n_0$ | | $(-6.6 \pm 1.15) \cdot 10^5$ | $(-3.8 \pm 1.82) \cdot 10^5$ |
| $q$ | | $(1.9 \pm 0.06) \cdot 10^4$ | $(1.5 \pm 0.07) \cdot 10^4$ |

level alignment is observed for both the pixel barrel modules and all tracker modules. Thus, a selection like the soft jet sample is most beneficial for early alignments. If other large selections are available it looses its advatege, as observed in the saturation of the alignment precision of the combination of all tracker modules. Additional studies to develop a HLT trigger that improves track selection for alignment on HLT level should be done.

**Table 5.6:** Parameters of the fit of equation 5.1 for the module alignment precision along $r\Delta\varphi$ (RMS of the geometrical misplacement $r\Delta\varphi$) for all tracker modules compared to best precision $\mathcal{M}_{\text{min}}$. Alignments were done using tracks from the `TkAlMinBias` selection applied to a minimum bias and a soft jet sample (see text).

| Name | | Minimum Bias Sample | Soft Jet Sample |
|---|---|---|---|
| $\mathcal{M}_0$ | [µm] | $19.0 \pm 0.19$ | $25.0 \pm 0.16$ |
| $\mathcal{M}_{\text{min}}$ | [µm] | $37.0 \pm 0.22$ | $34.0 \pm 0.21$ |
| $n_0$ | | $(-7.3 \pm 0.33) \cdot 10^5$ | $(3.0 \pm 0.36) \cdot 10^5$ |
| $q$ | | $(9.5 \pm 0.09) \cdot 10^4$ | $(4.8 \pm 0.07) \cdot 10^4$ |

### 5.1.3 The `TkAlMuonIsolated` Selection

The `TkAlMuonIsolated` selections basis is to choose tracks associated to global muons (see Tab. 3.1). Therefore, the high level trigger selection includes all high statistics muon bits. At least one of the following HLT conditions has to be met:

`HLT1MuonPrescalePt3` **and** `HLT1MuonPrescalePt5` requests at least one track reconstructed in the muon system with a $p_T > 3$ GeV and $p_T > 5$ GeV. These bits are statistically prescaled to reduce the rate of analysed events

`HLT1MuonIso` requests at least one track reconstructed in the muon system with $p_T > 11$ GeV. This track has to be separated in $\Delta R$ from measurements in the calorimetry systems (see [11] and [12] for details)

`HLT1MuonNonIso` requests at least one track reconstructed in the muon system with $p_T > 16$ GeV

In order to reject badly reconstructed low momentum tracks the `TkAlMuonIsolated` selection applies an additional transverse momentum cut of $p_T > 2$ GeV. Finally, a selected track has to be separated by a cone of $\Delta R > 0.1$ from the core of any jet reconstructed with a

transverse energy of more than 40 GeV. This isolation is applied since the rate of muons produced in the decay of charm or bottom mesons is orders of magnitude larger than the rate of muons produced in the Drell-Yan channel. For example, the cross-section for $b\bar{b}$ events is about four magnitudes larger than that of Drell-Yan (Fig. 1.1). Therefore, most muon tracks are embedded inside of jets. If the density of charged particles in the jet is large, fake hits and misalignment lead to errors during pattern recognition and track fit during the reconstruction process [13]. Fig. 5.8 shows the impact of misalignment to the fake rate in $t\bar{t}$ jet events.
Note that the fake rate can be reduced by not taking the misalignment into account during pattern recognition ("APE not used" in the Fig. 5.8). This however leads to a drastically reduced reconstruction efficiency. Since large track samples are the goal of the `TkAlMuonIsolated` selection, omitting the alignment position errors (APE) is not a feasible method.

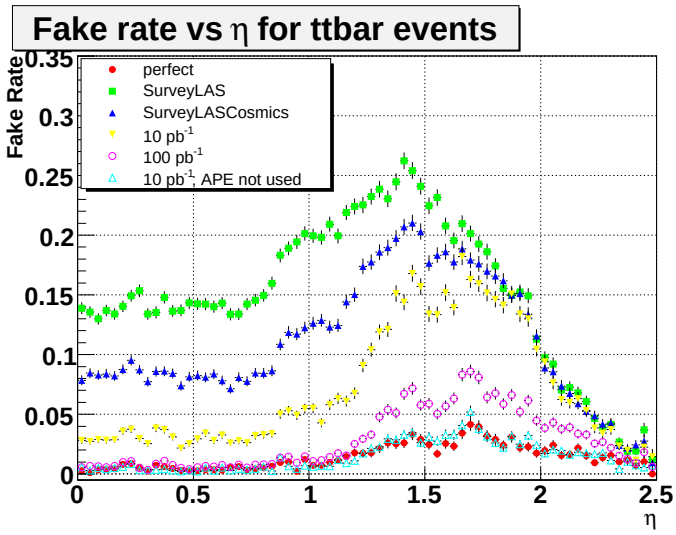


**Figure 5.8:** Observed fake rate in $t\bar{t}$ jet events for different misalignment scenarios. A track is defined as fake if there is no simulated track sharing at least 50% of its hits. The fake rate is the ratio of fake tracks to all reconstructed tracks.

Fig. 5.9a shows the transverse momentum spectrum of the `TkAlMuonIsolated` selection obtained from the CSA08 muon sample. In this sample events were rejected on generator level if they did not contain at least one simulated muon track with $p_T > 5$ GeV. Again, a tight correlation between the transverse momentum cut and number of selected tracks is anticipated. The effect of the generator level and HLT cut is seen: below a transverse momentum of 5 GeV only few tracks are found. These are reconstructed in the same event as a muon with higher transverse momentum.
In Fig. 5.9b a hit map as introduced in section 5.1.1 is depicted showing a similar distribution of hits as the `TkAlMinBias` selection.

### The Position Resolution in $r\Delta\varphi$

Similar to the study done for the `TkAlMinBias` selection, the alignment precision as function of the number of utilised tracks was studied for the `TkAlMuonIsolated` selection. Again the main figure of merit are the bias and precision of the module alignment along the most sensitive coordinate $r\Delta\varphi$. The evolution of its average and RMS is depicted in Fig. 5.10. As can be concluded from Fig. 5.10a the average $\langle r\Delta\varphi \rangle$ is well centered around zero within its error.

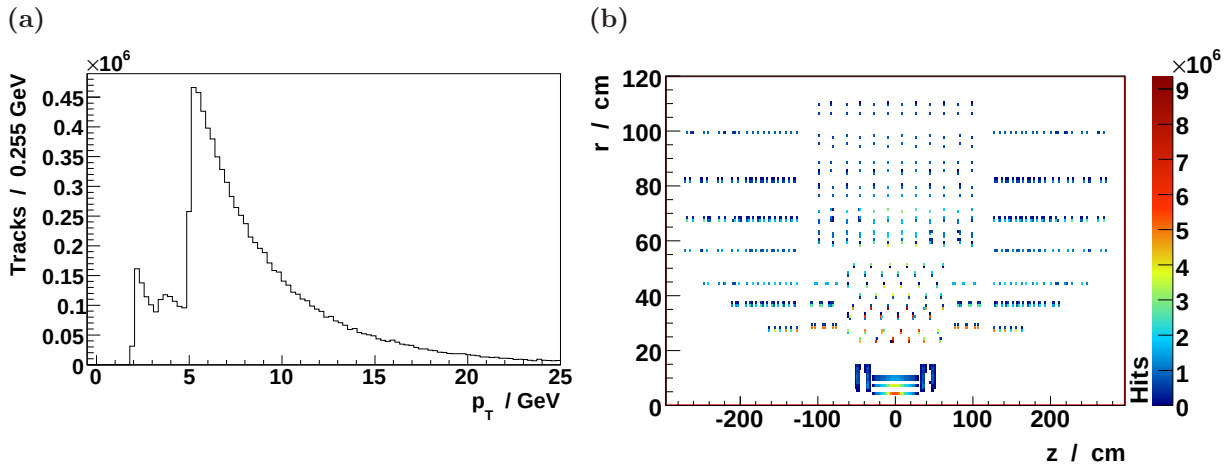


**Figure 5.9:** (a) Transverse momentum spectrum and (b) hit positions in the `TkAlMuonIsolated` selection.

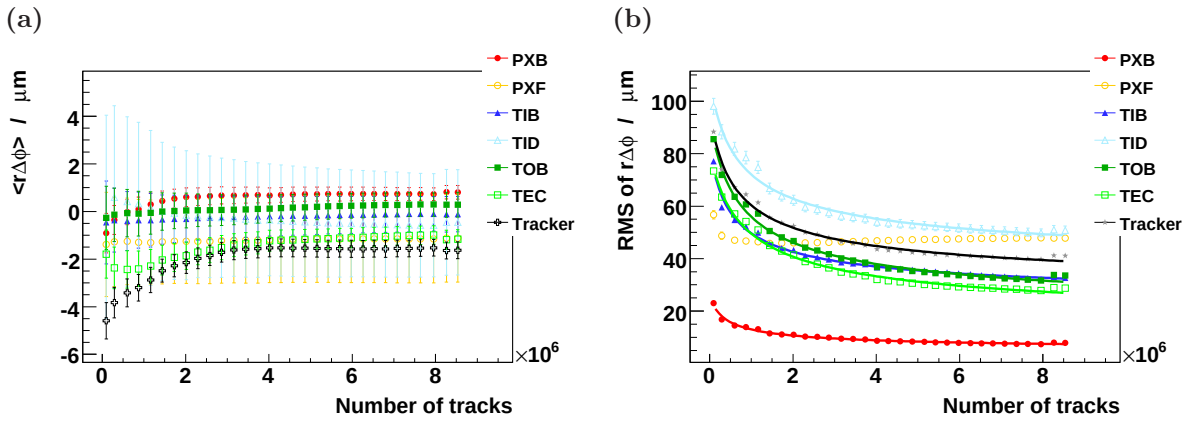


**Figure 5.10:** Statistical evolution of the module alignment bias (a) and precision (b) along the most sensitive coordinate $r\Delta\varphi$. A fit of Eqn. 5.1 is shown for the module alignment precisions for all sub-detectors excluding the pixel forward system. Error bars denote statistical errors (see Eqn. 5.2).

As shown for the TkAlMinBias selection, Eqn. 5.1 describes the evolution of the residual misalignment along $r\Delta\varphi$. The only exception to this rule, as before, is the resolution of the pixel forward alignment. Table 5.7 quotes the outcome of the alignment and compares to the precision achieved using the TkAlMinBias selection. Note that the achievable alignments using the full data sample expected at $\mathcal{L} = 10$ pb$^{-1}$ are compared, thus the minimum bias selection can utilise three times more tracks than the TkAlMuonIsolated selection.

**Table 5.7:** Module alignment precision along $r\Delta\varphi$ (RMS of the remaining geometrical misplacment) using $\mathcal{L} = 10$ pb$^{-1}$ of data for the full tracker and its subsystems. Comparision shows the TkAlMinBias selection (about $31.8 \cdot 10^6$ tracks) and the TkAlMuonIsolated selection (about $8.5 \cdot 10^6$ tracks)

| Subdetector | Minimum Bias RMS $r\Delta\varphi_{\text{last}}$ [μm] | Muon Sample RMS $r\Delta\varphi_{\text{last}}$ [μm] |
|---|---|---|
| PXB | $5.4 \pm 0.14$ | $7.3 \pm 0.19$ |
| PXF | $45.0 \pm 1.23$ | $46.0 \pm 1.25$ |
| TIB | $23.0 \pm 0.37$ | $32.0 \pm 0.51$ |
| TID | $47.0 \pm 1.44$ | $50.0 \pm 1.53$ |
| TOB | $30.0 \pm 0.33$ | $32.0 \pm 0.35$ |
| TEC | $28.0 \pm 0.27$ | $28.0 \pm 0.27$ |
| Tracker | $37.0 \pm 0.22$ | $40.0 \pm 0.24$ |

Due to the different size of both selections, the difference in the alignment resolution of the TkAlMinBias selection is consistently smaller. The direct comparison as shown for all tracker modules (Fig. 5.11 and Tab. 5.8) illustrates the effect of the higher quality of (lower $q$) of the muon tracks for alignment: The resolution improvement per used track is significantly higher. However, this is overcompensated by the abundance of tracks in the TkAlMinBias selection. Thus, the final precision seen in Table 5.7 is constantly higher for the TkAlMinBias selection. From the fit to Eqn.5.1 it is concluded, that if it were possible to increase the rate of accepted muons to choose $12.9 \cdot 10^6$ instead of $8.5 \cdot 10^6$ muons, the precision of the alignment using TkAlMinBias could be reached in terms of the overall module misalignment in $r\Delta\varphi$. Since the efficiency of muon reconstruction already is more than 98% for most of the $\eta$ range [6] this could either be done by loosening the isolation or transverse momentum cut or by improving the HLT selection. A lower transverse momentum threshold during early running is foreseen and would be beneficial to the alignment precision. Possible changes in selection thresholds are discussed in section 5.2.

**Table 5.8:** Quantitative results for the comparison of the TkAlMuonIsolated and TkAlMinBias selection with respect to alignment performance along $r\Delta\varphi$.

| Name | | Minimum Bias Sample | Muon Sample |
|---|---|---|---|
| $\mathcal{M}_0$ | [μm] | $19.0 \pm 0.19$ | $26.0 \pm 0.24$ |
| $\mathcal{M}_{\text{min}}$ | [μm] | $37.0 \pm 0.22$ | $40.0 \pm 0.24$ |
| $n_0$ | | $(-7.3 \pm 0.33) \cdot 10^5$ | $(-3.2 \pm 0.13) \cdot 10^5$ |
| $q$ | | $(9.5 \pm 0.09) \cdot 10^4$ | $(4.0 \pm 0.06) \cdot 10^4$ |

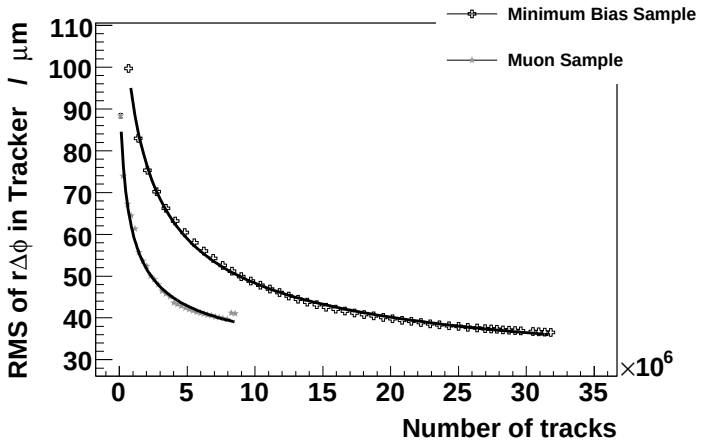


**Figure 5.11:** Direct comparison of the performance of the tracker module alignment precision along $r\Delta\varphi$ (RMS of $r\Delta\varphi$) of the `TkAlMuonIsolated` and `TkAlMinBias` selection, respectively. Error bars denote statistical errors (see Eqn. 5.2).

#### The Impact on Tracking Performance

As before, the impact of the residual misalignment has been studied using three independent benchmark samples containing 10 000 events and two muon per event. The muons have been simulated with a transverse momentum of 1, 10, and 100 GeV, respectively. Fig. 5.12a shows the evolution of the bias to the transverse momentum measurement. Fig. 5.12b shows the change of the obtained resolution. Both figures of merit are obtained from the distributions of pull$(p_T) = \frac{p_{T,\mathrm{reco}} - p_{T,\mathrm{sim}}}{\sigma_{p_T}}$ as introduced in section 2.6.2. Comparing the results to the study using the `TkAlMinBias` selection, the same features are observed: Muons simulated with $p_T = 10$ GeV are reconstructed with the highest precision. After utilising a few million tracks in alignment, neither the bias nor the resolution for the measurement of $p_T = 1$ GeV muons improves much, because tracking algorithms are not optimised for these tracks. Again, the largest improvements in $p_T$ measurement resolution are achieved for muons simulated at $p_T = 100$ GeV. This is explained by the greater sensitivity of such tracks to the residual misalignment along $r\Delta\varphi$. There is a minimum in the bias of the transverse momentum measurement for the $p_T = 100$ GeV muons at 5 million tracks utilised in the alignment process. In contrast to the `TkAlMinBias` selection there are not enough tracks available to observe a significant reduction of the bias after 10 million utilised tracks.

### 5.1.4 Conclusion

- Even after using 10 million tracks improvement of the alignment is observed.
- Higher alignment precision increases the resolution of high $p_T$ tracks muon tracks.
- The reduced quality of the `TkAlMinBias` selection leads to a correlated distortion of the module positions by the alignment procedure (section 5.1.2). Nevertheless, the higher quality of the `TkAlMuonIsolated` selection lacks statistical power. Thus, its overall performance falls short of the larger `TkAlMinBias` selection.

## 5.2 The Optimisation of Track Selection Criteria

The conclusion of the above section is that the number of tracks available for alignment is highly important to early alignment precision. This is supported by the naïve assumption that

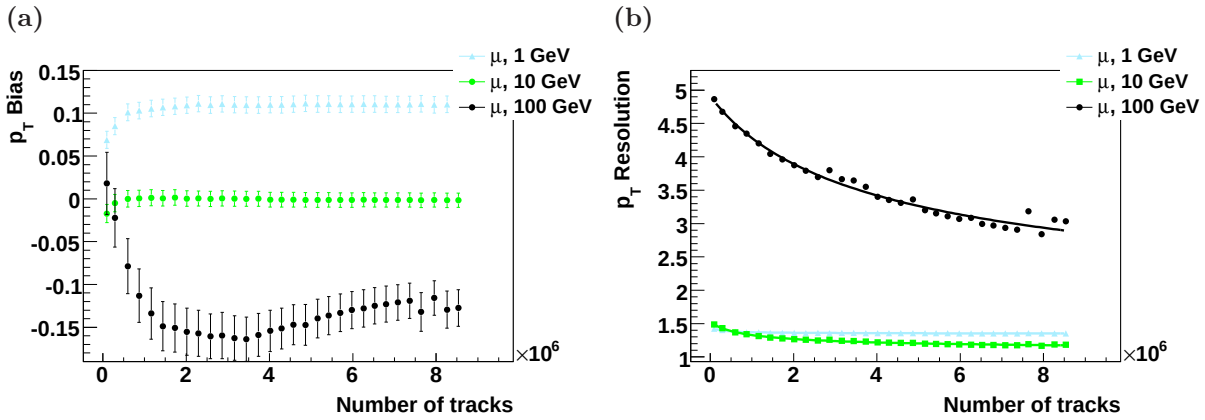


**Figure 5.12:** Evolution of (a) the bias (average of pull($p_T$) see Eqn. 2.6) and (b) the resolution (RMS of pull($p_T$) see Eqn. 2.6) for different alignments. The Number of tracks used in the alignments is increased by adding more and more events of the `TkAlMuonIsolated` selection. A fit to Eqn. 5.1 has been made for the distribution of the $p_T$ resolution. Error bars denote statistical errors (see Eqn. 5.2).

every well measured track adds information and thus helps to solve the alignment problem. Tight quality cuts ensure well measured tracks but decrease the number of tracks utilised in alignment. Thus, quality criteria have to be chosen to strike a balance between track quality and number of tracks in the selection. To evaluate the impact of changing the selection criteria, the ALCARECO selection cuts were both tightened and loosened before performing full tracker alignments. Basis for the cuts were samples containing $10 \cdot 10^6$ events of the minimum bias ($\mathcal{L} = 3.6$ pb$^{-1}$) and the muon enriched sample ($\mathcal{L} = 8.9$ pb$^{-1}$).

### 5.2.1 The Transverse Momentum Cut

The transverse momentum of the tracks used for alignment is expected to impact its precision due to multiple scattering. For low momentum tracks multiple scattering is accounted for by large uncertainties for the hit position measurements. Also these uncertainties lead to increased inclusion of fake hits in the track fit, which in turn reduce track quality. These effects are reduced for high momentum tracks [25], thus a transverse momentum cut might improve track quality for alignment. However, the $p_T$ distributions of both the `TkAlMinBias` (Fig. 5.2a) and the `TkAlMuonIsolated` (Fig. 5.9a) selections show that selection size will be greatly reduced by $p_T$-cuts.

#### The `TkAlMinBias` Selection

Fig. 5.13 shows the impact of transverse momentum cuts on alignment quality, selecting from the $\mathcal{L} = 10$ pb$^{-1}$ scenario events. While the average of the residual misalignment along the most sensitive coordinate $r\Delta\varphi$ is not significantly biased with respect to their errors for the tracker sub-detectors at thresholds below 7 GeV, the bias accumulates and introduces a significant deviation from a centered distribution of the tracker as a whole. This global rotation is harmless since it can be canceled by a redefinition of the coordinate system. On the right hand side of Fig. 5.13, the alignment precision for the same coordinate is plotted with respect to the applied cut. With lower $p_T$ thresholds a higher precision and less bias is observed.

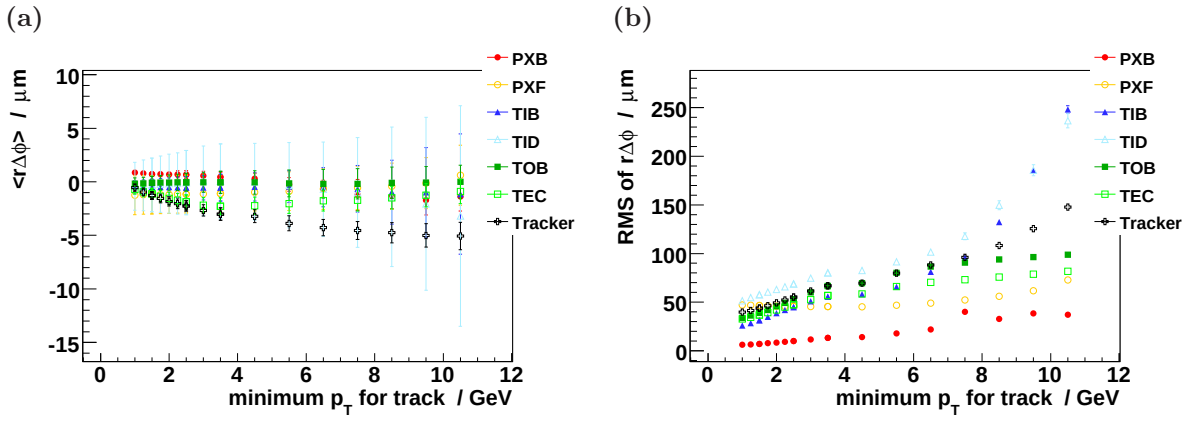


**Figure 5.13:** Bias (average of $r\Delta\varphi$) (a) and precision (RMS of $r\Delta\varphi$) (b) of the module alignment along $r\Delta\varphi$ for different minimal transverse momentum cuts on $10 \cdot 10^6$ events of the minimum bias sample. Cuts in the range of $p_T > 0.5$ and 10.5 GeV in steps of 0.5 GeV, additional data points at $p_T > 1.25$, 1.75, and 2.25 GeV. Error bars denote statistical errors (see Eqn. 5.2).

This demonstrates that the reduction of sample size supersedes the gain in track quality. Additional insight can be gained by investigating the radial distortion of the detector discovered in section 5.1.2. Fig. 5.14b illustrates that the alignment precision along $\Delta r$ is mostly independent of the transverse momentum cut for all subdetectors but the tracker inner barrel. In Fig. 5.14a applying transverse momentum cuts leads to well centered residual misalignment along $\Delta r$ which could be attributed to higher track quality. However, it has already been shown that this distortion increases with larger track samples. The disentanglement of those two effects is studied in the next section.

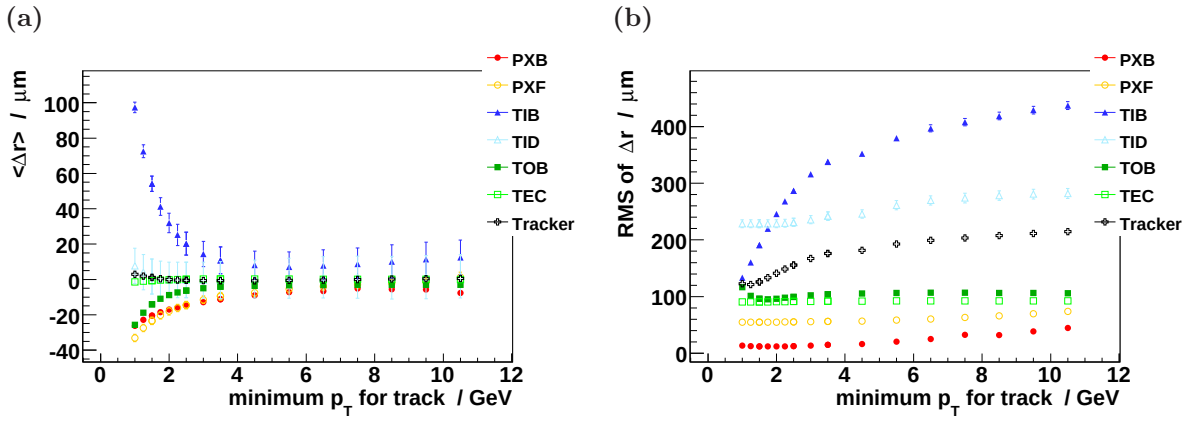


**Figure 5.14:** Bias of the module alignment along $\Delta r$ (average of $\Delta r$) for different minimal transverse momentum on $10 \cdot 10^6$ events of the minimum bias sample. Cuts in the range of $p_T > 0.5$ and 10.5 GeV in steps of 0.5 GeV, additional data points at $p_T > 1.25$, 1.75, and 2.25 GeV. Error bars denote statistical errors (see Eqn. 5.2).

### Disentangling Influences to the Distortions along $\Delta r$

In order to find out if the reduced bias in Fig. 5.14a is solely due to the reduction of the number of tracks used for alignment or due to improved track quality by transverse momentum cuts, the number of tracks used for alignment was reduced by $p_T$-cuts instead of random chance as before in section 5.1.2. The cuts applied range are the same used in section 5.2.1. The comparison is shown in Fig. 5.15. Although the alignments obtained using the sample restricted by $p_T$ cuts do improve marginally, the overall correlated distortion does not change. In both cases a linear dependence of the Bias of the tracker outer barrel module alignment with respect to the number of used tracks is visible. A straight line fit produces slopes of $(-8.7 \pm 0.24) \cdot 10^{-7}$ µm track$^{-1}$ and $(-7.5 \pm 0.49) \cdot 10^{-7}$ µm track$^{-1}$ for the randomly and the systematically reduced selection, respectively. The observed difference is small and within the statistical errors not very significant.
In conclusion, the effects of using higher momentum tracks and using muon tracks observed in the last section has been disentangled. The improvements seen using the muon sample can be largely attributed to the properties of muons for the alignment. Thus, muon data samples should be used whenever their size allows successful alignment.

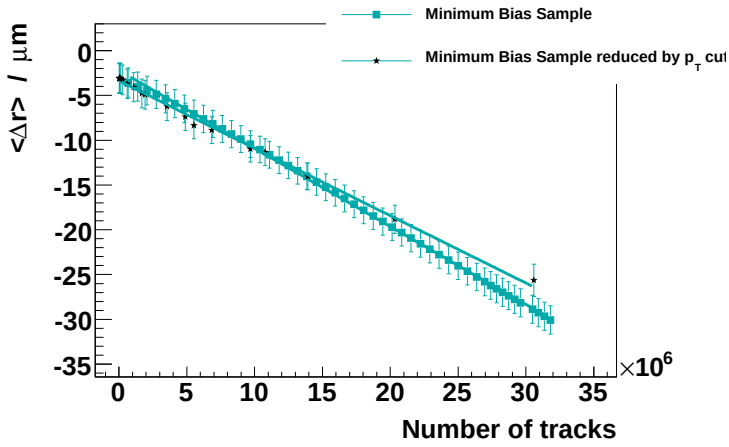


**Figure 5.15:** Comparison of the bias of the tracker outer barrel module alignment along $\Delta r$ using randomly reduced statistics (blue squares) and statistics reduced by transverse momentum cuts (black stars). Basis for the reduction by transverse momentum cuts were on $10 \cdot 10^6$ events of the minimum bias sample. A linear fit has been applied to both distributions. Error bars denote statistical errors (see Eqn. 5.2).

### Improvement Independent of the Selection Size

It has been shown that the gain in track quality does not outweigh the loss in sample size. As discussed above, using a dedicated HLT filter, track quality could be improved without decreasing the number of tracks available for alignment. In this section the impact of transverse momentum cuts irrespective of the loss in statistics is studied. To this end, the fit of Eqn. 5.1 obtained in section 5.1.1 is used. For a given number of tracks used in alignment it yields a projection $\mathcal{M}^{\text{fit}}_{\text{precision}}$ of the obtained alignment precision along $r\Delta\varphi$. The improvement $i_{\text{precision}}$ of the alignment precision is defined as:

$$i_{\text{precision}} = \mathcal{M}^{\text{fit}}_{\text{precision}}(n|_{p_T^{\text{cut}}}) - \mathcal{M}_{\text{precision}}|_{p_T^{\text{cut}}}$$

where $\mathcal{M}_{\text{precision}}|_{p_T^{\text{cut}}}$ denotes the value of the metric obtained applying the threshold $p_T^{\text{cut}}$. Further $n|_{p_T^{\text{cut}}}$ represents the number of tracks reconstructed with a transverse momentum above $p_T^{\text{cut}}$. It follows that $\mathcal{M}^{\text{fit}}_{\text{precision}}(n|_{p_T^{\text{cut}}})$ is the projected alignment precision using $n|_{p_T^{\text{cut}}}$ tracks of the standard selection. Smaller values of $\mathcal{M}^{\text{fit}}_{\text{precision}}$ and $\mathcal{M}_{\text{precision}}|_{p_T^{\text{cut}}}$ are interpreted as better alignment precision, because they are defined by the RMS of the $r\Delta\varphi$ distribution. Subsequently, $\mathcal{M}^{\text{fit}}_{\text{precision}} > \mathcal{M}|_{p_T^{\text{cut}}}$ shows that the transverse momentum cut allowed for a better alignment precision if the loss in statistics in neglected.
Similarly, the improvement of the resolution of the transverse momentum measurement $i_{\text{resolution}}$ can be defined.

$$i_{\text{pT resolution}} = \mathcal{M}^{\text{fit}}_{\text{pT resolution}}(n|_{p_T^{\text{cut}}}) - \mathcal{M}_{\text{pT resolution}}|_{p_T^{\text{cut}}}$$

The fit to the statistical evolution of the $p_T$ resolution $\mathcal{M}^{\text{fit}}_{\text{resolution}}$ is used to predict the resolution using $n|_{p_T^{\text{cut}}}$ tracks for alignment. Again smaller values of the resolution represent better alignments and positive improvements $i_{\text{resolution}}$ show that the transverse momentum cut did improve the track quality for alignment.

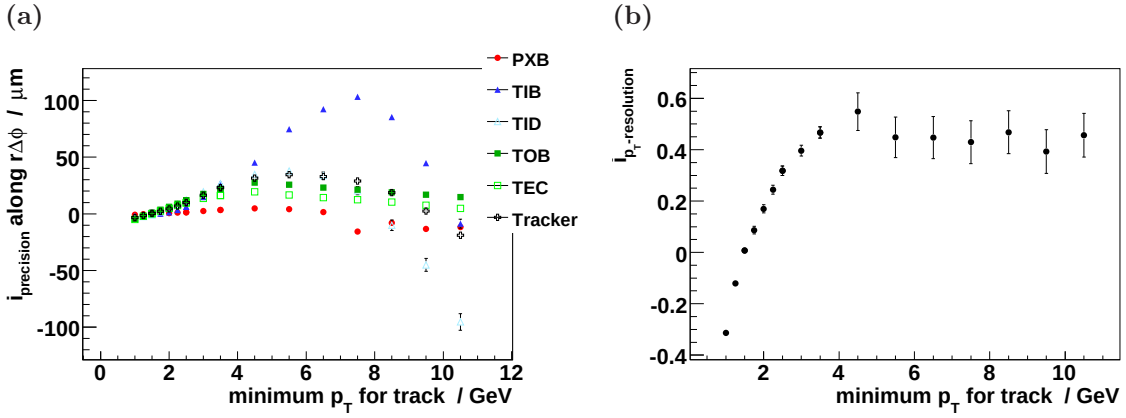


**Figure 5.16:** Improvements $i_{\text{precision}}$ and $i_{\text{resolution}}$ (see text) obtained using transverse momentum cuts for the `TkAlMinBias` selection. Events for alignment were selected from $10 \cdot 10^6$ events of the minimum bias sample. Benchmark sample used for (b) consists of 10 000 events containing two muon tracks simulated at $p_T = 100$ GeV. Error bars denote statistical errors calculated by error propagation.

Fig. 5.16a introduces the improvements determined by the above procedure for the subdetectors and the whole tracking system, respectively. Note that the forward pixels are excluded from this study since no significant improvement could be observed changing both the number of used tracks and the $p_T$ threshold. There are two features visible in the distribution of the improvements: First, the improvement rises with for higher thresholds. This proofs that the track quality is indeed increased by $p_T$ cuts.
Second, this rise meets a maximum between $p_T^{\text{cut}} = 4.5$ GeV and $p_T^{\text{cut}} = 8.0$ GeV depending on the sub-detector in question. For these, only about 500 to 50 thousand tracks pass the high cuts. The decreases the quality of the alignment since not all degrees of freedom can be constrained by the track selection. This effect is not accounted for in equation 5.1 and leads to better expected module alignment precisions. Due to the high occupancy of the tracker inner barrel already observed in Fig. 5.2b, the turning point for the improvement of this sub-detector is reached at the highest threshold, in turn leading to the largest improvements. The resolution of the transverse momentum measurement similarly improves for track selections based on higher thresholds as observed in Fig. 5.16b. Again, starting at thresholds of

about 4.5 GeV no further improvement is observed, because systematic effects due to missing constraints lead to worse alignments than predicted by the fit.
In conclusion it has been shown that track quality for alignment improves when applying transverse momentum cuts. As seen earlier, this effect is however outweighed by the need of a large track sample for early alignment. Thus, transverse momentum cuts are useful if more tracks are available. This is the case for a HLT level selection or long term alignment where $\mathcal{M}_0$ of equation 5.1 dominates the alignment precision.

#### The `TkAlMuonIsolated` Selection

The alignment performance has been studied as a function of the minimal transverse momentum threshold similar to the study of the minimum bias case. Since the sample was simulated with a generator level cut off at $p_T = 5$ GeV, this value was the starting point for the study. Additionally, the effect of the secondary tracks with a lower $p_T$ (Fig. 5.9a) was studied by a cut at 2 GeV. The outcome of this alignment should not be mistaken for an alignment using all tracks with $p_T > 2$ GeV which could utilise significantly more tracks.
Fig. 5.17 depicts the outcome of those alignments in terms of the residual misalignment along the most sensitive coordinate.

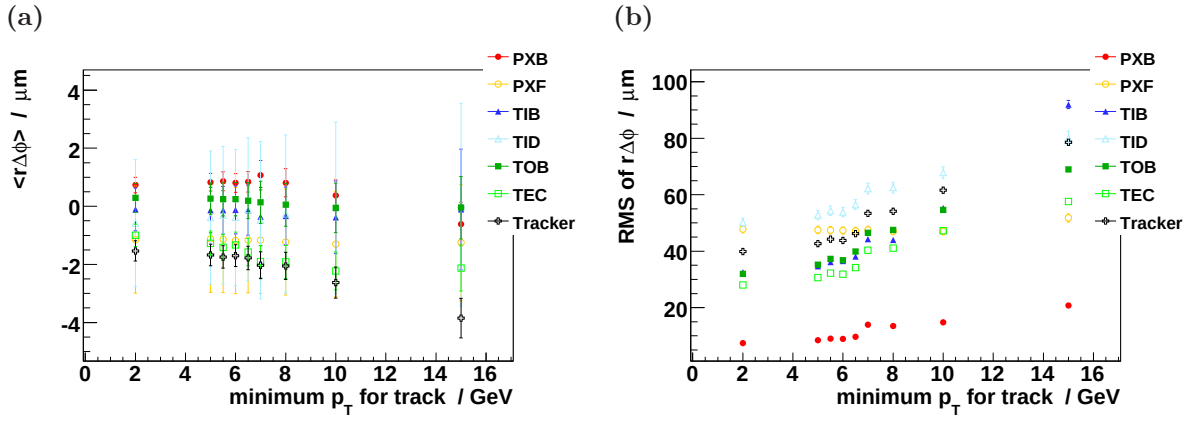


**Figure 5.17:** Bias (average of $r\Delta\varphi$) (a) and precision (RMS of $r\Delta\varphi$) (b) of the module alignment along $r\Delta\varphi$ for different minimal transverse momenta in the `TkAlMuonIsolated` selection. Basis for this selection were $10 \cdot 10^6$ events of the muon sample. Error bars denote statistical errors (see Eqn. 5.2).

As before, the alignment does not gain from the higher transverse momentum cuts. The reduced number of available tracks produces a less-centered residual misalignment for high cut-offs and reduced precision in all subdetectors but the forward pixel modules. Even the low $p_T$ muon tracks coming from events with two or more muons do improve the precision of the alignment as seen in Fig. 5.17b.
In conclusion for the `TkAlMuonIsolated` selection, the best alignment results could be obtained applying the lowest restrictions on the transverse track momentum. Even if distortions might be introduced by badly measured low momentum tracks, their impact on alignment precision does not justify the reduction sample size by transverse momentum cuts.

### 5.2.2 The Minimum Number of Hits Criterion

Besides the transverse momentum, the number of hit measurements included in the fit for a track is used in the `TkAlMinBias` selection. This sections investigates the impact of this cut to

the track quality for alignment using the `TkAlMinBias` selection. Fig. 5.18 shows the number of hits on a track with respect to its pseudo-rapidity. The bulk of the tracks has more than 13 hits and is, when parametrised by a helix, well over-determined. The default of eight hits demands, that the particle at least traverses beyond the first stereo layer of the tracker inner barrel. Finally, for high $\eta$, just barely at the geometrical coverage of the inner tracker, tracks are reconstructed mainly with 5 hits and below. To study the possible benefits of those tracks the standard threshold of a minimum of 8 hits was changed to 0, 2, 5, 10, and even 13.

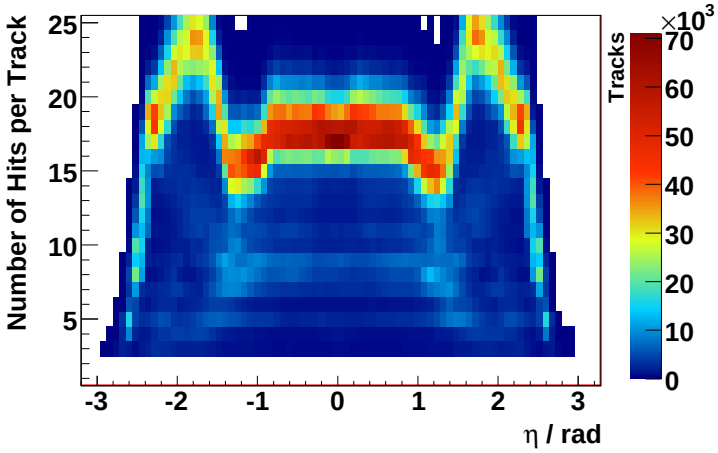


**Figure 5.18:** Number of hits on a track in the `TkAlMinBias` selection versus the pseudo-rapidity of the same.

Fig. 5.19 shows the impact of these selections, which is negligible. The slight degradation of the resolution of the transverse momentum measurement can be fully attributed to the reduction in sample size due to the cut. Notably, the poor alignment of the forward pixel is not improved by lower threshold on the number of hits per track, even though Fig. 5.18 shows that additional tracks are gained mainly in high $\eta$ ranges.
Eminently tracks reconstructed using less than 13 hits do not have a significant impact on the alignment precision.

### 5.2.3 The Track Isolation Criterion

At the LHC muons will primarily be produced in soft QCD interactions combined with many other charged particles produced in the hadronisation process. To disentangle the hits introduced by those particles from the hits by muons is a challenging task for the tracking algorithms if the hits are concentrated in a small angular region. To reduce the negative impact of wrongly reconstructed tracks (fakes) and wrongly associated hits in these regions tracks can be omitted if there are other tracks reconstructed in a similar direction.

In this section the isolation of tracks to each other is studied for the `TkAlMuonIsolated` selection. Fig. 5.20 shows the distance of one track to the next. This is determined by the minimum of $\Delta R = \sqrt{\Delta\eta^2 + \Delta\varphi^2}$ for the track with respect to all other tracks in the event. For distances larger than $\Delta R \approx 0.1$ rad, the number of tracks decreases as expected since muons are produced in QCD-jets. On the other had, during tracking a requirement is introduced to reduce the shared hits of two tracks [29]. If the tracking algorithm finds two tracks sharing more than 50% of their hits, only the one reconstructed with the lower $\chi^2$ in the track

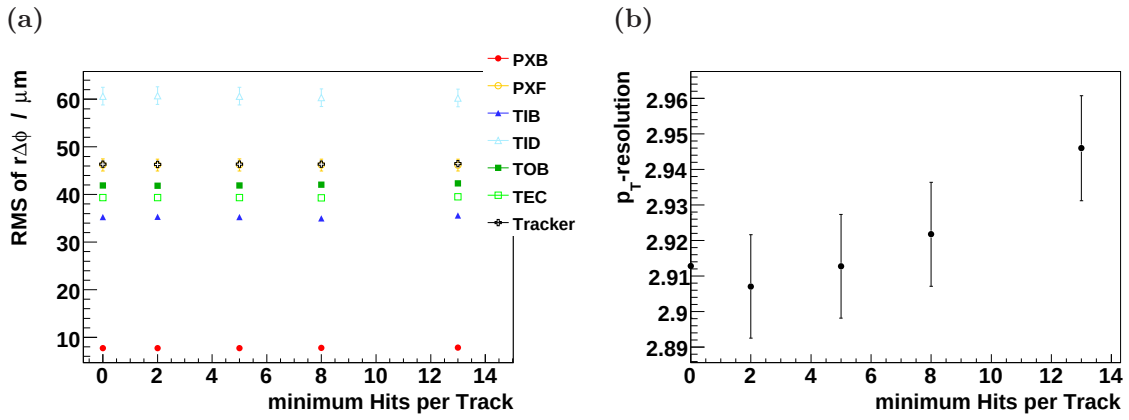


**Figure 5.19:** Precision of the module alignment (RMS of the residual misalignment along $r\Delta\varphi$) (a) and impact on transverse momentum resolution (RMS of pull($p_T$)) (b) for different minimal hit thresholds. Events for alignment were selected from $10 \cdot 10^6$ events of the minimum bias sample. Benchmark sample used in (b) consists of 10 000 events containing two muon tracks simulated at 100 GeV. Error bars denote statistical errors (see Eqn. 5.2).

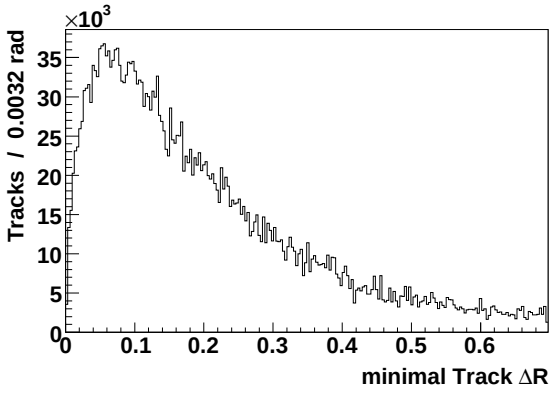


**Figure 5.20:** Distance in terms of $\Delta R = \sqrt{\Delta\eta^2 + \Delta\varphi^2}$ of one track to the nearest other track in the `TkAlMuonIsolated` selection.

fit is kept.
For alignment, however, a tighter requirement could be beneficial, since in principle any hit wrongly associated to a used track introduces a bias. To make sure a track is isolated, a criterion is introduced that ensures a minimal distance of the track used in alignment to the next in $\Delta R$. To verify the benefit of this isolation criterion different thresholds have been used for full tracker alignments.

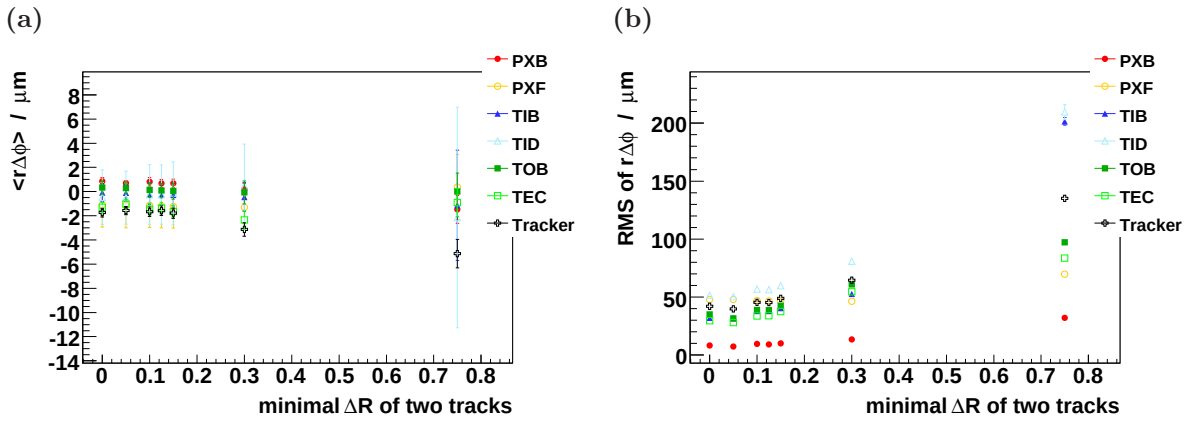


**Figure 5.21:** Bias (average of $r\Delta\varphi$) (a) and precision (RMS of $r\Delta\varphi$) (b) of the module alignment along $r\Delta\varphi$ for different minimal track distance thresholds in addition to the `TkAlMuonIsolated` selection. Basis for this selection were $10 \cdot 10^6$ events of the muon sample. Error bars denote statistical errors (see Eqn. 5.2).

Fig. 5.21 shows the impact of this cut on the residual misalignment along the most sensitive coordinate. As seen already in the study of transverse momentum selections the reduction of sample size due to the cuts surpasses the benefits from the isolation and high cuts introduce a bias. Further studies correcting for the different sample sizes – similar to section 5.2.1 – have shown that no significant improvement is gained by the track isolation criterion.

## 5.3 Conclusions

- Transverse momentum cuts do neither improve the alignment precision of the `TkAlMinBias` nor the `TkAlMuonIsolated` selection. The reduction of the number of tracks available for alignment supersedes any beneficial effect.

- For the `TkAlMinBias` selection a significant improvement of alignment precision is observed when compared to an alignment using the same number of tracks but a smaller transverse momentum threshold. For this selection a dedicated HLT trigger bit could impose transverse momentum thresholds instead of random prescaling. In that case a transverse momentum cut is proven to be beneficial.

- The observed reduction of the correlated distortion along $\Delta r$ for higher transverse momentum cuts is mainly induced by the reduced number of tracks not by improved track quality.

- Reducing the minimal number of hits of tracks used for alignment has proven to be without significant effect on alignment precision.

- Imposing an isolation criterion based on the angular distance of reconstructed tracks has been shown not to improve the alignment, either. Tracks are already well seperated due to reconstruction.
- The number of tracks handed to the alignment algorithm is paramount to alignment precision.

# 6. Performance of Mixed Track Selections

The expected rate of very high quality events like Drell-Yan $Z \rightarrow \mu^+\mu^-$ at the LHC is too low to achieve a full tracker alignment in the $\mathcal{L} = 10$ pb$^{-1}$ scenario with these samples alone. Therefore, it is proposed to enhance the alignment quality by adding tracks from those high quality data sets to the alignment procedure. The idea is to constrain $\chi^2$ invariant modes (see section 2.4) of the `TkAlMinBias` or `TkAlMuonIsolated` selection by tracks that are on the one hand very well measured, and on the other hand introduce additional information through mass and vertex constraints as described in section 2.5.
A second ansatz to constrain $\chi^2$ invariant modes is to use non-collision tracks like cosmic muons or beam halo tracks travelling parallel to the beam line. The latter are produced in beam gas reactions or during the collimation of the beams as they reach the CMS cavern. Both offer a radically different event topology compared to tracks stemming from collision events.
In this chapter studies are performed to estimate the value of these additional sources of tracks in combination with the `TkAlMinBias` selection, which provided the best alignment result for the $\mathcal{L} = 10$ pb$^{-1}$ scenario as shown in chapter 5. Since the samples under investigation are very small compared to the `TkAlMinBias` selection, any significant improvement in the alignment precision is not due to higher statistical power of the combined sample, but rather an effect of the special sample properties.

## 6.1 The Use of $Z \rightarrow \mu^+\mu^-$ Events

As described in chapter 4 the $Z \rightarrow \mu^+\mu^-$ decay obtained through Drell-Yan events is the "golden channel" for long term alignment. This section studies the impact of these events for the start-up scenario introduced in section 2.1. In the alignments the $32 \cdot 10^6$ tracks of the `TkAlMinBias` selection were combined with 9000 muon pairs from a $Z \rightarrow \mu^+\mu^-$ signal sample.
Fig. 6.1a depicts the residual misalignment of all tracker modules for three different cases varying the used alignment method and initial misalignment:

**"Misaligned, mass & vertex constrained"** uses the start-up misalignment and miscallibration scenario and tries to improve alignment precision by fitting the whole decay

instead of single tracks (mass and vertex constraint) as described in section 2.5. The decay is parametrized by the mass, the vertex position, two angles between the emerging muons in the Z rest frame and the initial momentum of the Z.

**"Misaligned, simple trackfit"** again uses the start up misalignment, but applies the standard helix track model for the two mouns.

**"Ideal, mass & vertex constrained"** uses the ideally aligned detector as a starting point and applies the mass and vertex constraint.

The RMS of the residual misalignment along $r\Delta\varphi$ of $(35.8 \pm 0.22)$ µm using the simple track fit is smaller than the RMS of $(41.1 \pm 0.25)$ µm obtained if the mass and vertex constraint is used. If no initial misalignment is applied, a similar result as in the unconstrained case is obtained: The RMS is $(36.5 \pm 0.22)$ µm. Note that even if no initial misalignment is applied this figure of merit is not expected to be zero. Due to material effects and detector resolution the track model does not necessarily fit the simulated track. Additionally deformations along weakly defined modes and the linearisation done in the MillePede algorithm lead to further degradation of alignment quality. Subsequently, even if no initial misalignment is applied the quality of the track selection leads to residual misalignment. Here, this quality evidently is not improved by the mass and vertex constraint.

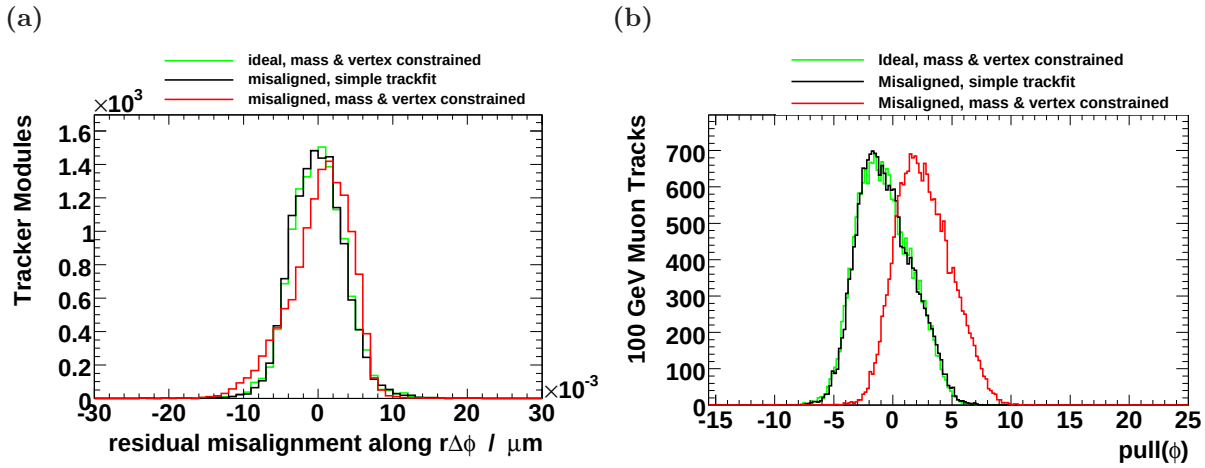


**Figure 6.1:** Residual misalignment along $r\Delta\varphi$ (a) and relative measurement of the track parameter $\varphi$ for different alignment methods and initial misalignment

Moreover, applying the mass and vertex constraint leads to an increased bias of the average of the distribution, if the $\mathcal{L} = 10$ pb$^{-1}$ misalignment scenario is used. It increases from $\langle r\Delta\varphi \rangle = 0.07 \pm 0.32$ µm starting from the ideal geometry and applying the mass and vertex constraint and $-0.29 \pm 0.31$ µm strating from the $\mathcal{L} = 10$ pb$^{-1}$ misalignment scenario without applying the mass and vertex constraint to $2.2 \pm 0.36$ µm starting from the $\mathcal{L} = 10$ pb$^{-1}$ scenario and applying the mass and vertex constraint. Also the distribution is not symmetric with respect to its mean, hinting towards a correlated distortion of the tracker.
To study the effect of these deformations, ten thousand independent events containing two muons with a simulated transverse momentum of 100 GeV were used. Fig. 6.1b and Fig. 6.2a show the resulting mismeasurements of the track parameters. Introduced in section 2.6.2 the

resulting relative mismeasurement of the $\varphi$-parameter is defined as $\text{pull}(\varphi) = \frac{\varphi_{\text{reco}} - \varphi_{\text{sim}}}{\sigma_\varphi}$. If the mean of these distribution significantly differs from zero the measurement of the parameter is systematically biased, whereas the RMS of the distribution indicates the resolution of the measurement in terms of its statistical error. The bias introduced by the mass and vertex constraint is significant for both parameters if the $\mathcal{L} = 10\ \text{pb}^{-1}$ misalignment scenario is used. The double peak observed for the relative mismeasurement of the transverse momentum is explained by the bias of the mean in Fig. 6.2b: The relative mismeasurement of the charge divided by the momentum shows only a single maximum indicating that the observed split is due to a systematic mismeasurement dependant on the particles charge. This is a sign for a $\chi^2$-invariant mode of selections containing helix tracks: The layers of the detector are systematically rotated along the beam axis. If the amplitude of this distortion increases with the radial position the measured transverse momentum is changed, but not the $\chi^2$ of the track fit. This also explains the mismeasurement of the azimuthal track direction shown in Fig. 6.1b. The fact that this is only observed for alignments starting from the misaligned geometry suggests that the alignment algorithm finds a local minimum of the $\chi^2$ function introduced by the combination of misalignment and the mass and vertex constraint.

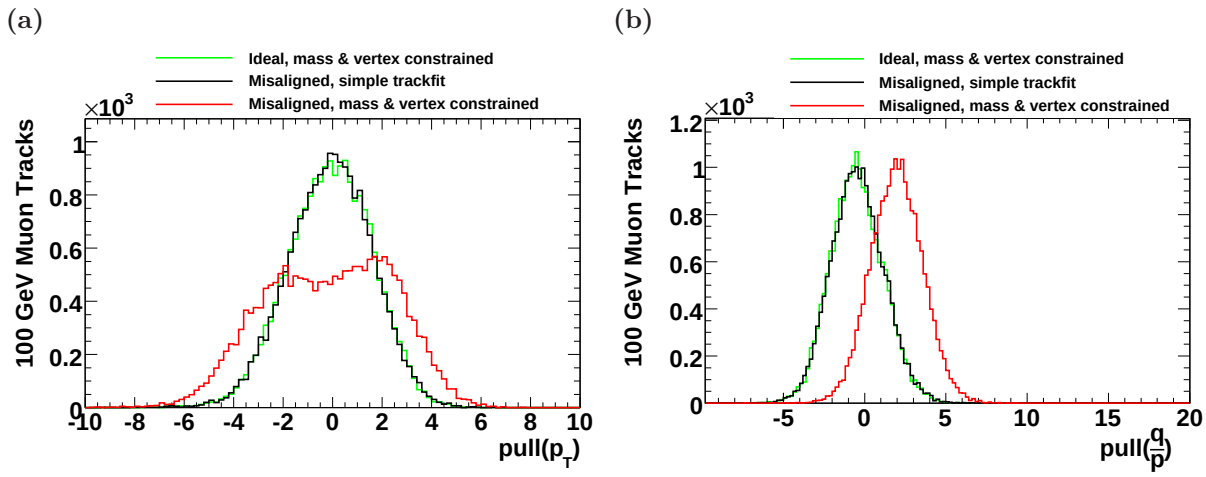


**Figure 6.2:** Relative mismeasurement of the transverse momentum $\text{pull}(p_t) = \frac{p_{T,\text{reco}} - p_{T,\text{sim}}}{\sigma_{p_T}}$ (a) and charge dived by the momentum $\text{pull}(\frac{q}{p}) = \frac{\left(\frac{q}{p}\right)_{\text{reco}} - \left(\frac{q}{p}\right)_{\text{sim}}}{\sigma_{\frac{q}{p}}}$ (b) for different alignment strategies and initial misalignments. The bench mark sample consists of 10 000 events containing two muons simulated at $p_T = 100$ GeV.

### 6.1.1 Further Investigations

To investigate this surprisingly bad performance, the events of an independent $Z \to \mu^+\mu^-$ sample have been reconstructed using the alignment constants obtained with and without applying the mass and vertex constraint. The transverse momentum resolution of the muon final states does not show the double peak observed in the sample containing $p_T = 100$ GeV muons (Fig. 6.3b).
Similarly, in Fig. 6.3a no significant impact on the invariant mass measurement is observed for the events used in alignment. Fitting a simple Breit-Wigner function to both distributions yields compatible Z-resonance masses and widths. This proofs that if there is a bias introduced by the mass and vertex constraint it is smaller than the effects of the detector resolution and

the assumption of a Breit-Wigner distribution. Here, no negative effect of the mass and vertex constraint is observed. Finally, the average normalised $\chi^2$ of the track fits improves from $1.35 \pm 0.02$ for the unbiased constants to $1.106 \pm 0.004$ for the biased constants. This confirms that the introduced deformation is unconstrained by the used samples. In conclusion the observed deformation is not due to a simple software bug that introduces a bias for all measurements.

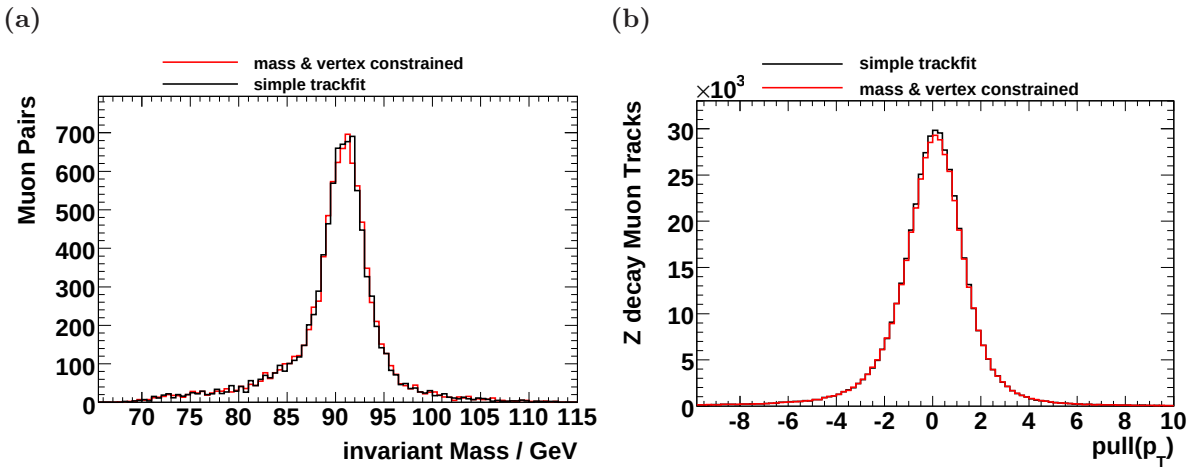


**Figure 6.3:** Comparison for the distribution of the invariant mass for muon track pairs in the used $Z \rightarrow \mu^+\mu^-$ sample (a) and for the transverse momentum mismeasurements of the same muon tracks (b).

As Fig. 6.4a illustrates there is indeed a correlation observed between the misalignment along $r\Delta\varphi$ and the radial position of the measuring module. Again the two approaches "Misaligned, simple trackfit" and "Ideal, mass & vertex constrained" as defined above produce similar results, whereas the combination of misaligned initial geometry and mass and vertex constraint introduces a significant bias. The inner parts of the detector are rotated in one direction, while the outer parts are rotated in the other. Fig. 6.4b sketches this deformation and its impact on helix tracks. This simplified model illustrates how the found deformation can introduce a bias to the measured track direction as well as the transverse momentum.

## 6.2 The Use of $\Upsilon \rightarrow \mu^+\mu^-$ Events

For the $\mathcal{L} = 10$ pb$^{-1}$ scenario 58500 events were chosen by the `TkAlUpsilonMuMu` selection. These tracks were used in addition to the 32 million tracks of `TkAlMinBias` to evaluate their value to alignment. It was of special interest if the bias introduced in section 6.1 does occur again. As seen in section 4.4, the detector resolution dominates the width of the invariant mass distribution. In order to correct for this effect a Gaussian fit to this distribution was performed and a corrected width of $\sigma = 0.1030$ GeV measured. Subsequently alignments were performed using the mass and vertex constraint, once configured with the natural width of the $\Upsilon$-meson, and once with the corrected $\sigma$.

Fig. 6.5a shows the measured $p_T$ resolution using the $p_T = 100$ GeV muon benchmark sample. Here the resolutions are compared to the initial misalignment ("Misaligned") and the results of the alignment using minimum-bias-alignment only ("no $\Upsilon$"). Again a degradation of the transverse momentum measurement is observed, which is not as large as the one seen in the previous section. However, Fig. 6.5b shows that a significant bias in the $\varphi$ measurement is

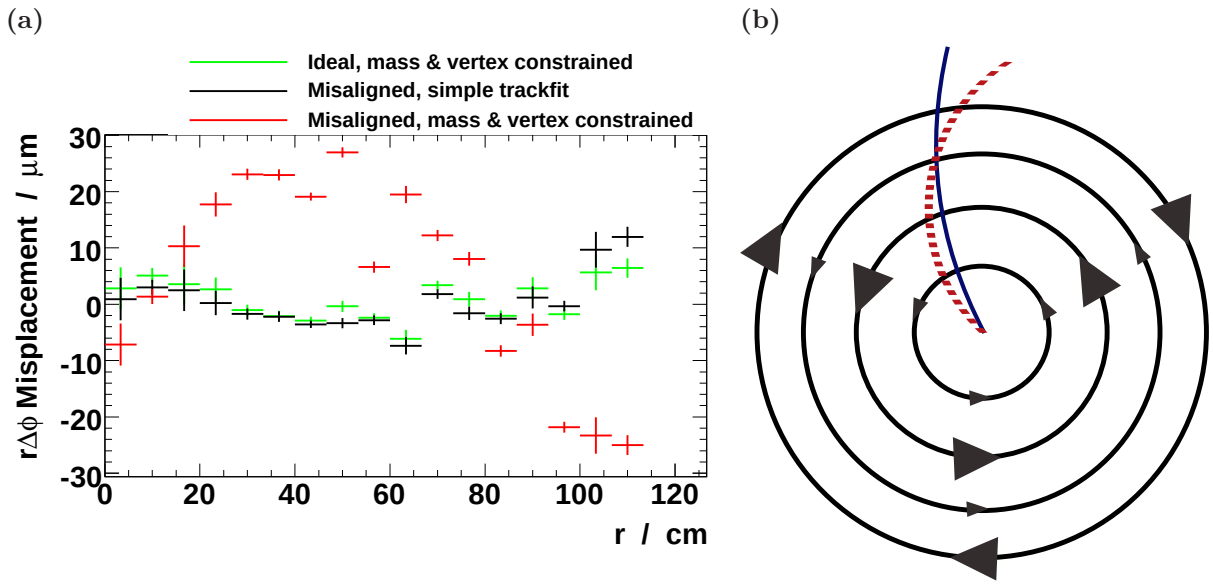


**Figure 6.4:** Measurement (a) and sketch (b) of the introduced $\chi^2$-invariant mode. The left hand side shows the precision of module alignment along $r\Delta\varphi$ versus the radial module position.

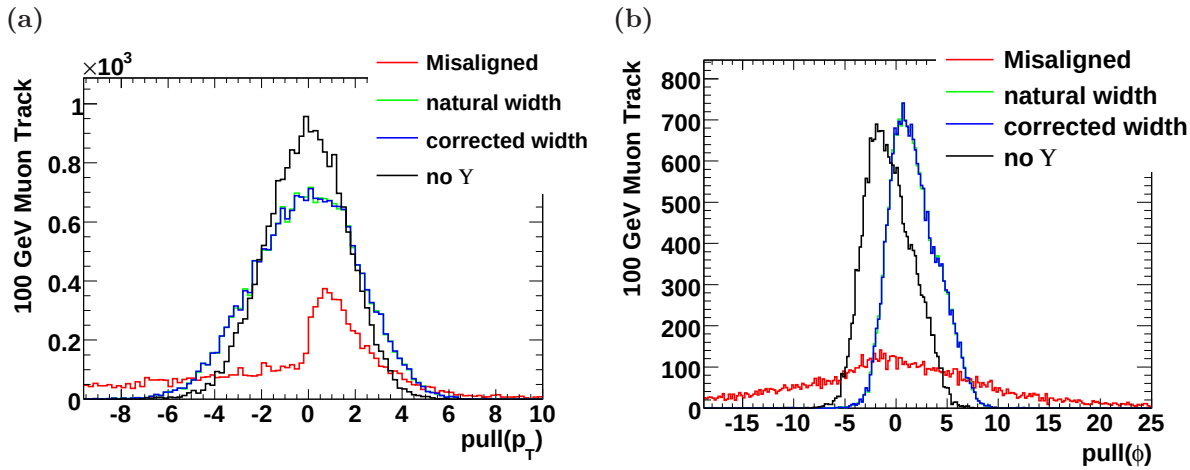


**Figure 6.5:** Comparison of tracking performance using the `TkAlUpsilonMuMu` selection in addition to the `TkAlMinBias` selection. Differences assuming measured (corrected) and natural width of the $\Upsilon$-meson are compared to the initial misalignment and results using `TkAlMinBias` only.

introduced. The average normalised $\chi^2$ of $1.278 \pm 0.061$ when only the `TkAlMinBias` selection was used is compatible to the normalise $\chi^2$ of $1.276 \pm 0.061$ obtained when the $\Upsilon$ selection is added and the mass and vertex constraint is applied. The conclusion is that again using the mass and vertex constraint a rotation of the modules along a $\chi^2$ invariant mode is introduced. The choice of the width used for the mass and vertex constraint does not affect these distortions.
Fig. 6.6 shows the deformation along $r\Delta\varphi$ as a function of the radial module position. The correlated distortion again is observed when starting from a misaligned geometry and using the mass and vertex constraint. The shape and amplitude is very similar to the distortion observed in Fig. 6.4a. Also a comparison to the misaligned scenario is made. The different shape of the distortion indicates that the distortion is introduced by the alignment and does not remain from initial misalignment.

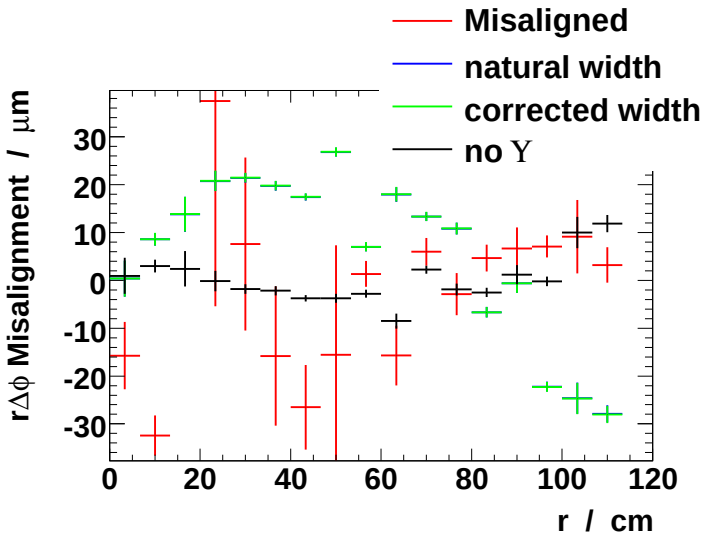


**Figure 6.6:** Correlation between misalignment along $r\Delta\varphi$ and the radial module position.

## 6.3 Conclusion for the Use of Mass and Vertex Constraint

Evidently applying the mass and vertex constraint does not degrade the $\chi^2$ for the reconstruction of the tracks used in the alignment process. Using the $Z \to \mu^+\mu^-$ it even improves. However, it introduces a significant bias to the measurement for the independent high momentum muon sample, but not for an independent $Z \to \mu^+\mu^-$ sample. Especially the reduced $\chi^2$ of the track fits is a sign of the otherwise $\chi^2$-invariant deformation being affected by the mass and vertex constraint.
It has also been shown that the observed correlated distortion is not a feature of the usage of the mass and vertex constraint in $Z \to \mu^+\mu^-$ events only, but does occur when the same constraining mechanism is used for $\Upsilon \to \mu^+\mu^-$ events, too. Furthermore tests mixing less minimum bias events or using the `TkAlMuonIsolated` selection have been fruitless.
To verify the assumption the nature of $\chi^2$-invariant deformations of the CMS inner tracking system has to be studied. This could be done by determining the eigen-vectors and eigenvalues of the matrix $C$ in equation 2.3 as described in [2]. However doing so for the full tracker alignment problem on module level needs vast computing resources and could not be done in the course of this thesis.

Additionally, the implementation of the mass and vertex constraint as reconstruction of two body decay events (see section 2.5) has to be investigated in order to exclude numerical errors that could lead to introduced misalignment.

## 6.4 The Use of Beam Halo Muons

Due to collisions of the LHC beam protons with residual molecules inside the evacuated beam pipe and the collimation of the beams directly before entering the CMS cavern a small number of charged particles are expected to travel nearly parallel to the beam line. Due to the hadronic nature of these interactions pions and kaons will be produced which, in turn can decay into muons. Those muons are able to traverse the material of the detector - including parts of the muon system and the caloremetry - and leave tracks in the inner tracking system. Because the tracks are nearly parallel to the beam line, they are expected to be beneficial to the alignment of the tracker end caps and tracker inner disks in the early stages of alignment. Furthermore their unique topology is expected to constrain otherwise weakly defined modes of the alignment problem. Due to this radically different topology a special pattern recognition and track reconstruction is in place [30]. Fig. 6.7a shows the positions of hits used for these track fits. It is observed that only modules of the forward pixel, the tracker inner disks and the tracker endcaps contribute, since angles of the trajectories of beam halo particles with respect to modules of the barrel region are expected to be too shallow to contribute reliable measurements. Therefore this study concentrates on improvements achieved in these subsystems.

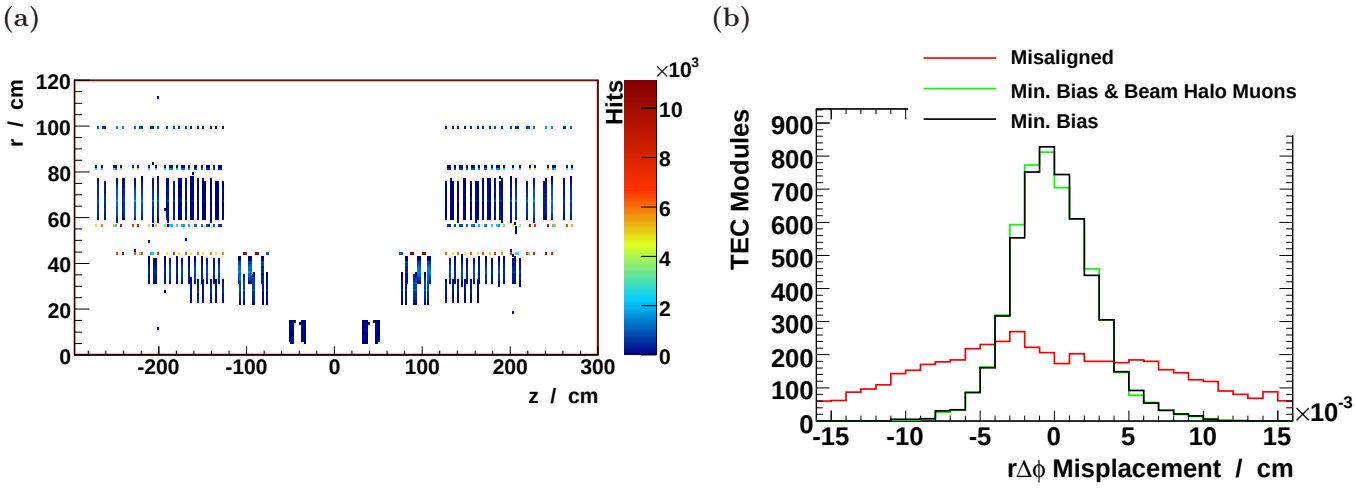


**Figure 6.7:** Positions of hits used in beam halo reconstruction (a) and residual misalignment along $r\Delta\varphi$ in the TEC mixing 32 million minimum bias tracks and 150 thousand beam halo tracks. (b)

For this first study of their impact on alignment a sample of about 150 000 tracks was available, which was simulated to contain muons only. As before this track selection was added to the `TkAlMinBias` selection and alignment constants were computed. Fig. 6.7b shows the residual misalignment along $r\Delta\varphi$ for the tracker end cap. In comparison to the alignment obtained using the `TkAlMinBias` selection alone no significant improvement is observed. Similarly Tab. 6.1 shows that no significant improvement is observed for the tracker inner discs and the forward pixels.
Since there is no significant improvement it is concluded, that the beam halo selection does not

**Table 6.1:** Comparison of the r.m.s of the residual misalignment along the $r\Delta\varphi$ coordinate using beam halo tracks.

| Subsystem | `TkAlMinBias` [µm] | `TkAlMinBias` + `TkAlBeamHalo` [µm] |
|---|---|---|
| PXF | $48.0 \pm 1.3$ | $47.9 \pm 1.3$ |
| TID | $47.0 \pm 1.4$ | $47.5 \pm 1.5$ |
| TEC | $28.0 \pm 0.27$ | $27.7 \pm 0.27$ |

constrain remaining $\chi^2$-invariant modes significantly. Due to the large difference in the number of $32 \cdot 10^6$ tracks in the `TkAlMinBias` selection and 150 000 beam halo tracks no significant improvement is expected due to the greater statistical power of the combined sample.

### 6.4.1 First Stand Alone Beam Halo Alignment

In the course of these studies the first full tracker alignment of the CMS tracker using beam halo tracks has been performed. Fig. 6.8 shows the improvement along the most sensitive coordinate $r\Delta\varphi$ in the tracker end cap. In this figure also the result of the alignment using 32 million tracks from the `TkAlMinBias` selection and the initial misalignment are shown. As expected from Fig. 6.7a the alignment of the forward pixel, the tracker inner disks, and the tracker endcaps improves, as summarised in Tab. 6.2.
These results prove that the workflow of special reconstruction, track selection, and final alignment is set up and ready for the first beam halo tracks to be recorded by CMS.

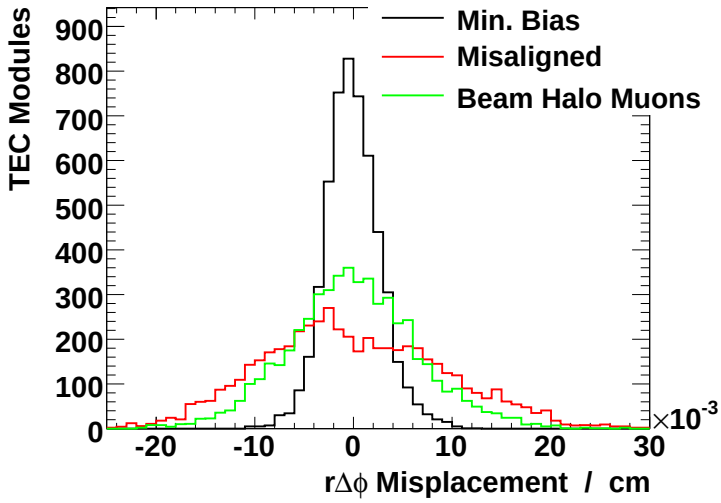


**Figure 6.8:** Residual misalignment of the TECs along $r\Delta\varphi$ using the `TkAlBeamHalo` selection.

## 6.5 The Use of Cosmic Muons

Another source of tracks that do not stem from the interaction point and thus have a different event topology are cosmic muons. It has already been shown that they are beneficial to alignment and do constrain otherwise unconstrained $\chi^2$-invariant modes [2]. To prove their usefulness to the start-up scenario the 32 million tracks of the `TkAlMinBias` selection have been combined with 240 thousand cosmic muon tracks. These have been selected requiring 18

**Table 6.2:** Comparison of the r.m.s of the residual misalignment along the $r\Delta\varphi$ coordinate using beam halo tracks.

| Subsystem | Misaligned [µm] | `TkAlBeamHalo` [µm] |
|---|---|---|
| PXF | $119.8 \pm 3.7$ | $106.1 \pm 2.9$ |
| TID | $445 \pm 13.7$ | $305 \pm 9.4$ |
| TEC | $91.9 \pm 0.90$ | $66.2 \pm 0.65$ |

hits and a transverse momentum of at least 15 GeV .
Fig. 6.9b shows the comparison between the combined and the uncombined track sample. A significant improvement of the alignment precision is observed for the overall tracking system and for the sub-systems as summarised in Tab. 6.3.

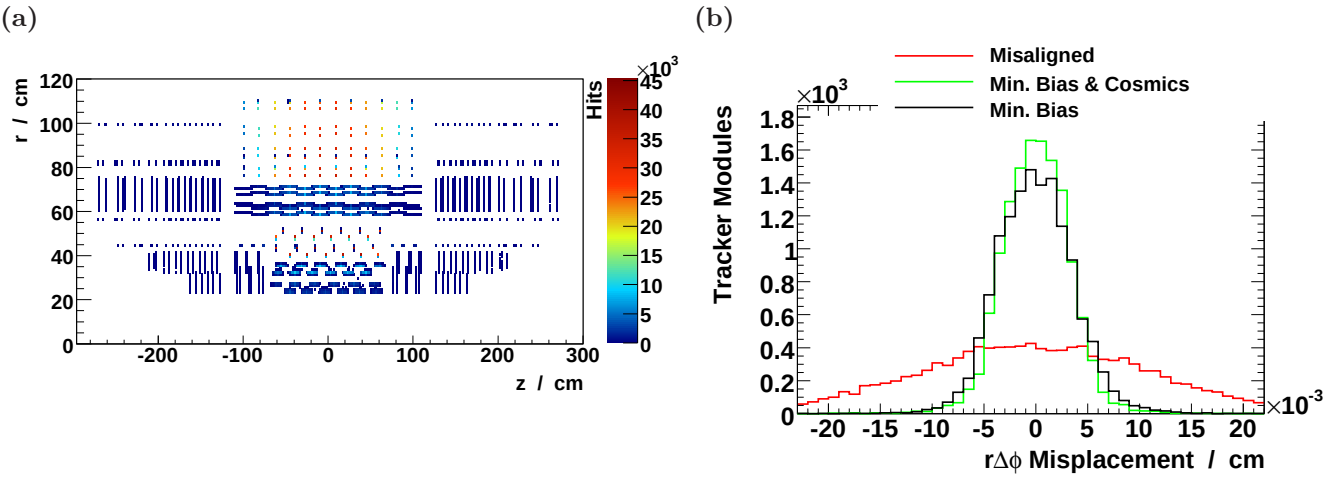


**Figure 6.9:** Positions of hits used in reconstruction of cosmic muons (a) and residual misalignment along $r\Delta\varphi$ for the whole tracking system mixing 32 million minimum bias tracks and 240 thousand cosmic muon tracks. (b)

Note that Fig. 6.9a shows that no cosmic muon track features a hit in the pixel detectors. This is due to a bug in the tracking code used during CSA08 and this thesis. Nevertheless the alignment precision of the pixel barrel is improved. Here the MillePede ansatz of simultaneously fitting all parameters pays off: By improving the alignment precision in the tracker inner and outer barrel the cosmic muon tracks allow a better fit of the pixel detector positions using the tracks from the `TkAlMinBias` selection.

## 6.6 Conclusion

- Beam halo muons can be used for alignment, but low statistics do not improve the $\mathcal{L} = 10$ pb$^{-1}$ alignment.
- Cosmics do help to improve even the $\mathcal{L} = 10$ pb$^{-1}$ alignment, therefore they are the most valuable sample for sample mixing.
- Compared to the usage of the mass and vertex constraint both samples perform well. One should not hesitate to use them on real data.

**Table 6.3:** Comparison of the r.m.s of the residual misalignment along the $r\Delta\varphi$ coordinate using cosmic muon tracks.

| Subsystem | `TkAlMinBias` [μm] | `TkAlMinBias` + `TkAlCosmicsCTF` [μm] |
|---|---|---|
| PXB | $5.4 \pm 0.14$ | $4.8 \pm 0.12$ |
| PXF | $48.0 \pm 1.4$ | $47.5 \pm 1.3$ |
| TIB | $23.3 \pm 0.37$ | $12.1 \pm 0.19$ |
| TID | $47.0 \pm 1.4$ | $41.5 \pm 1.2$ |
| TOB | $30.0 \pm 0.33$ | $19.1 \pm 0.21$ |
| TEC | $28.0 \pm 0.27$ | $29.2 \pm 0.28$ |
| Tracker | $36.5 \pm 0.22$ | $32.2 \pm 0.20$ |

# 7. Summary

Track based alignment is used to measure the position and orientation of more than 16 000 detector components of the CMS inner tracking system. The precision of this measurement depends on the quality and the amount of tracks used in the alignment procedure. Sources for these tracks are categorised into:

- resonance selections (e.g. $Z \to \mu^+\mu^-$, $J/\psi \to \mu^+\mu^-$ and $\Upsilon \to \mu^+\mu^-$ selections)
- selections offering high statistics (e.g. minimum bias and global muon selections)
- selections of tracks that do not stem from the interaction point (e.g. beam halo and cosmic muon selections)

The advantage of resonance selections for track based alignment is, that additional knowledge can be utilised – specifically that of the invariant mass of the resonance and the existence of a decay-vertex (mass and vertex constraint). Selections of tracks from the decay of the Z boson, the $J/\psi$ meson, and the $\Upsilon$ meson have been presented. In those, the purity has been maximised and high efficiency has been obtained (Tab. 7.1). The decay into two muons was chosen for all resonance selections. This way, errors due to material interaction during pattern recognition and reconstruction are minimised and the excellent particle identification of the CMS muon system is being used. The software developed for these selections was tested as part of the CSA08 exercise at conditions expected at LHC start-up. This test has shown that the applied high level trigger selection reduces the event rate to a level that can be handled by the computing infrastructure.

**Table 7.1:** Efficiencies and purities of available resonance selections

| Process | Efficiency [%] | Purity [%] |
|---|---|---|
| $Z \to \mu^+\mu^-$ | 40.2 | 98.4 |
| $J/\psi \to \mu^+\mu^-$ | 45.1 | 96.7 |
| $\Upsilon \to \mu^+\mu^-$ | 68.1 | 82.1 |

During the early stages of tracker alignment where only $\mathcal{L} = 10\ \mathrm{pb}^{-1}$ of data have been collected, the outcome was that the rate of these resonance selections was not sufficient to measure the positions and orientations of all tracking modules. In this scenario two selections offering high statistical power were studied. The minimum bias selection applies minimal cuts and achieves the highest statistical power (32 million selected tracks). The second selection is based on the muon identification by the CMS muon system and applies an additional jet isolation criterion. This reduces the statistical power of the selection to 8.5 million tracks of higher quality. It has been shown that the precision of the alignment can be modeled by $\mathcal{M}(n) = \mathcal{M}_0 + \frac{q}{\sqrt{n-n_0}}$ for both selections. Here, $\mathcal{M}$ denotes a metric measuring the alignment performance, $n$ denotes the number of tracks used in alignment, and $\mathcal{M}_0$, $q$, and $n_0$ are parameters of the fit.
A significant correlated distortion of the tracking geometry along the radial coordinate was observed when the minimum bias selection was used in alignment. This effect is suppressed when the muon selection is used. While this shows the higher quality of the muon selection, this selction lacks statistical power. The overall alignment precision of the minimum bias selection is better than that of the muon selection. This is shown by both the absolute misalignment with respect to the known geometry used during simulation, and the comparison of simulated and reconstructed track parameters.
In order to optimise the selection, cuts have been varied and the alignment performance of the resulting selections has been compared. For all cuts it has been shown that statistical power is paramount to track quality in the $\mathcal{L} = 10\ \mathrm{pb}^{-1}$ scenario. Furthermore, transverse momentum cuts can improve track quality when applied during the high level trigger selection for the minimum bias sample. Here, a reduction of the statistical power can be omitted by reducing the high prescales.

Finally, the increase of alignment performance by mixing high quality and high statistics selection has been studied. It has been shown that due to a large $\chi^2$-invariant deformation of the tracking geometry resonance selections are not useful in the $\mathcal{L} = 10\ \mathrm{pb}^{-1}$ scenario. In contrast to that, the selection of the third category presented to be beneficial. Tracks from muons generated in the upper atmosphere have a radically different topology than tracks emanating from the interaction point. When 240 000 tracks from this selection are added to the $32 \cdot 10^6$ tracks of the minimum bias selection, the best alignment presented in this thesis is achieved. The residual misalignment measured by the module alignment precision along the most sensitive coordinate $r\Delta\varphi$ is reduced from $(36.5 \pm 0.22)$ to $(32.2 \pm 0.20)$ µm. Utilising tracks from beam halo muons in this procedure did not show a similar improvement. These muons are produced in beam-gas interactions or during the beam collimation. Nevertheless, the first successful alignment using beam halo tracks was performed in this study.

Further studies of the track selection for alignment should investigate possibilities to improve track quality without limiting the statistical power. This goal could be reached with a dedicated high level trigger selection for alignment. Additionally, once CMS has begun to harvest data, the alignment performance of the Monte Carlo selections needs to be compared to real data selections. Differences occurring in these two selections will lead to further improvements of the track selection and might thus complement the studies elaborated in this thesis.

# Bibliography


[1] M. V. Donckt, Top Physics at LHC, CMS Conference Report CMS CR-2008/017.

[2] G. Flucke, P. Schleper, G. Steinbrück, M. Stoye, CMS silicon tracker alignment strategy with the Millepede II algorithm, JINST 3 P09 002.

[3] J. Drees, Review of final LEP results or a tribute to LEP, Int.J.Mod.Phys. A17 (2002) 3259-3283.

[4] L. Evans, P. B. (editors), LHC Machine, JINST 3 S08 001.

[5] ATLAS collaboration, The ATLAS Experiment at the CERN Large Hadron Collider, JINST 3 S08 003.

[6] CMS Collaboration, The CMS experiment at the CERN LHC, JINST 3 S08 004.

[7] LHCb Collaboration, The LHCb Detector at the LHC, JINST 3 S08005.

[8] Alice collaboration, The ALICE experiment at the CERN LHC, JINST 3 S08 002.

[9] M. Schwartz, D. Fehling, G. Giurgiu, P. Maksimovic, V. Chiochia, A new technique for the reconstruction, validation, and simulation of hits in the CMS Pixel Detector, CMS Note 2007/033.

[10] L. Borrello, A. Messineo, E. Focardi, A. Macchiolo, Sensor design for the CMS Silicon Strip Tracker, CMS Note 2003/020.

[11] CMS Collaboration, CSA07 HLT Menu, CERN/LHCC LHCC-G-134.

[12] CMS HLT Group, CSA08 HLT Menu, https://twiki.cern.ch/twiki/pub/CMS/TSG_27_V_08/HLTM

[13] T. Lampen, N. de Filippis, F.-P. Schilling, A. Schmidt, M. Weber, Comprehensive Set of Misalignment Scenarios for the CMS Tracker, CMS Note 2008/029.

[14] V. Blobel, C.Kleinwort, A new method for high-precision alignment of track detectors, Contribution to the Conference on Advanced Statistical Techniques in Particle Physics, Durham hep-ex/0208021.

[15] V. Blobel, Millepede II manual DRAFT, http://www.desy.de/˜blobel.

[16] Bronstein, Semendjajew, Musiol, Mühlig, Taschenbuche der Mathematik (5. Auflage, 2001).

[17] F. Zhang, The Schur Complement and Its Applications (April 2005).

[18] A. Meister, Numerik linearer Gleichungssysteme (1999).

[19] D. Hoaglin, Understanding robust and exploratory data analysis (June 2000).

[20] V. Innocente, L. Silvestris, D. Stickland, CMS Software Architecture, CMS Note 2000/047.

[21] E. Widl, R. Frühwirth, Representation and Estimation of Trajectories from Two-body Decay, CMS Note 2007/032.

[22] P. Schieferdecker, M. V. Acosta, A. Oehler, K. Rabbertz, G. Bruno, D. Kcira, L. Quertenmont, P. Kurt, C. Dragoiu, N. Varelas, F. Ratnikov, J. Widawsky, M. Zielinski, A. Bhatti, G. Dissertori, Performance of the $k_t$ jet algorithm in CMSSW, CMS Internal Note CMS IN 2007/062.

[23] CSA08 Collaborators, The 2008 CMS Computing Software and Analysis Challenge (to be published as CMS Note).

[24] S. Dutta, V. Chiochia, M. S. Mennea, G. Zito, Data Quality Monitoring for the CMS Silicon Tracker, CMS Conference Report CMS CR 2006/012.

[25] W.-M. et al. (Particle Data Group), The Review of Particle Physics, J. Phys. G 33 1 (2006).

[26] M. Mangano, M. Moretti, F. Piccinini, R. Pittau, A. Polosa, ALPGEN, a generator for hard multiparton processes in hadronic collisions, JHEP 0307 (2003) 001.

[27] T. Sjöstrand, L. Lönnblad, S. Mrenna, PYTHIA 6.2 Physics and Manual (31 Aug 2001).

[28] CMS Collaboration, CMS Technical Design Report Vol. II, Journal of Physics G Volume 34 Number 6.

[29] W.Adam, T. Speer, B. Mangano, T. Todorov, Track reconstruction in the CMS tracker, CMS Note 2004/041.

[30] J.-R. Vlimant, private communication (2008).

# A. Danksagung

Zuerst möchte ich mich bei Professor Dr. Lutz Feld für die Möglichkeit diese Arbeit anzufertigen bedanken. Besonders danke ich ihm für seine Geduld und Unterstützung, sowie die Gelegenheit am CERN zu arbeiten.
Außerdem danke ich Professor Dr. Achim Stahl für die freundliche Zweitkorrektur.
Mein besonderer Dank gilt Dr. Martin Weber der diese Arbeit betreut hat. Ich bin sehr dankbar für die angeregten Diskussionen die ich mit ihm führen durfte und sein unermüdliches Korrekturlesen meines Manuskripts.
Weiterhin haben Martin, Daniel, Niklas, Richard, Klaus und Albert es immer verstanden ein angenehmes Arbeitsklima zu schaffen. Auch Katja, Jenny, Jan und Rüdiger haben dieses produktive Klima in der Gruppenzusammenarbeit geprägt. Vielen Dank dafür! Besonders habe ich das Zusammenleben mit Daniel und Martin in Genf genossen, das wir trotz vieler Arbeit angenehm gestaltet haben.
I want to thank the CMS Collaboration and the especially the alignment group for their support and many interesting discussions. Besonders Dr. Markus Stoye und Dr. Gero Flucke gilt mein Dank für ihre Anleitung in der Bedienung des MillePede 2 Paketes und der Interpretation seiner Ausgaben.
Auch Stefan Kawalla möchte ich danken, der mir zu jeder Tages- und Nachtzeit in Fragen zur englischen Sprache beigestanden hat.

Ein Physikstudium ohne Kommilitonen und Freunde mit denen man die Wirren und Herausforderungen meistern kann erscheint mir wenig erstrebenswert. Für mich waren Konstantin, Sebastian, Aaron, Walter und besonders Daniel diese Freunde und ich danke ihnen dafür. Auch meinen Eltern und meinem Großvater danke ich nicht nur für die finanzielle sondern auch für die seelische Unterstützung während des Studiums.
Zuletzt gilt mein besonderer Dank meiner Frau Anke, die mir in allem eine beständige, fürsorgliche und liebevolle Partnerin ist.

# B. Erklärug

Hiermit versichere ich, dass ich die vorliegende Arbeit selbstädig verfasst und keine anderen als die angegebenen Quellen und Hilfsmittel verwendet habe.

Aachen, den 11.12.2008

Matthias H. Edelhoff